UNIVERSITÉ DE MONTRÉAL

PLASMA ACTUATION FOR ACTIVE CONTROL OF WIND TURBINE POWER

SHUBHANKAR GHOSH
DÉPARTEMENT DE GÉNIE MÉCANIQUE
ÉCOLE POLYTECHNIQUE DE MONTRÉAL

MÉMOIRE PRÉSENTÉ EN VUE DE L'OBTENTION
DU DIPLÔME DE MAÎTRISE ÈS SCIENCES APPLIQUÉES
(GÉNIE MÉCANIQUE)
DÉCEMBRE 2011

UNIVERSITÉ DE MONTRÉAL

ÉCOLE POLYTECHNIQUE DE MONTRÉAL

Ce mémoire intitulé :

PLASMA ACTUATION FOR ACTIVE CONTROL OF WIND TURBINE POWER

Présenté par : GHOSH Shubhankar

en vue de l'obtention du diplôme de : Maîtrise ès sciences appliquées

et a été dûment accepté par le jury d'examen constitué de :

M. MUREITHI Njuki, Ph.D., président

M. VO Huu Duc, Ph.D., membre et directeur de recherche

M. MASSON Christian, Ph.D., membre et codirecteur de recherche

M. LAURENDEAU Éric, Ph.D., membre

Acknowledgements

I would like to express my deepest gratitude to Prof. Huu-Duc Vo for his continuous guidance and support for me and my research. His suggestions and inputs have been extremely helpful in the shaping of this thesis. His advice related to all CFD- and experiment-related issues is highly appreciated.

I wish to thank Prof. Masson for his support and for sharing his expertise on wind turbines. His graduate course on wind turbine technology provided information that is indispensable to this thesis.

I would like to express my gratefulness to Philippe Versailles for having carried out the preliminary work which is the foundation of this research. I would also like to thank Xiaofei Xu for his contribution in the CFD implementation of the plasma actuator model and for his help with the plasma generation system.

Thanks are also due to Javad Hosseini, Mert Cevik and Catherine Mastrostefano for their help with the wind tunnel experiments. I also thank Eray Akcayoz and Engin Erler for helping maintain a pleasant work atmosphere in our office.

In the end, I would like to thank my parents for their support and patience over the last two years.

Résumé

Cette recherche évalue, optimise et démontre expérimentalement une nouvelle méthode pour réduire la portance et augmenter la traînée d'une pale de turbine éolienne pour contrôler la puissance éolienne à des vitesses de vent élevées. La méthode consiste à appliquer l'actionnement électro-fluidique du plasma pour accélérer la séparation de la couche limite sur les pales d'éolienne. L'effet de l'actionnement plasma sur un profil à deux dimensions d'éoliennes est d'abord évalué numériquement à de faibles nombres de Reynolds en utilisant un code commercial CFD auquel un modèle de l'actionneur plasma est intégré. Les résultats de ces simulations indiquent l'existence de conditions d'exploitation préférable pour l'actionneur plasma en termes de paramètres tel que sa force, la vitesse non-perturbée et sa position sens de la corde sur la pale. En ce qui concerne la force d'actionnement, il est constaté qu'il existe un seuil de la force au-delà duquel il y a un saut soudain dans la réduction de portance obtenue. Un bond semblable à l'effet d'actionnement est observé lorsque le nombre de Reynolds non-perturbé est réduit en deçà d'une certaine limite. L'existence de positions optimales pour l'actionneur plasma sur l'extrados de la pale est également observée. L'optimum est situé près du bord de fuite de l'aile pour les angles d'attaque avant le décrochage et il est déplacé en amont aux angles d'attaque près du décrochage et dépassés le décrochage. Toutes les simulations indiquent que la position de l'actionneur plasma par rapport au point de séparation de la couche limite est le facteur décisif à l'effet de l'actionneur sur la portance et la traînée. Ces simulations sont validées par des en soufflerie tests pour les mêmes conditions d'écoulement en soufflerie. Les mesures en soufflerie de la portance et la traînée se trouvent principalement à être cohérents avec les résultats de simulations. Le logiciel CFX validé expérimentalement est ensuite utilisé pour simuler l'écoulement à un *Re* réaliste pour les applications éoliennes. Cette étude montre que le niveau actuel de la force d'actionnement plasma est incapable d'exercer une influence perceptible sur les performances d'une éolienne. La théorie de l'élément de pale couplée à un bilan de quantité de mouvement est utilisée pour déterminer la quantité de la chute de portance qui serait nécessaire pour le fonctionnement à puissance nominale et cette exigence est comparée à l'impact de l'actuelle génération d'actionneurs plasma. Une tentative est faite pour estimer la force d'actionnement qui serait nécessaire pour réaliser la réduction de la puissance requise pour le fonctionnement nominal. Cette analyse montre qu'une force d'actionnement de deux ordres de grandeur serait nécessaire pour que le concept fonctionne sans l'aide d'un autre moyen de contrôle pour limiter la puissance des éoliennes. Cela implique qu'il doit être couplé avec une

autre méthode comme le contrôle de la vitesse du rotor pour avoir une possibilité réaliste d'application dans un proche avenir.

Abstract

This research evaluates, optimizes and experimentally demonstrates a new method to reduce the lift and increase the drag of a wind turbine blade for controlling the turbine power at high wind speeds. The method consists of applying electro-fluidic plasma actuation to accelerate the separation of boundary layer on the wind turbine blade. The effect of plasma actuation on a two-dimensional wind turbine profile is first assessed numerically at low Reynolds numbers *Re* using a commercial CFD code to which a plasma actuator model is integrated. The results from these simulations indicate the existence of preferred operating conditions for the plasma actuator in terms of parameters such as its strength, the free-stream velocity and its chordwise position on the blade. With respect to the actuation strength, it is found that there exists a threshold strength beyond which there is a sudden jump in the lift reduction obtained. A similar jump in the actuation effect is observed when the free-stream Reynolds number is reduced past a certain limit. The existence of optimal positions for the actuator on the suction side of the blade is also observed. The optimum is situated near the airfoil's trailing edge for a pre-stall angle of attack and it is displaced upstream at stall and post-stall angles of attack. All the simulations indicate that the position of the actuator relative to the point of separation of the boundary layer is the key element in the actuator's effect on lift and drag. These simulations are validated by testing for the same flow conditions in wind tunnel. The wind tunnel measurements of lift and drag replicate the trends seen in the simulations. The experimentally validated CFD tool is then used to simulate wind turbine flows at a realistic Reynolds number. This study shows that the current level of plasma actuation strength is incapable of exerting any discernable influence on the performance of a wind turbine blade. The blade element momentum theory is used to determine the amount of lift drop that would be required for rated power operation and this requirement is compared with the impact of the current generation of plasma actuators. An attempt is made at estimating the actuation strength that would be necessary to bring about the power reduction required for rated operation. This analysis shows that actuator strength of two orders of magnitude higher would be required for the concept to work on its own to limit wind turbine power. This implies that it must be coupled with another method such as rotor speed control to have a realistic chance of application in the near future.

Table of Contents

List of Figures

List of Appendices

CHAPTER 1
INTRODUCTION

1.1 Background

Global warming, geopolitical self-sufficiency based on energy security and rising prices of fossil fuels has increased pressure on companies and societies to turn to renewable energy. Of all the available sources, wind energy constitutes a source with great potential. In the past few decades, the evolution of wind energy has been sustained and rapid. It is in fact the fastest growing energy source, doubling its capacity every three years. At the end of 2009, the worldwide installed wind power capacity stood at 159 GW which rose to around 175 GW by mid-2010 and was expected to surpass 200 GW by the end of 2010. Currently, 340TWh of wind energy is being produced annually which is 2% of the worldwide electricity consumption [1].

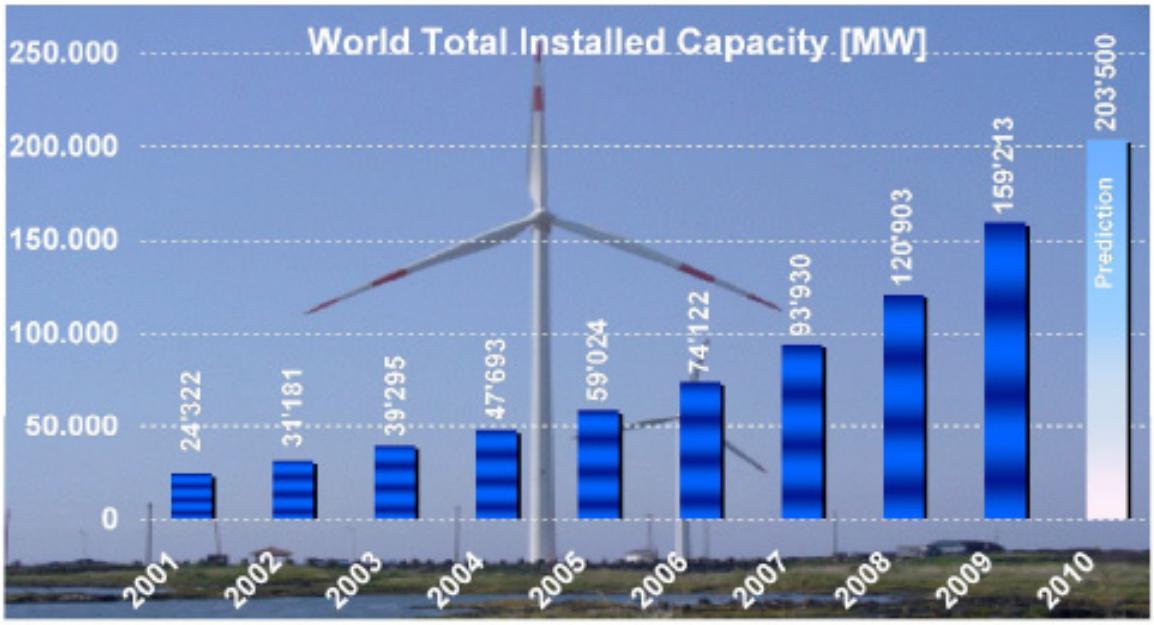

Figure 1.1 Rise in the installed wind power capacity in the last decade [1]

Wind turbines have expanded both in size as well as capacity in the past few decades and continue to do so. The turbines of 25 years ago had diameters of the order of 15m and produced typically 50 KW whereas the turbines of today have rotor diameters in excess of 100m and can generate up to 5MW of power. There is enormous wind potential that still remains to be exploited, especially offshore wind energy.

However, in the current economic context, the relatively high cost of wind turbines is a significant barrier to their proliferation and can deter prospective investments into the wind

energy sector. As a result, wind energy is faced with the challenge of remaining commercially viable and cost-effective. This challenge also presents opportunities to improve and optimize various aspects of the wind energy technology.

The power control of wind turbines is one such major challenge. It is a major factor in their cost of acquisition and exploitation.

1.2 Problem Definition

The power characteristics of a typical horizontal-axis wind turbine are qualitatively similar to Figure 1.2. This figure illustrates the different regimes of operation of a wind turbine.

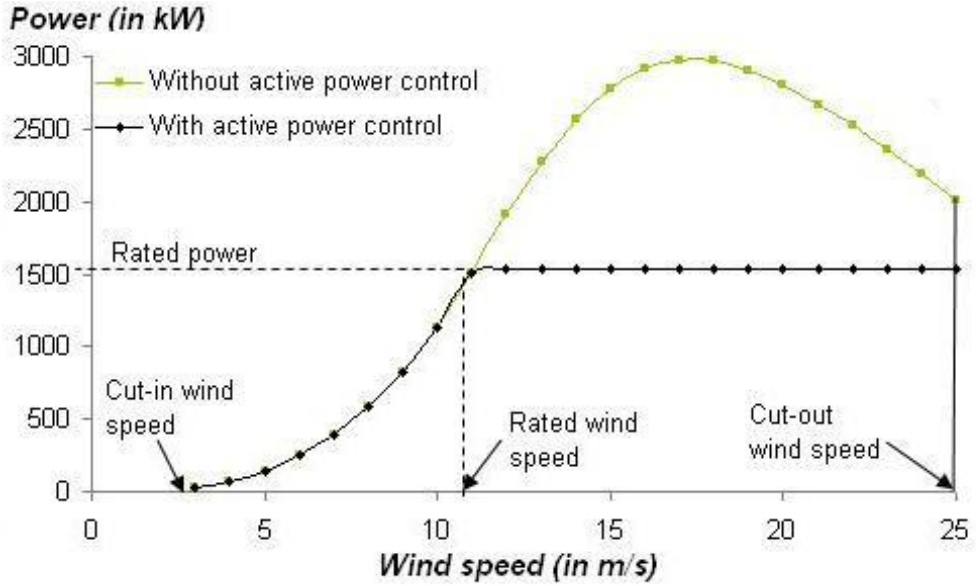

Figure 1.2 Typical power curve of a wind turbine

At speeds less than the cut-in speed, there is very little power being generated. For speeds greater than the cut-in speed, the power increases almost proportionally with respect to the cube of velocity in much the same way as the theoretical prediction. If left unchecked, this rise would continue till high values of velocity, at which point the blade begins to stall if the rotational speed is maintained constant. After a certain upper limit of the velocity, it is advisable to shut down the wind turbine to prevent damage to the rotor blade, the generator and other components. This upper limit is called the cut-out wind speed.

A wind turbine must produce electricity at the lowest possible cost. In this context, it is designed to produce maximum power or the rated power at an average wind speed of about 12.5 to 15 m/s (also called the rated wind speed), rather than for the stronger winds that come only a few times during the year and for which an optimal design of wind turbine would be more expensive. During strong winds, the turbine should not exceed its maximum design output to

avoid risking mechanical failure. Therefore, a reliable and economical technology to control the wind turbine power is required to enable a more widespread use of this clean energy source.

1.2.1. Wind Turbine Power Generation Explained with Blade Element Theory

Most modern horizontal-axis wind turbines (HAWTs) rely on the lift generated on the blades by the relative inflow of the wind to produce power. The blade element theory, which treats each rotor blade as a combination of several sections or *elements* and estimates the turbine performance from the superposition of the effects of these elements, permits the determination of the rotor power as a function of the lift and drag coefficients of the airfoil(s) in question.

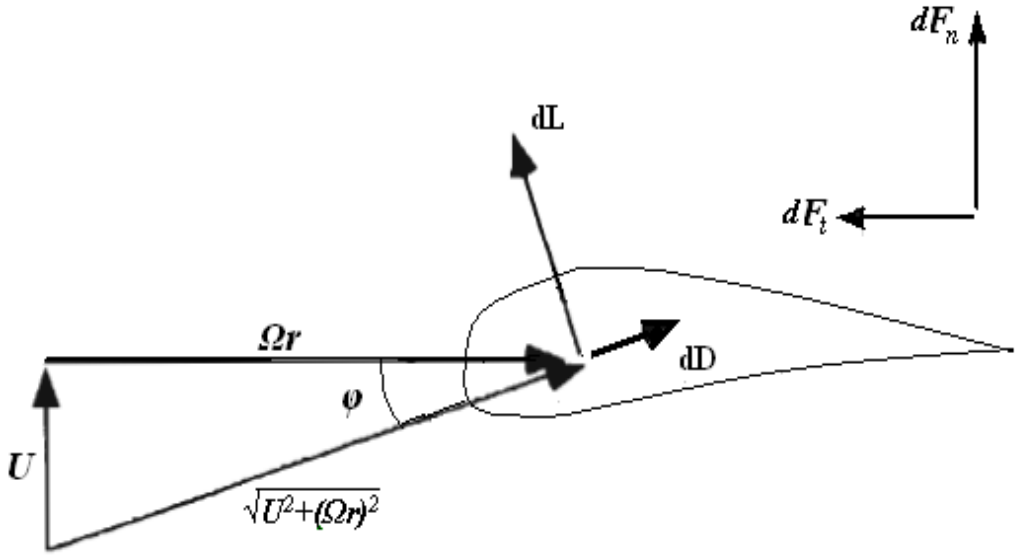

Figure 1.3 Relative velocity and aerodynamic forces on a blade element

Figure 1.3 shows the velocity and force vectors on a blade element of length *dr*, at a radial distance of *r* from the hub, rotating at an angular speed of Ω. The wind velocity at the blade rotor plane is U. It should be noted that this velocity is less than the free-stream velocity by a fraction called the axial induction factor. The relative speed U_{rel} is, therefore, $[U^2+ (\Omega r)^2]^{0.5}$ and is oriented at an angle φ from the plane of rotation. The differential drag dD and differential lift dL, being respectively parallel and perpendicular to this speed, are also inclined at φ to the plane of rotation and its normal.

dF_n and dF_t, the resultant force components in the normal and tangential directions respectively, can be computed from the resultant of the components of dL and dD in the respective directions [2].

If B is the number of blades, the total differential torque dQ produced on the blade elements at a radial distance of r by the tangential force dF_t is: $dQ = B\ r\ dF_t$. The total torque Q is given by $Q = \int dQ = B \int r\ dF_t$ and the power generated P is given by $P = Q\Omega$.

The above expression for the rotor power demonstrates that the power output of a wind turbine is a function of the lift and drag acting on the blades. A reduction of the lift and/or an enhancement of the drag bring(s) about a decrease in the power output. This is the working principle behind all aerodynamic methods of power control including deployment of flaps and pitching of blades.

1.2.2. Boundary Layer Control

Several techniques have so far been developed for the purpose of power and load control in wind turbines. Some of these techniques are based on controlling the boundary layer on the suction surface of the blade. As the near-wall flow moves downstream along the blade's suction side, it encounters an adverse pressure gradient which weakens the boundary layer and may cause it to detach from the blade's surface. Beyond a relatively high angle of attack, this phenomenon is intense enough to curtail the increase in lift that otherwise entails an increase in the angle of attack and a decrease in the lift coefficient follows. The airfoil, in this condition, is said to be stalled. If the boundary layer separation can be enhanced over an airfoil without increasing the angle of attack, the lift invariably drops for that particular angle. Boundary layer control is achieved by devices placed on the airfoil that are capable of manipulating the boundary layer, thereby affecting the pressure distribution and the lift and drag on the airfoil.

The present research intends to control the wind turbine rotor output power by using a plasma actuator on the blade suction side to add momentum in the upstream direction. Plasma actuators are discussed in detail in Section 1.3. This addition of momentum would induce or intensify suction side boundary layer separation, as shown in Figure 1.4, so as to limit blade lift and hence the power output at the high angles of attack associated with high wind conditions.

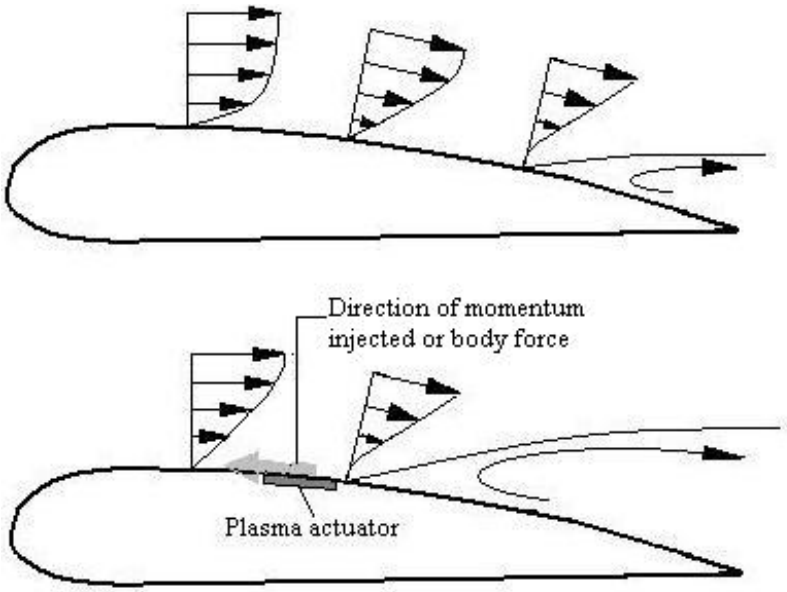

Figure 1.4 Enhancement of flow separation by plasma actuation

1.3 Concept of Plasma Actuation

Although there are various kinds of techniques currently employed for wind turbine power control, they all suffer from one or more drawbacks as discussed in the next chapter. This research proposes the novel technology of plasma actuation as a viable solution that is free from a lot of the practical restrictions, mechanical and economical, posed by the use of the conventional techniques. The potential of plasma actuators to address the problem is evaluated and analyzed in this project.

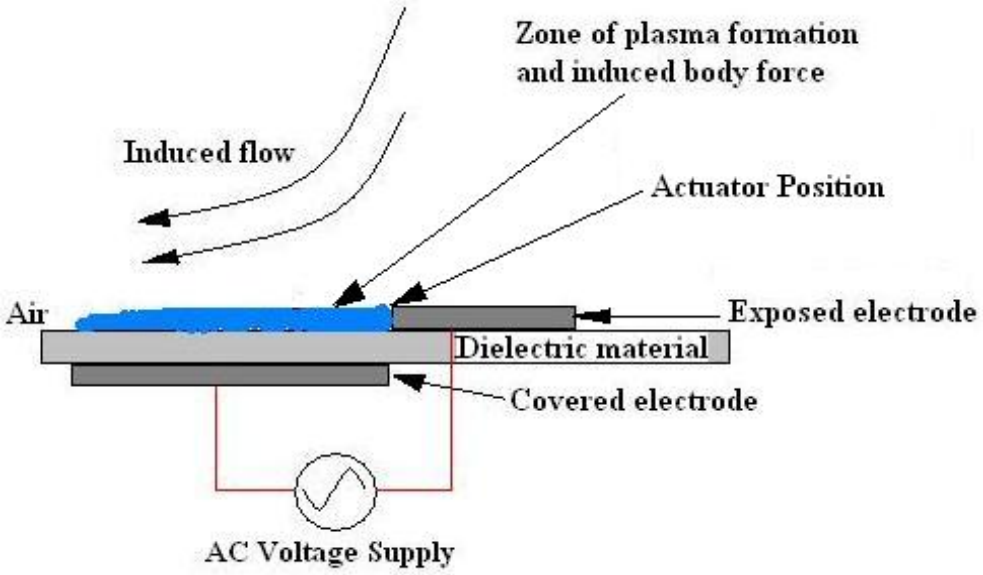

Figure 1.5 Schematic of a plasma actuator

A typical DBD (dielectric barrier discharge) plasma actuator, the most common variety of plasma actuators, is an electro-fluidic device which consists of two thin electrodes arranged asymmetrically and parallel to each other, one electrode exposed to the air and the other one offset axially and fully hidden beneath a layer of dielectric material. Figure 1.5 is a schematic of an actuator configuration known as single dielectric barrier discharge or SDBD. When a radio frequency AC voltage signal of relatively low power but sufficiently high amplitude ($O(kV_{pp})$) is applied across the electrodes, a weak ionization of the air takes place above the covered electrode with little or no heating. In presence of the electric field between the electrodes, the ionized particles, also called the plasma, experience an electric force and are accelerated. Their collision with the inert air particles results in momentum addition to the flow near the surface, equivalent to a body force acting on the air in motion. The magnitude of this force is quantified per unit of spanwise length under the name of plasma actuation strength and is measured in mN/m. In quiescent conditions, the effect of this body force is remarkably similar to a thin wall jet adjacent to the surface. More details on plasma actuators can be found in reference [3]. Plasma actuators are simple electric devices without any moving parts and consume very little power. Consequently, they are robust, easily integrable to existing structures and have higher bandwidth than mechanical actuators. Given that the electrodes have negligible thickness, plasma actuators can be made flush with the suction surface of the wind turbine blade, thus presenting a virtually non-intrusive solution to modify the effective aerodynamic shape of the wind turbine profile via the body force. For the purpose of this project, the axial position of the actuator is an important parameter. It should be noted that all the subsequent mentions of the actuator position in this thesis refer to the edge of the exposed electrode as shown in Figure 1.5.

The technology of plasma actuation has evolved considerably over the past few years. The following sub-section discusses the various applications where it has thus far been employed.

1.3.1. Previous Applications

Plasma actuators were first investigated by Roth *et al*. [4] in 2000. Since then, these actuators have been used for the control of leading edge boundary layer separation to maintain airfoil lift at high angles of attack and enhance lift at low and moderate angles of attack [5-11] by adding momentum in the direction of the incoming flow. These studies have used different actuator configurations, actuation locations and voltage wave-forms to delay flow separation but they have all dealt mostly with laminar flows of speeds ranging up to 30 m/s and produced similar results.

Plasma actuation was investigated for its ability to reduce the viscous drag in the case of a turbulent boundary layer in [12] with moderate success. Thomas *et al*., in [13], presented the results that they obtained from plasma actuation in order to streamline the flow past a cylindrical bluff body and to reduce noise.

In [14], Li *et al*. showed that upstream plasma forcing, located at ±90 deg on a circular cylinder with respect to the inflow, is quite effective in attenuating the noise from the wake flow interaction with an oblique downstream strut which is also a part of the bluff body. In another study [15] aimed at noise reduction, the results showed that continuous plasma actuation near the trailing edge can reduce the wake of a rotor considerably with relatively low power consumption and that the effect of the actuation is proportional to its strength.

In [16], plasma actuation was investigated for its potential to improve jet mixing. Huang *et al*., in [17], employed plasma actuation for the control of flow separation over blades in the low pressure turbine stage of a gas turbine engine at a Reynolds number typical of high altitude cruise. In [18], List *et al*. demonstrated the elimination of the separation bubble on a turbine blade in a linear cascade at low Reynolds numbers.

High flow turning in compressor stages [19] was achieved at a tip Mach number of 0.5 in a CFD assessment by Lemire et. al. Significant recovery of pressure was achieved in diffusers [20] with the help of spanwise acting plasma actuators generating a pair of streamwise vortices at the inlet section.

Moreover, plasma actuators have been studied for controlling tip clearance flow to increase turbine efficiency. In [21], the plasma force was oriented perpendicular to the camber line to resist the leakage flow through the tip gap. In the study carried out in [22], plasma actuation was found to bring about a 29.5% decrease in maximum pressure loss at a Reynolds number of 10^5 and a 14.7% decrease at a Reynolds number of 10^4.

The suppression of aerodynamic instabilities (criteria associated with spike rotating stall) in compressors with a plasma actuator was demonstrated in [23]. In their study, Li *et al*. [24] found that three plasma actuators placed at different chordwise positions on the endwall in a compressor cascade were most effective in reducing the pressure loss and flow blockage when operated simultaneously.

The above applications and some others have been discussed in greater detail in [5] and [25]. The impact of plasma actuation, as studied in [25], on an airflow that has separated past the leading edge of a flat plate is shown in Figure 1.6.

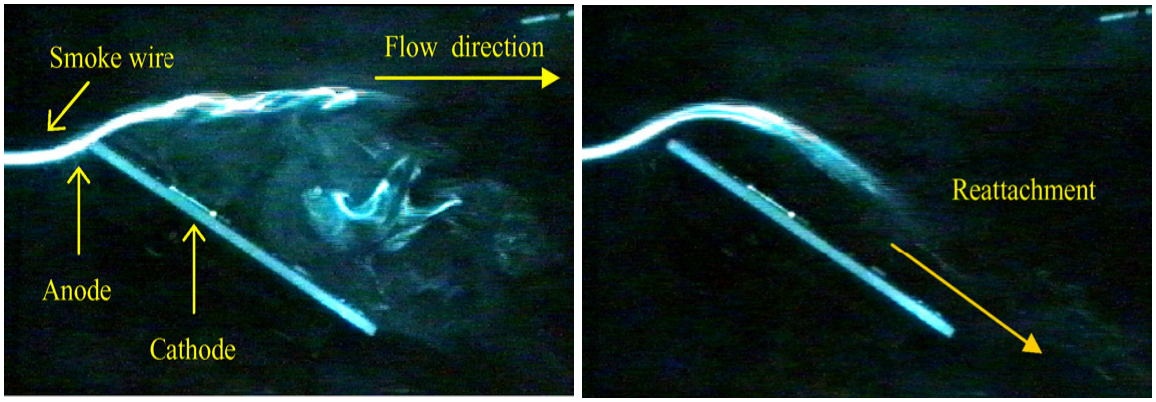

(*a*) (*b*)

Figure 1.6 Smoke flow visualization (a) in absence, (b) in presence of actuation [25]

1.4 Research Question

The basic question addressed in this work is whether plasma actuation is, by itself, capable of limiting the power of a MW (Megawatt)-class wind turbine. Moreover, what is the most optimal configuration (in terms of actuator location and strength) for power control using this concept and which are the conditions of flow incidence and velocity best suited for its application? A preliminary response to this research question was attempted in [26]. This work is discussed in more detail in Chapter 2.

1.5 General and Specific Objectives

The general objective of this project is to demonstrate the reduction of lift by plasma actuation on a 2-D profile of a wind turbine blade at low Reynolds number *Re* and estimate the effect on full-scale blades at realistic Reynolds numbers.

The specific objectives are stated below:

1. Assess numerically (CFD) the effectiveness of plasma actuators to influence lift on a 2-D wind turbine blade profile with respect to parameters such as actuator location and strength, flow incidence and velocity at low Reynolds number *Re*.
2. Validate experimentally the low *Re* numerical results in a wind tunnel.
3. Determine the effect of plasma actuation at realistic Reynolds numbers using a CFD code validated by wind tunnel testing.
4. Estimate the net change in lift from plasma actuation for a 3-D blade under high wind conditions from 2-D profile analysis.
5. Evaluate impact on the power output of a typical MW-class wind turbine.

1.6 Thesis Outline

This thesis consists of five chapters. The first chapter introduces the research problem and the concept of plasma actuation.

Chapter 2 contains a detailed review of the literature that describes the research that has been undertaken in the area of wind turbine power control along with the merits and demerits of each method. It also discusses the work that has thus far been done with regard to the development and computational modeling of plasma actuation.

Chapter 3 lays down the methodology that has been followed in order to achieve the goals of this research. It presents the details of the computational study comprising of the set-up of the CFD tool with the incorporation of the plasma actuator model and the experimental set-up which includes the plasma generation system and the test blade in the wind tunnel.

Chapter 4 contains the results from the parametric study of plasma actuators through numerical simulations and wind tunnel runs and a discussion on the implications of these results. It also studies the requirements of real-scale wind turbines in terms of power control and load reduction.

Chapter 5 gives an account of the conclusions of this study and suggestions for future work.

CHAPTER 2

LITERATURE REVIEW

This chapter presents an overview of the work that has been previously carried out by other researchers and which is fundamental to the current project. The preceding work can always be assigned to one of the following two categories:

1) Flow control methods over wind turbine blades, and
2) The technology of plasma actuation.

These are the two approaches that are adopted in this chapter to discuss the earlier research.

2.1 Wind Turbine Flow Control

The term flow control can be associated with any device or method that modifies a given flow field. Such alteration of the flow could be desirable for a variety of reasons, ranging from enhancement of lift to augmentation of mixing. The benefits of flow control are generally many fold and not mutually exclusive. In some cases, flow control employed for a particular benefit may also entail one or more undesirable effects on other properties of the flow. In these cases, a trade-off has to be made based on judgment.

So far, the techniques employed for controlling the flow around commercial wind turbines and hence their electrical power output can be classified under two categories. These are passive control and active control as shown in Figure 2.1.

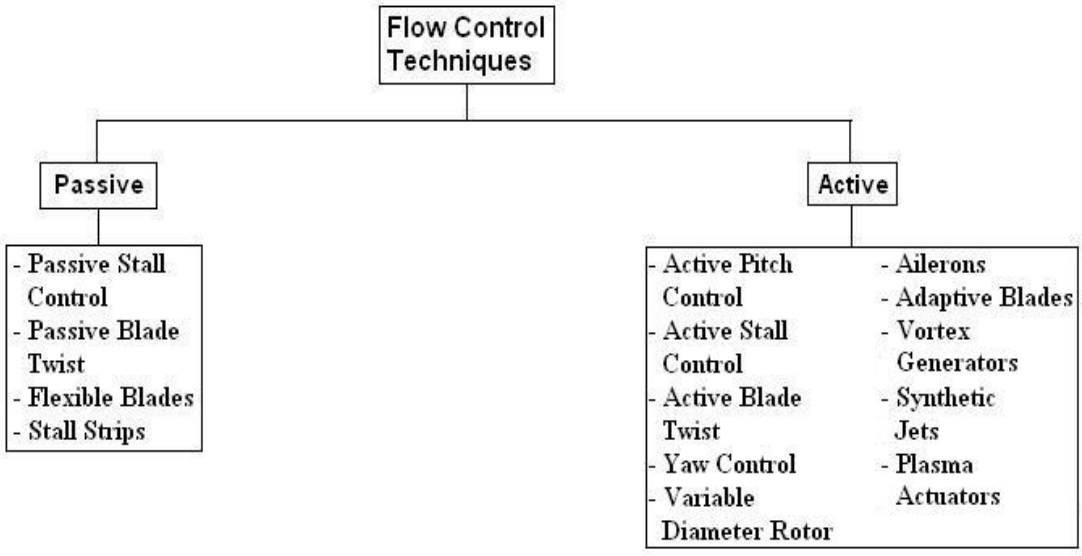

Figure 2.1 Wind turbine flow control

It should be noted that in the context of this project, the term 'power control' is used to imply a limitation of the rotor power during high winds and not the optimization of the rotor to maximize power in the case of moderate winds. The discussion that follows deals accordingly with controlling the flow to control or limit the turbine power.

2.1.1. Passive Flow Control

As the name suggests, passive flow control methods function without the supply of external energy [27]. Passive stall control is the simplest and most common of all such methods. Passive stall controlled blades rely on the intrinsic tendency of airfoil blades to stall, by the separation of the boundary layer on their upper surfaces, at higher angles of attack which are experienced at high wind velocities. The drop in the lift and the rise in the drag of stalled blades limit the power output of the turbines. These blades are designed and their pitches are fixed so as to attain the rated power at the desired wind speed. This method was used with reasonable success by earlier kW-sized wind turbines.

With no additional mechanical components involved, this method provides a cheap and reliable solution. But it comes with the associated uncertainty of the behavior of airfoils in stalled regimes. The contamination of dirt and insects at the leading edge of the blade may result in premature transition and turbulent separation of the boundary layer [28] which, in turn, could result in the wind turbine operating at a low efficiency in normal wind conditions due to premature stall. Moreover, the boundary layer on a profile in rotation behaves differently from that on a translating profile due to the Coriolis and centrifugal forces and often results in stall delay [29-31].

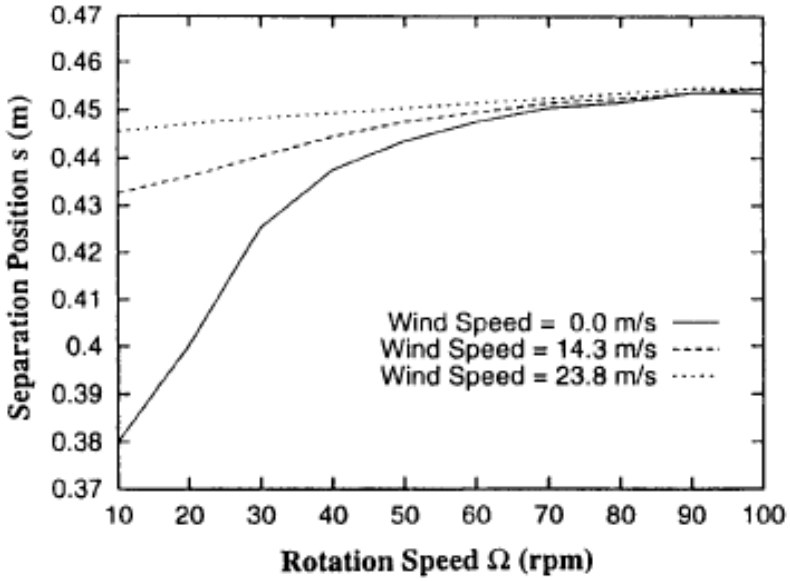

Figure 2.2 Influence of rotation on separation at different wind speeds [30]

Figure 2.2 demonstrates the effect of the rotation on the separation point on a blade element at a particular spanwise position at different wind speeds. The effect of rotation is seen to be more conspicuous at low wind speeds. These difficulties may produce deviations of the order of tens of percent of the maximum power from the predictions, resulting sometimes in the stoppage of these turbines during high winds to avoid any damage. The economic losses associated with this phenomenon are estimated at 15% [29].

Passive blade twist is another flow control technique where the aeroelastic composite blade can alter its spanwise distribution of twist in response to aerodynamic forces. This method is however faced with challenges like waste of energy in normal winds, high costs and reduced structural integrity of the blade [32].

The use of flexible blades, also known as compliant blades, is another passive method where the blades shed the excess power in high speed winds by twisting towards the wind to reduce the angle of attack. Lee *et al*. [33] showed that these blades can eliminate the aerodynamic loads at the source. However, their design is a complex issue and they need a rather large twist to waste enough power for operation at rated specifications. The feathering requirement increases non-linearly from root to tip with a maximum of 30°-40° predicted for the tip by the simulation model.

Another technique is the placement of passive devices like stall strips, which are wedge shaped structures, near and parallel to the leading edge to induce flow separation. The results of Lewis *et al*. [34] showed that stall strips of a sufficient height can induce stall on the suction surface by acting as a trip for flow separation. Nevertheless, issues such as maintenance of tight tolerances between the strips and the blade surface and the possibility that the performance of the blade might be adversely affected by the presence of the strips [35] because of the drag penalty under normal wind-conditions, are serious obstacles to the implementation of this technique.

2.1.2. Active Flow Control

As opposed to passive control methods, active control methods actively modify the flow field by doing work or spending energy to a desired end while avoiding any major drag penalty. This energy has to be provided by an external source. There is a very obvious matter of profitability associated with active flow methods. Their use is justified only when their beneficial effects result in profits, monetary or otherwise, which are greater than the implementation and energy investments necessary for their operation.

An active control system is generally comprised of actuators and sensors placed spanwise over the blade. The sensors are meant to detect any changes that occur in the flow conditions

around the turbine. This acquired data is then transmitted for analysis to microprocessors which respond to the changes by instructing the actuators to apply the required displacements or strains which would counter the adverse effects of the changes [36].

Currently, the most widespread method of wind turbine power control is active blade pitch control [37]. It involves rotating the blade around its pivoting axis, via actuators in the hub of the rotor, so as to decrease the blade's angle of attack with respect to the wind and thus control its lift and hence the power of the wind turbine during periods of high winds. A very similar method to the one mentioned above is active stall control. It is essentially the same principle but the power here is limited by pitching the blade into stall. The sense of rotation is opposite to pitch control and it is sometimes referred to as negative pitch control. These two methods also slow down the rotor because reduced lift and increased drag result in torque reduction for the blades. In a way, power is controlled in this case by a two-fold reduction in i) the blade torque, due to reduced lift and increased drag and ii) the reduced speed of the rotor.

The active pitch controlled blades enable superior control of the power output compared to active and passive stall machines because of greater unpredictability of the behaviour of post-stalled blades and allow operation at almost exactly the rated power. However, both active pitch and active stall control come with the drawback that they require expensive hydraulics or electric stepper motors with complex control mechanisms to position the angle of blades with precision [38]. These methods can add up to a significant fraction of the cost of a lower-power wind turbine, without even considering maintenance costs associated with the mechanism.

Besides the two aforementioned methods, numerous other active flow control devices and methods have so far been employed or are still being developed. These have been summarized in the discussion that follows.

Yaw control is a possibility for power control in small wind turbines generating a few kilowatts. The rotor is yawed out of the wind in order to capture less energy. But yawing results in increase in sound emission and in cyclic stresses on the rotor which could be potentially dangerous because of the possibility of fatigue failure of the entire structure.

Since the electrical power output of a wind turbine is directly proportional to the area swept by the rotor, variable diameter rotors [32] can be effective in controlling the power output. As shown in Figure 2.3, the rotor blade consists of a blade element that is extensible and retractable with respect to the main blade section. Operation at a smaller diameter beyond the rated wind speed would enable to limit the power production. Accounting for all the alterations that this concept would entail in a wind turbine, a reduction of 18% is predicted for the cost of

energy in [32]. With this technique, there are issues like complex control mechanisms and increased weight of the blades.

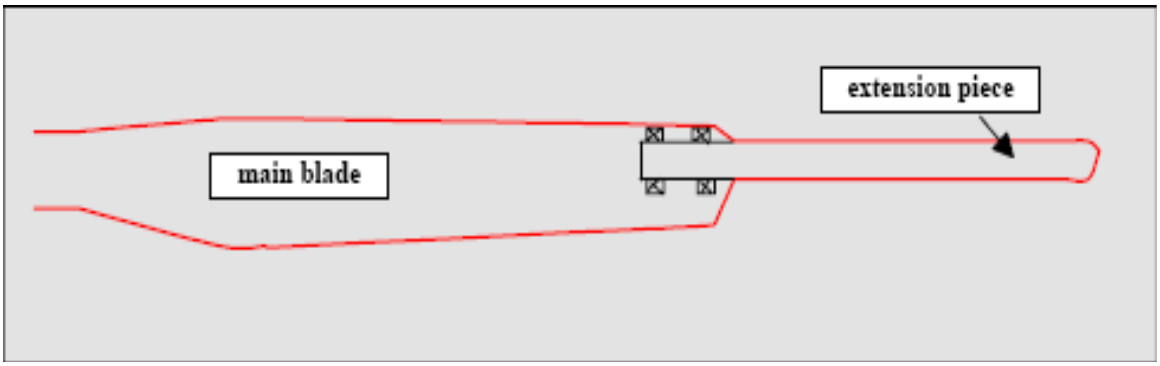

Figure 2.3 Illustration of variable diameter blade concept [32]

Ailerons, which are essentially flaps deployed by applying a moment at their hinges, were studied as an active technique to control lift by Miller *et al*. [39] who obtained interesting results in terms of braking capability with larger ailerons. These flaps can be either a separate entity or a deformable continuation at the trailing edge as shown in Figure 2.4. Studies of Lackner *et al*. [40] show that these trailing edge flaps are quite effective for fatigue load control. Their simulations resulted in reductions between 12 and 15% for the damage equivalent load of the blade root flapwise bending moment. But their effectiveness is subject to the system's ability to react fast enough, by overcoming the inertia of the flaps, to changes in the ambient flow [41]. Moreover, the fabrication of ailerons and the associated actuation and control mechanism can be an unacceptable addition to the manufacturing and maintenance cost of the wind turbine. In addition, the mounting components are subject to wear and tear, the aerodynamic performance of the blade degrades due to an abrupt change in camber and the surface discontinuity can produce unwanted noise and cause stall during low winds [42].

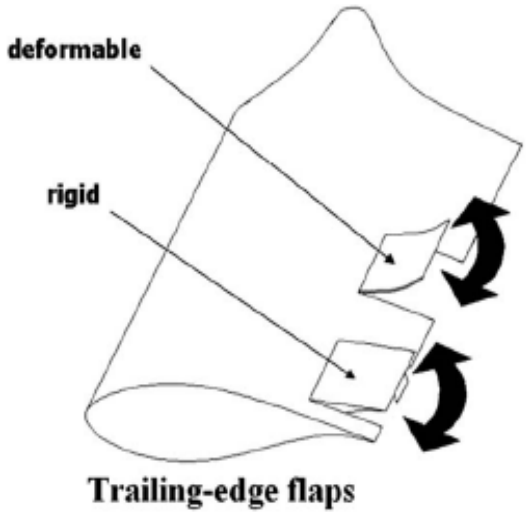

Figure 2.4 Concept of trailing edge flaps [42]

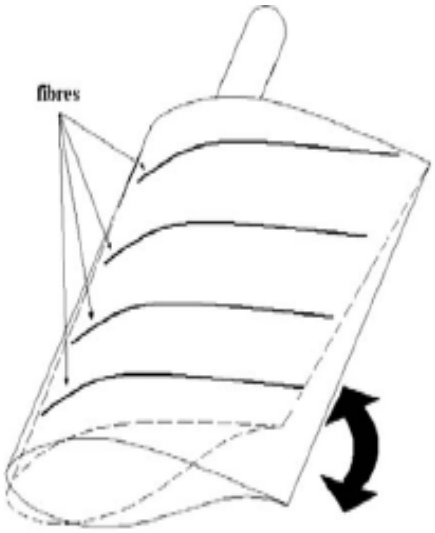

Figure 2.5 Active twist concept [42]

Active twist of wind turbine blades is another way to alter the local angle of attack for power and load control. The effect is shown in Figure 2.5. The twisting is accomplished by active piezoelectric elements present in the blade and it is highest at the blade tip, where it is required the most [42]. This concept is faced with problems like reduced structural integrity, slowness of response due to inertia, high cost of the actuation components and inadequacy of the system to produce the necessary strains. It was shown in [43] that a strain as high as 800μ would be needed to produce a 4° twist at the tip of a 60 m wind turbine blade with a mean chord of 3.4 m and *t*/*c* ratio of 28%.

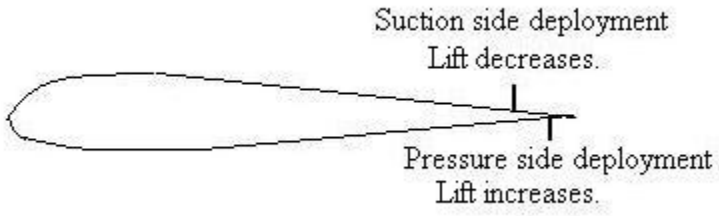

Figure 2.6 Microtab concept

The deployment of Gurney Flaps or microtabs projecting perpendicularly near the trailing edge of the airfoil is another option that has been investigated by van Dam *et al.* [44,45]. The schematic is shown in Figure 2.6. Their deployment effectively changes the camber of the airfoil and thus alters the aerodynamic forces on the blade. If placed on the suction side, they can be used to decrease lift, as is evident from the data in Figure 2.7. But they pose the risk of increased vibrations of the blade by causing unsteady shedding of counter-rotating vortices near the trailing edge. Moreover suction side flaps or tabs have been shown to reduce lift only for low and

moderate angles of attack. They are less effective at higher angles experienced during high winds since the flow has already separated upstream and is not affected by their presence [46].

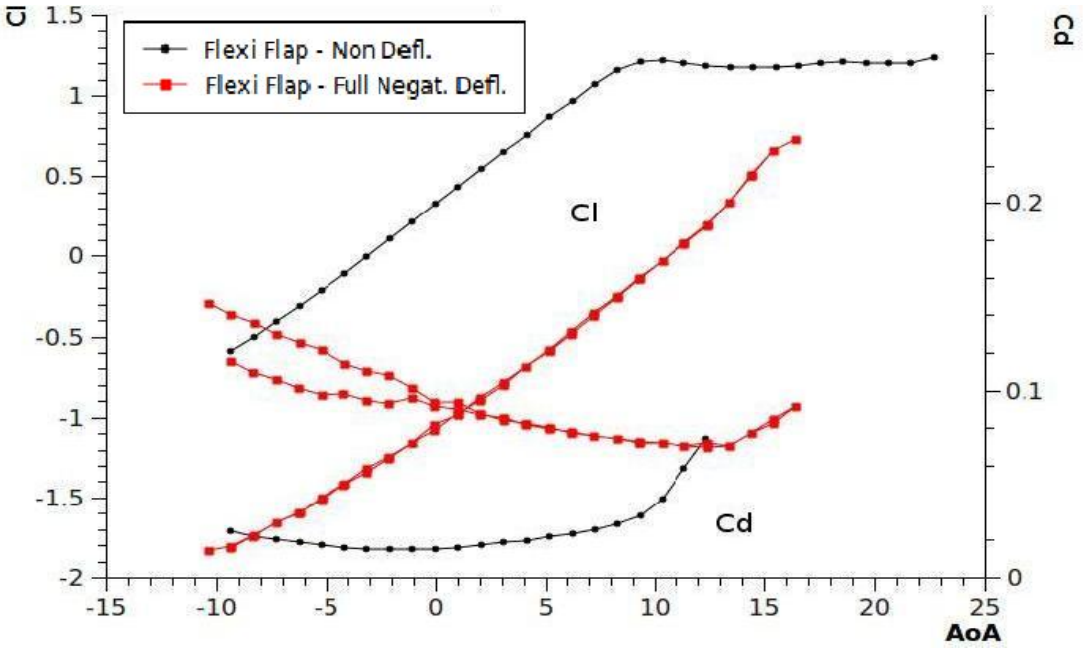

Figure 2.7 Wind tunnel C_l and C_d curves for flap at full suction side deflection [47]

Adaptive blades are blades that are capable of modifying their camber and their overall shape in order to meet the control requirements. In this sense, they differ from actively twisted blades where the observed angle of attack is altered but the blade profile is not. They are similar to compliant blades, discussed in Section 2.1.1, but for the fact that the alteration of the profile is achieved by smart materials, such as piezoelectrics or shape memory alloys, embedded in the blade's skin [48]. This is illustrated in Figure 2.8. A very thin skin section is imperative for this kind of control. Since the strains produced in this case are significant, a thin section may result in a breach of the structural integrity.

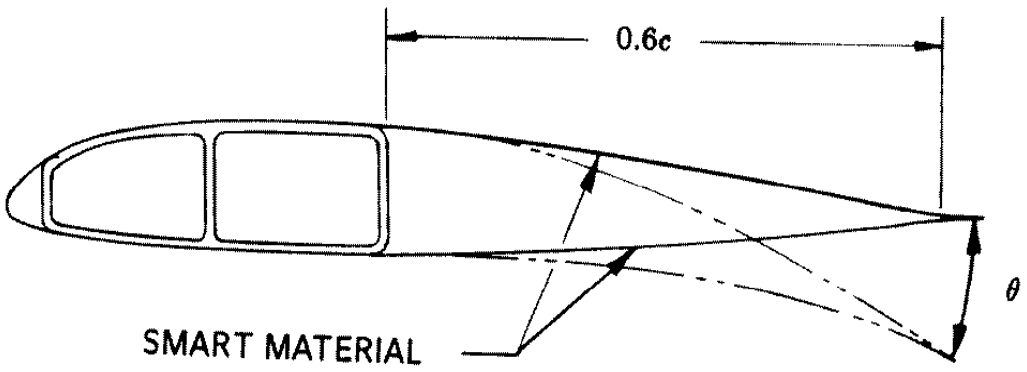

Figure 2.8 Camber control with smart materials [48]

Although they have not been used for load or power control on wind turbines, active vortex generators, which are solid tabs on the airfoil surface, could be an interesting option in this respect. Barrett and Farokhi [49] performed wind tunnel experiments on a two-dimensional wing section to demonstrate a 14% increase in maximum lift, a 2.7 deg rise in the stall angle of attack and 42% jump in lift-to-drag ratio through stall using modern vortex generators. These benefits would have to be exploited by deploying the vortex generators during moderate winds enabling more extraction of power from the wind. Beyond the rated speed, they could be withdrawn to reduce the lift and hence control the power. However, the additional drag would be a significant drawback when the flow has not separated.

Vortex generator jets, which are jets of air coming out of the blade wall, are a similar but less intrusive technique that could be investigated. Figure 2.9 illustrates a schematic of the vortex generator jet configuration. As in the case of vortex generators mentioned above, these jets will have to be functional during normal winds and dormant during strong winds. Results from a parametric study [50] performed with such jets indicate that the level of flow control accomplished depends on the speed, the orientation with respect to the free-stream and the location of the jet with respect to the separation region.

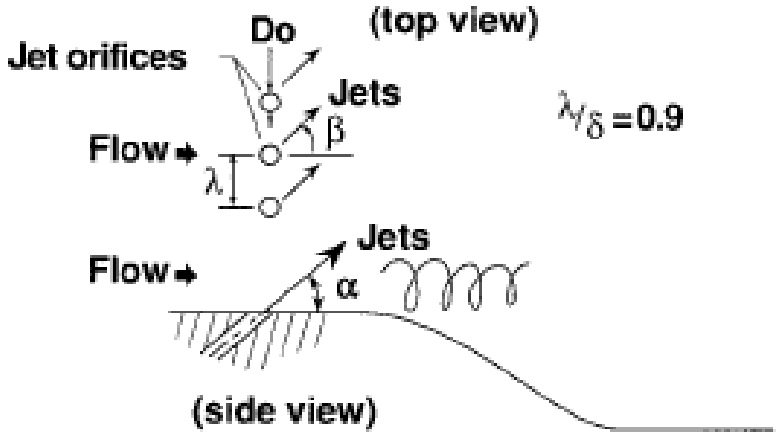

Figure 2.9 Geometry of vortex generator jets [50]

The concept of lift enhancement by the addition of vortices in normal operation and their absence at high wind speeds can be extended to high-frequency micro vortex generators. In this case, vortices are added by the periodic movement of one or more mechanical elements. Lift increase on the order of 10%, drag reduction on the order of 50% and *L*/*D* ratio enhancement of 100% for a high lift airfoil was reported in [51] using these micro-vortex generators. Synthetic jets [52] work in a very similar manner. A schematic of a synthetic jet is presented in Figure 2.10. These jets were found to favour reattachment of separated boundary layers in [53]. The

mitigation of the extent of separation due to the operation of a synthetic jet can be observed in Figure 2.11. These methods are easy to integrate with the turbine blade but need tight tolerances and could potentially create noise.

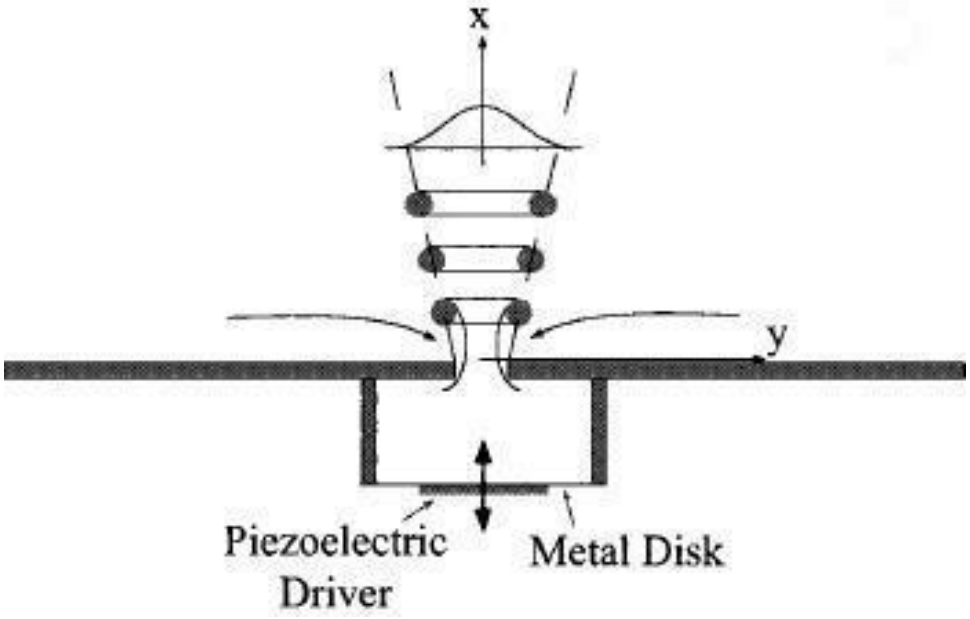

Figure 2.10 Side view of a synthetic jet [52]

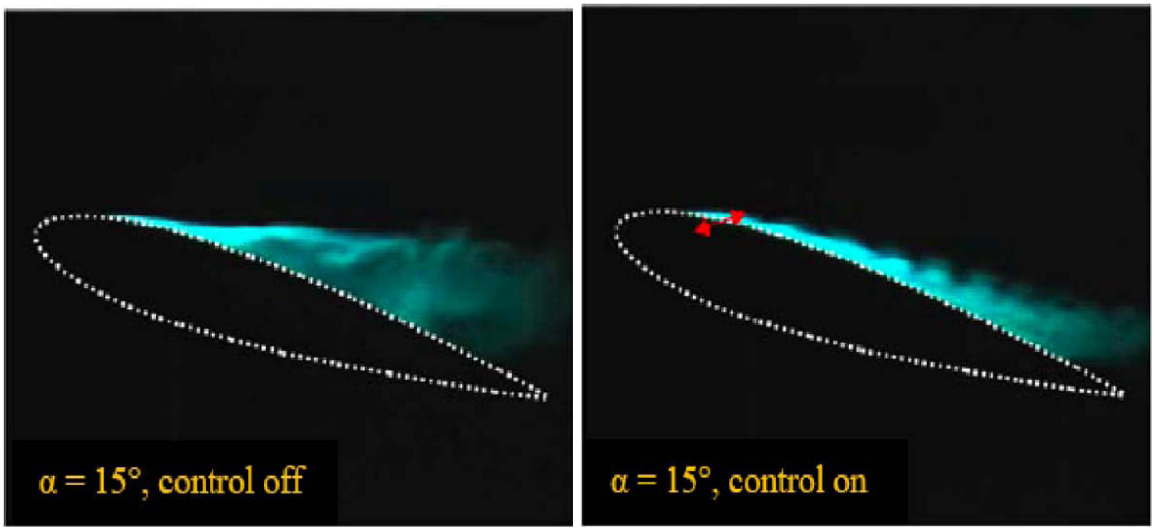

Figure 2.11 Laser sheet flow visualization of synthetic jet operation [53]

Most of the flow control devices, discussed above, have their merits and demerits and are still being researched. Before they are introduced as viable solutions to the problem of wind turbine power control, they need to be improved in various aspects and extensively tested on real wind turbines.

2.2 Plasma Actuation

Plasma actuators are finding newer avenues due to their capability of aerodynamic flow control. This section discusses the efforts for the development and optimization of plasma actuators. An overview of the research aimed at numerical modeling of the effect of actuation is also presented.

2.2.1. Development and Optimization of Plasma Actuator

Before they were introduced into aerodynamics, plasma actuators were used industrially for purposes like ozone generation and depollution of gas streams [54]. Subsequently aerodynamic applications have been tested and developed, the majority of which are based on the enhancement of the performance of aerodynamic profiles as opposed to the present research which seeks to reduce the lifting capability of such profiles. Since its inception, plasma actuation has witnessed extensive research efforts in terms of its optimization as well as its deployment on test surfaces. It finds such wide acceptance owing to its ease of construction, lack of moving parts, low power input, low cost, quick response time and little interference offered to the flow during idle periods due to their thinness.

Plasma actuation has proved to be quite versatile so far. It has lent itself to a large variety of applications because of its ability to influence the boundary layer by means of the wall jet that it induces very near the aerodynamic surface. The impact on the boundary layer is significant because the action of the jet is mostly in the length scale of the boundary layer. Numerous studies have been undertaken with the objective of examining the mechanism behind the production of the plasma body force that influences the boundary layer. In one such study [55], it was found that the magnitude of the force that models the effect of momentum transfer depends only on the electric field strength, ion density (number of ions available per unit volume for acceleration) and plasma volume and not on the density of the neutral particles (unionized molecules of gas). It was seen that all the momentum of the ions is transferred to the neutral particles irrespective of their density.

The majority of the previous work in plasma actuation has been limited to low and moderate Reynolds numbers ($O(10^5)$). This is because of the weak strength of actuation that has typically been achievable. Plasma actuators of strengths ranging from 20 to 40 mN/m have till now produced wall jets with maximum speeds of the order of a few m/s, which is suitable enough only for the modification of flows at low to moderate values of *Re*. The development of plasma actuators of higher strength, capable of inducing larger flow accelerations, is an active area of research.

Balcon *et al*. [56] found that negative sawtooth signals are more appropriate than positive sawtooth signals in terms of inducing homogenous and rapid airflows near aerodynamic surfaces. There have been attempts to enhance the actuation strength by varying different parameters of actuator geometry and configuration. In their study [57], Forte *et al*. observed higher flow velocities for greater lengths of the hidden electrode till a certain extent. It is likely that the increase takes place as long as the length of the hidden electrode is not sufficient for the spread of plasma and saturation is reached when this length is enough to accommodate the fully-expanded plasma.

Ideally, dielectrics having large dielectric constants and small thicknesses should be the best option to induce high values of thrust for a given input voltage [58]. But thin dielectrics come with the downside of having low dielectric strengths due to which the threat of arcing becomes more realistic at high voltages. Consequently, thicker materials are a safer choice for plasma generation despite the fact that they necessitate a higher input voltage. Thicker dielectrics with low dielectric constants end up producing higher values of maximum thrust because of their ability to operate at higher voltages without breaking down. This tendency is observed in Figure 2.12. Recent studies indicate that there has been an order of magnitude increase in the strength of actuators than what was previously achievable and body forces of about 200 mN/m are now possible using thicker dielectric materials of lower dielectric constants and higher AC voltages [59].

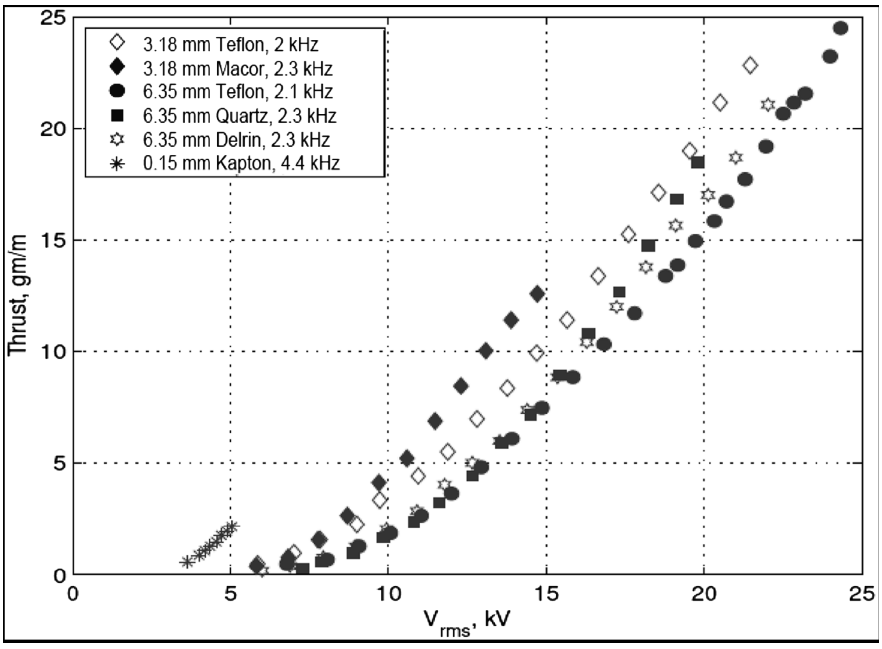

Figure 2.12 Thrust per unit span vs. r.m.s. voltage for different dielectric materials [59]

2.2.2. Counter-Flow Plasma Actuation

Studies on plasma actuators as counter flow devices have been very few and far between. The past research has dealt with counter-flow plasma actuation as just another variant of actuator configurations to be examined in order to achieve the same end as the co-flow actuation, viz. the suppression of stall and boundary layer separation.

Visbal *et al*. [60] were the first to operate the counter-flow actuator. They showed that the counter-flow actuator provided an effective tripping device for a laminar boundary layer developing along a flat plate and used this property to suppress laminar separation over a ramp. They however did measure reduction in the lift coefficient in the case of steady counter-flow actuation.

In [61], a velocity decrease was observed on the suction side of the wake of a compressor blade rotating at two different speeds 600 RPM and 350 RPM with the counter-flow actuator at ¼ chord. The effect of plasma actuation was to remove momentum from the flow on the suction side. The results of Benard *et al*. [62] indicated that counter-flow actuation, as opposed to its co-flow counterpart, was unsuitable to promote any substantial change in the mixing of a jet flow.

In the case of this thesis, counter-flow plasma actuation is always applied to a turbulent flow. In the computational simulations and wind tunnel experiments, the incoming laminar flow is forced to transition at 10% chord length and the actuation occurs some distance downstream. This arrangement is chosen so as not to reduce the plasma actuator to a flow tripping mechanism [60].

2.2.3. Computational Modeling of Plasma Actuator

Despite the rapid advances being made in the technology of plasma actuation, computational fluid dynamics (CFD) will play an instrumental role in the assessment of the capacity of plasma actuation to influence various airflows. It provides an inexpensive alternative in comparison to the building of test prototypes. New configurations of plasma actuation can be evaluated for their effectiveness using CFD before incurring any expenses for wind tunnel or full-scale testing. In order to numerically analyze the effect of plasma actuation, it is essential to have a well-defined model of the body force since the force has to be incorporated in the momentum conservation equations. The following sub-section deals with the efforts that have been made in the modeling of the body force.

The operation of a plasma actuator is simulated in a CFD code by modeling it with a spatial body force field. Several attempts have been made by researchers to develop models capable of closely reproducing the observations from experiments involving plasma actuation.

A study of the available literature indicates that the numerical modeling of plasma actuation has been accomplished primarily using one of two approaches, namely macroscopic and microscopic. The macroscopic models solve the global phenomena that take place during plasma actuation and simulate the momentum transfer to the flow with a spatial body force distribution that can be implemented as a source term in many CFD codes. On the other hand, the microscopic models solve for the effects of plasma actuators considering microscopic effects which include chemical reactions and collisions between ions, electrons and neutral particles.

One of the first efforts to numerically model plasma actuators was undertaken by Massines *et al*. [63]. The variations of the electric field in space and time were calculated along with the electron and ion densities from a one-dimensional model based on the continuity of the charged and excited particles and the Poisson equation. The discharge mechanisms involved were more clearly understood after this analysis. In [64], the time-dependent evolution of the potential and the electric field around two-dimensional objects during a high voltage pulse was studied. The numerical simulation was based on the solution of Poisson's equation on a grid and the determination of the movement of the particles through it.

References [65] and [66] are exercises in the macroscopic or 'phenomenological' modeling of plasma actuator. This approach is more suitable in design and for implementation in CFD. Hall [65] applied plasma actuation as flaps on airfoils and wings using potential flow models as a first-order approach. The discharge physics was not taken into account. A doublet (source and sink) was selected to represent the plasma actuator in a free-stream. The doublet's strength was calibrated using a relationship based on the local velocity at the point of actuation and it was incorporated into a Smith-Hess panel code. The experimental lift enhancement results were successfully reproduced with this model. This model however requires some inputs based on experimental observations in order to model the actuator with reasonable accuracy due to the fact that the actuator properties are not accounted for.

Shyy *et al*. [66] proposed a simple plasma actuator model characterized by a time-averaged (over an AC input cycle) linear two-dimensional body force distribution based on the size of the electrodes was presented. The parameters related to the electrode operation, including the voltage, frequency and free-stream speed, were varied to study the characteristics of the plasma-induced flow and the heat transfer. It was found that the induced flow velocities and heat flux varied proportionally with the applied frequency and voltage and that the electric field was greatest at the inner edge of the electrodes and decreased linearly as one moved away from it. This model was however faced with a few issues. First of all, the properties of the dielectric are

not taken into account. Secondly, the body force field generated by it is very much linear and does not present an accurate enough representation of plasma behavior seen experimentally. In addition, the computed body force strength differs considerably from experimental measurements for given values of voltage and frequency.

Suzen *et al*., in [67] and [68], proposed a more refined model which computes the body force vector by the spatial solution of two additional equations: one for the external electric field (or potential ϕ) due to the applied AC voltage at the electrodes and the other for the charge density ρ_c representing the ionized air. These equations are as follows:

$$\nabla \bullet (\varepsilon \nabla \phi) = 0 \qquad (1)$$

$$\nabla (\varepsilon \nabla \rho_c) = \rho_c / \lambda_d^2 \qquad (2)$$

where ε is the local relative permittivity and λ_d is the Debye length (a plasma property quantifying the extent of shielding of an external electric field from the interior of the plasma). The calculation of the electric potential and the charge density as a function of actuator input, electrode size/thickness and the nature and properties of the dielectric material generates a more realistic body force distribution which is then modulated in time according to the input AC voltage. This model however does not capture the experimentally observed unsteadiness in the plasma over an AC cycle. Figure 2.13 shows the contour plot for the magnitude of the body force in the vicinity of the electrodes computed using the model of Suzen *et al*.

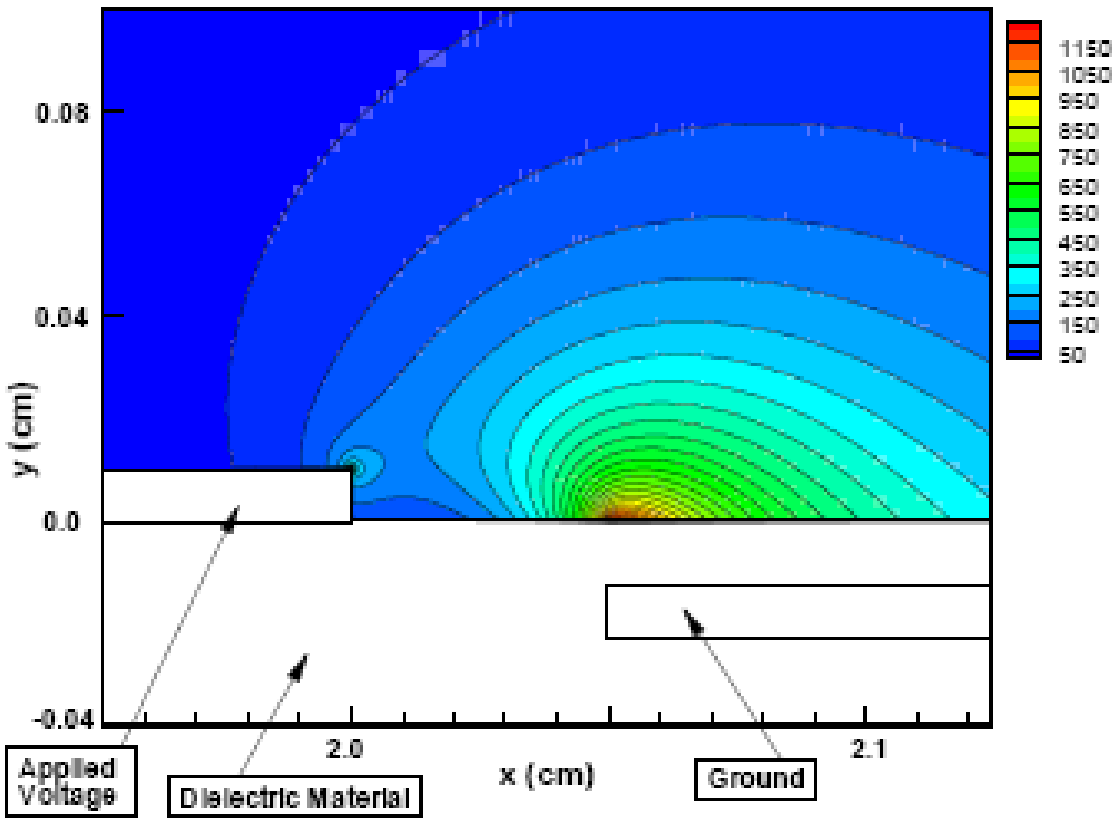

Figure 2.13 Computed body force magnitude contours near the electrodes [68]

In the above figure, the highest magnitude of the body force is seen to be concentrated in the area over the upper corner of the concealed electrode. This is also true for the computed charge density and electric field strength. This finding is consistent with experimental observations of maximum plasma strength occurring in the same region. On the other hand, the model of Shyy *et al*. predicts the existence of maximum force magnitude some distance downstream over the concealed electrode where vertical force vectors, pointing towards the dielectric, predominate.

Orlov *et al*. [8,69] proposed a model incorporating more of the physics that governs plasma generation to obtain a more accurate time-variation of the body force during the AC input cycle. The dynamics of the glow discharge (plasma) region over the encapsulated (hidden) electrode was modelled using a network of electrical elements to obtain a more accurate spatial and time variation of the induced body force along the dielectric surface during the plasma generation cycle. However, the body force distribution resulting from this model was still not very realistic.

There are some more sophisticated models aiming to simulate the working of the actuator on a microscopic scale and involving more complicated chemistry. These models contain

numerous reaction equations with different reaction times and energy outputs. The equations account for reactions amongst the neutral and charged particles in different gases present in the air. The reaction equations are solved with those of fluid motion to obtain the actuator-generated force mostly in the case of a simple one-dimensional dielectric barrier discharge. Font *et al*. [70,71] took into account nitrogen and oxygen reactions in their model of the plasma discharge in the asymmetric plasma actuator. The propagation of a single streamer was shown from the bare electrode to the dielectric surface and back. In [72], the weakly ionized air plasma was modeled as a four-fluid mixture: neutral molecules, electrons, and positive and negative ions. The ionization and recombination processes were included. The charging of the dielectric by electrons during the avalanche ionization process was found to play a crucial role in DBD operation and gas acceleration.

Although modeling of the plasma actuator in micro scales is the most suitable approach to understand its physics, it tends to be very time-consuming and computationally intensive. Its application as a design tool for iterative optimization of plasma actuators and its implementation in CFD solvers to simulate macroscopic aerodynamic flows is not yet a feasible option.

According to Orlov *et al*. [8], for the flow velocities considered in most flow control studies with plasma actuators, the time scale associated with the flow response is six and two orders of magnitude slower than that associated with the ionization process and the AC input cycle respectively. Since the plasma formation process is virtually instantaneous from the point of view of the flow, a time-averaged spatial body force distribution approach can most effectively model plasma actuation. It captures the net spatial effect of the actuation on the flow near surface boundaries and the computational cost remains acceptable. No model has yet been developed which can produce a time-accurate distribution of the body force from the actuator geometry and input. In [63] however, it was shown that the proposed model of the body force could replicate experimental velocity profiles even if the magnitude of the body force may be inaccurate. A better conformation could be obtained with a more accurate body force distribution.

Lemire *et al.* [15] came up with a model which is coded in MATLAB and combines the best features of the models by Suzen *et al.* [68] and Orlov *et al.* [8,69] to simulate the plasma actuator as a time-averaged spatial body force distribution which resembles that obtained with one of the much more sophisticated scientific models [73] but is obtained from an engineering model. The corresponding body force distribution (per unit actuator length) is computed from equation (3), where A is the area of the mesh, after solving the model equations (1) and (2) to obtain the spatial

distributions of the electric potential and charge density on a very fine rectangular mesh. Figure 2.14 shows the time-averaged body force vectors in space.

$$\overline{F} = \rho_c \overline{E} A = \rho_c (-\nabla \phi) A \qquad (3)$$

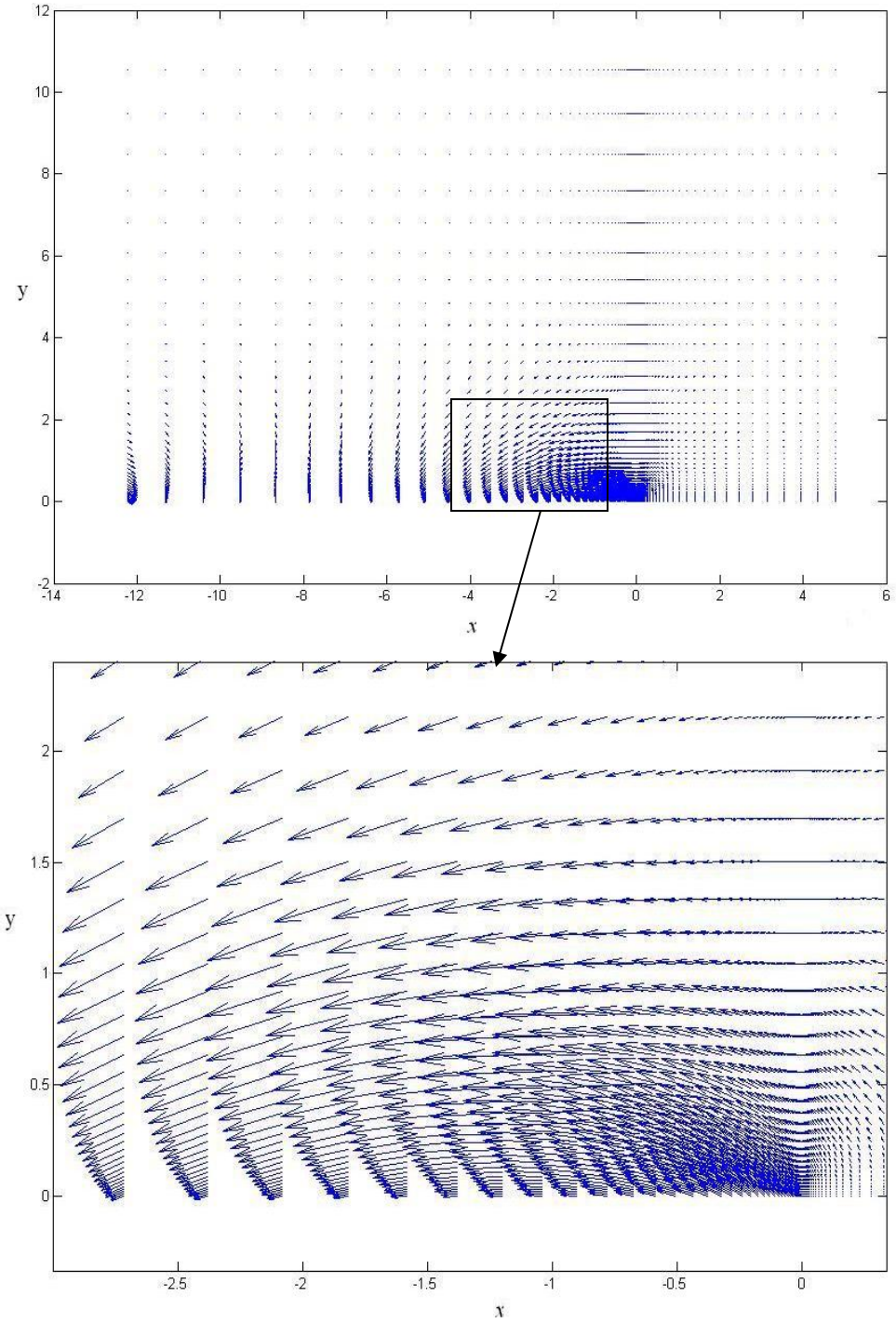

Figure 2.14 Body force field computed with the model of Lemire *et al.* [15]. *x* and *y* are in mm. *x* = 0 is the edge of the exposed electrode and *y* = 0 represents the dielectric surface.

There is some qualitative resemblance between the force fields represented in Figure 2.13 and Figure 2.14 as far as the force magnitudes are concerned. The models of both Suzen *et al*. and Lemire *et al*. predict the occurrence of maximum force strength near the junction of the two electrodes and a gradual decrease in the force magnitude on moving away from this junction.

The force distribution is mapped onto the coarser CFD mesh of the actuator sub-domain in which the plasma actuator is placed using the method outlined by Lemire *et al.* [15]. The body force vectors are then scaled to obtain the desired total induced body force (actuator strength). This model does not claim to be able to exactly predict the spatial force distribution or the force magnitude but it claims to be able to predict a spatial force distribution that is comparable to the time-averaged distribution predicted by a microscopic model.

2.3 Preliminary Assessment of Wind Turbine Blade Lift Control via Plasma Actuation

In a preliminary experimental and computational effort to evaluate the potential of plasma actuation to reduce the lift of a wind turbine airfoil [26], an actuator, injecting in the upstream direction, was installed on the suction side of the blade to induce and control the separation of the boundary layer. Experiments were carried out in a subsonic wind tunnel, at angles of attack in the range 0-15°, for velocities of 12.60 and 16.30 m/s, on a 6-inch chord untwisted 2-D blade having the DU 1996-W-180 profile. Details on this profile can be found in [74]. The plasma actuator was placed at 30% of the chord to induce an upstream flow and sand paper, placed at 10% of the chord, was used to trip the laminar boundary layer so that the flow past the blade would be turbulent as in real wind turbine cases. The aerodynamic balance force measurements showed a modest reduction of the order of 10% for the lift coefficient. Flow fields obtained by PIV demonstrated that depending on the angle of attack, the actuator thickens the boundary layer, induces or amplifies its separation. The CFD simulations reproduced the experimental trends. Figure 2.15 shows the reduction in lift that is observed both experimentally and numerically at an inlet speed of 12.6 m/s.

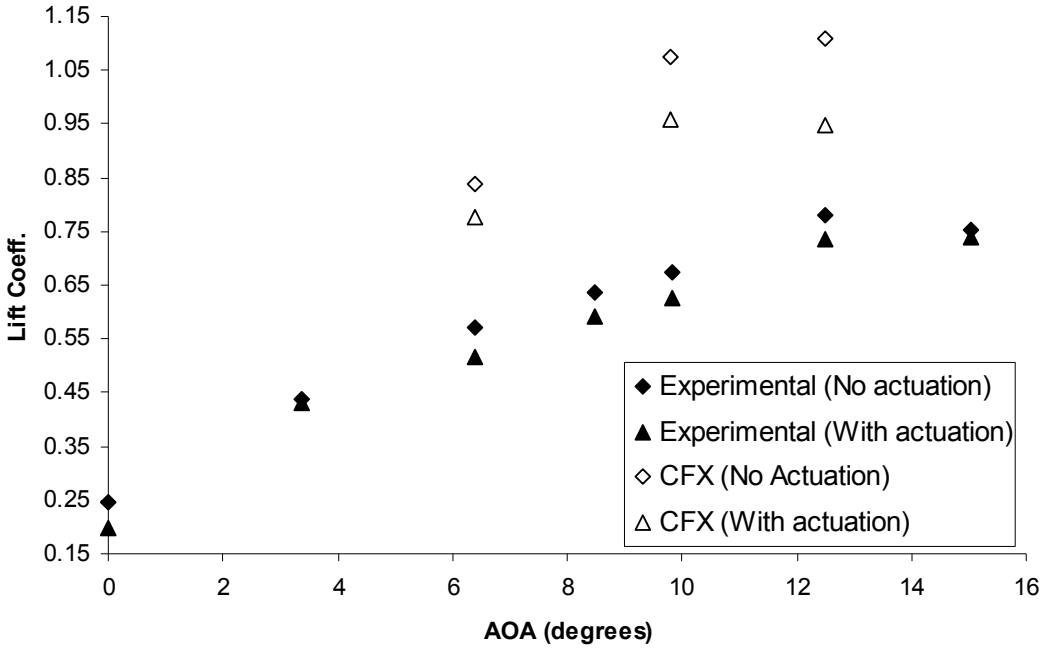

Figure 2.15 C_l vs. angle of attack at 12.6 m/s [26]

This thesis is based on the premise that lift reduction can be achieved by plasma actuation and investigates more thoroughly its potential and applicability in the context of real wind turbines. The behaviour of the flow in response to plasma actuation is investigated for a wider variety of conditions, which will be elucidated in the later chapters of this thesis, and applies to actuators of greater strength in flows of greater Reynolds numbers. The tools used in this project, namely CFD and wind tunnel testing, are the same as in [26] but they are used not only to demonstrate the reduction of lift but also to optimize certain flow parameters which are critical to the effectiveness of the actuator.

2.4 Summary

The literature review in this chapter examines the conventional practices that have been and are being employed to control the loading and electrical power output of wind turbines. Most of the existing techniques are based on the structural modification of the blade in some way or the other. Boundary layer control methods have not been comprehensively tested and applied. This research project aims to investigate plasma actuation as one such method.

The computational modeling of plasma actuation has been reviewed since it is indispensable to the CFD studies for optimization. The model, presented in [15], is chosen for

application in this research project after taking the merits and complications offered by a numerous models into account.

Finally, the preliminary work carried out in [26] is presented because this thesis builds upon the same philosophy. Some promising results were observed in this work, primarily demonstrating the possibility of lift reduction with plasma actuation.

CHAPTER 3
METHODOLOGY

In this chapter, the methodology is described for the following three phases of this research:

1) Numerical study
2) Experimental validation
3) Application in realistic conditions

The numerical study is aimed at simulating flow conditions that can be validated experimentally. The computational domain is a two-dimensional section of the wind tunnel which is used for experiments. The simulations are restricted to low Reynolds numbers and examine the aerodynamic response of the airfoil to plasma actuation under different flow conditions. These tendencies are expected to be present, although to a different extent, at real-scale Reynolds numbers too and give an insight as to how the operation of a plasma actuator may potentially be manipulated to obtain the best results in the course of its application on a wind turbine.

The second phase of this project comprises of the experimental validation of the results obtained computationally. The objective is to authenticate the use of ANSYS-CFX as a reliable tool for analysis of external flows on airfoils and the application of the integrated plasma body force model. The simulated cases in the first phase are all redone in the wind tunnel in the second phase.

The experimental validation of CFX is followed by its application to simulate high Reynolds number flows around full-scale 2-dimensional blades to assess the impact of the plasma actuator in such conditions. The lift reduction requirement is calculated and simulations are executed to predict the strength of actuation that would be necessary to achieve these levels of lift drop.

The wind turbine airfoil that is tested here is DU 96-W-180 [74]. This particular profile has a maximum thickness that is 18% of the chord length. It is a relatively thin member of the DU series of wind turbine airfoils and has a sharp trailing edge which makes it suitable for use at outboards of wind turbine blades. Given that the airflow past the blade has the least tendency to separate at its outboard and that the outward blade elements are the major contributors to wind turbine power, it is here that the conditions are the most adverse for plasma actuation to induce

separation. For this reason, this study focuses on the potential impact of plasma actuation at the blade tip.

Choice of Angle of Attack

The choice of angles of attack to be examined is critical to the numerical and experimental study. Figure 3.1 shows the typical variation of the angle of attack encountered by the tip of the blade of a wind turbine which operates at a constant tip-speed ratio (the ratio of the rotational velocity of the tip to the far-stream velocity) $\lambda=7$ for wind speeds less than 12.5 m/s and switches to constant speed rotation for speeds in excess of this value.

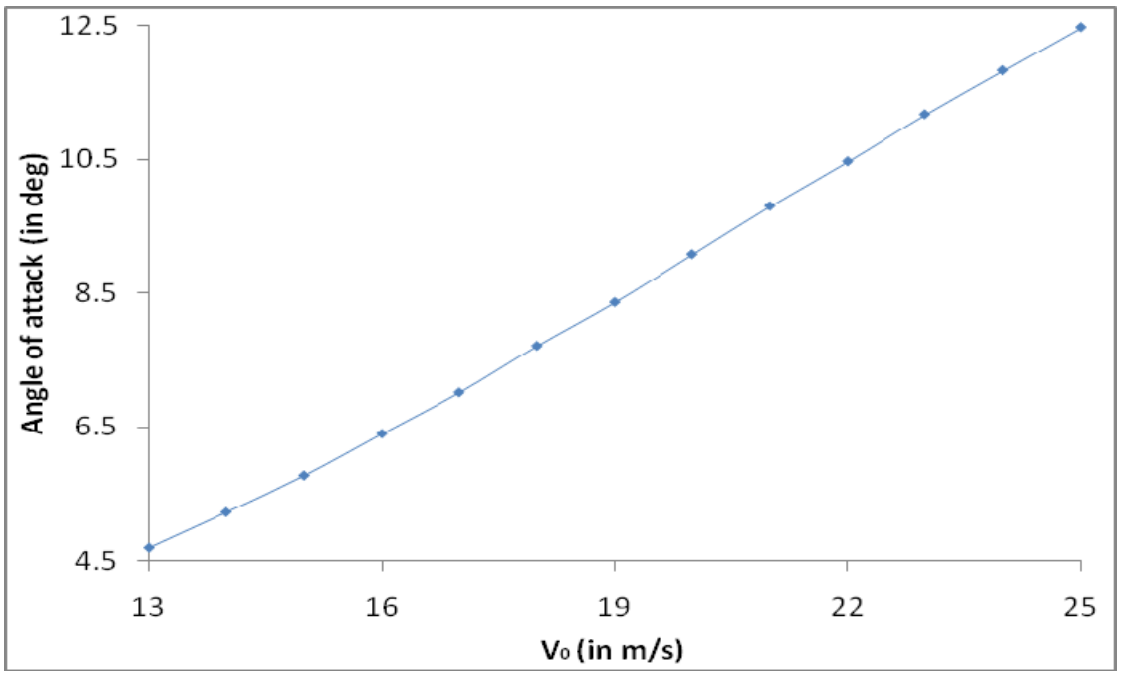

Figure 3.1 Angle of attack variation vs. far-stream speed

It is seen that its variation with far-stream velocity is quasi-linear for operation in the regime of constant rotational speed where the need of power control arises. These values have been calculated from the inverse tangent of the ratio of the cross-plane velocity (which is less than the far-stream velocity by the axial induction factor) and the in-plane velocity (which is more than the rotational velocity by the angular induction factor) at the blade tip. These two factors have been determined by using the iterative Method 2 with initial guess values obtained graphically from Method 1, as described in the sub-section 'Solution Methods' in [2].

6.4 deg, 9.8 deg and 12.4 deg are the three angles of attack chosen for the computational analysis. From the figure, it is evident that these angles nearly correspond to the speeds 16 m/s, 21 m/s and 25 m/s respectively. This permits the computations at these angles to simulate the

flow at these far-stream velocities which are typical in the regime of power control. However, the Reynolds number for the computations is limited due to reasons discussed previously.

In addition, these angles are also representative of three different flow regimes for the DU96-W-180 profile at the Reynolds numbers being examined. 6.4 deg is an angle of attack for which the flow remains attached and the lift curve is linear. At 9.8 deg, the linearity is lost and the blade begins to stall. The 12.4 deg angle indicates a stalled airfoil. The selection of these angles allows the investigation of the behaviour of the flow and its response to plasma actuation in these three regimes.

3.1 Numerical Study

The effect of plasma actuation on the flow past a two-dimensional airfoil section of the wind turbine blade is studied by means of CFD simulations performed in ANSYS-CFX. The CFX solver is chosen as the computational tool because it is known to produce good results, close to XFOIL (a foil and wing analysis code) predictions, for 2-D aerodynamic analyses. It is also a good solver for transient conditions.

Since the CFX solver is incapable of two-dimensional simulations, a 2-D rectangular x-y grid with an extremely small extrusion in the z-direction is used as the mesh. Figure 3.2 illustrates the CFD model used for the flow simulation. The model is essentially a thin section of the wind tunnel flow set-up with the airfoil surface and the upper and lower walls of the test-section modeled as no-slip walls. The height of the domain is 2’ which is same as that of the test-section and the blade chord is 8” which is same as the test blade. The inlet of the wind tunnel is modeled with a total pressure inlet boundary condition. The wind tunnel outlet is a mass flow rate boundary condition corresponding to the velocity under consideration. All meshes used for the computations are structured and have nearly 150000 hexahedral elements with high grid density near the blade surfaces as shown in Figure 3.3. Separate meshes were created for the different combinations of angle of attack and actuator location. In the model, free-slip (no shear) walls are added upstream of the no-slip walls as a substitute for the contraction section that leads up to the test section. This adjustment results in better convergence of the simulations and does not affect the flow on a fluid dynamics basis since the flow continues to remain parallel and the no-shear walls offer no resistance. Laminar-turbulent boundary layer transition is forced at 10% chord on the suction side since the flow becomes turbulent a short distance downstream of the leading edge and remains turbulent for the rest of its passage over the blade. The shear-stress-transport (SST) turbulence model has been applied in all the simulations because of its general

acceptance as the most accurate model for aerodynamic applications. This model is more capable of correctly representing boundary layer separation compared to the *k*-ε model.

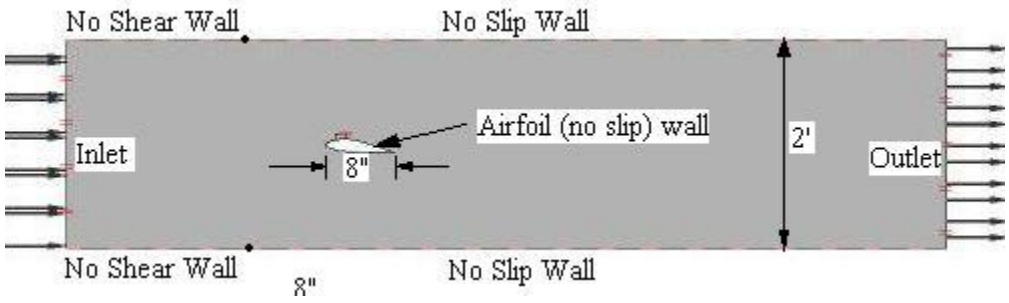

Figure 3.2 CFD domain used in simulations

The numerical results in this thesis are subject to uncertainty due to the discretization error of CFX. This uncertainty is essential to assess the accuracy of the numerical results and their degree of reliability. For the purpose of this research, these errors are estimated using the 5-step procedure proposed by Celik *et al*. [75]. First of all, a representative or average cell size *h* is defined for a mesh. Then the same simulation is executed using three meshes, with varying number of grid elements, in the same computational domain such that the refinement factor $r = h_{coarse}/ h_{fine}$ is in excess of 1.3. This is followed by the calculation of the order *p* of the method and eventually leads to the grid convergence index (GCI) which is the CFD equivalent of error bars in experimentally measured data [75]. All the CFD results in this thesis represent the solution from the finest grid. Since all the data points in the Chapter 4 graphs which show CFD results are obtained from separate simulations and running every such simulation for 3 sets of grids would have used up a lot of computational time and memory space, the error analysis was performed for only one of the several x-coordinate settings in each graph. This helps us to quantify the uncertainty in one of the cases and gives us an idea of the level of uncertainty in the remainder of the cases because they all have the same number of grid elements.

Figure 3.3 presents an enlarged view to show the blade section and a sub-domain on its suction side where a momentum source, derived from plasma actuation, can be implemented.

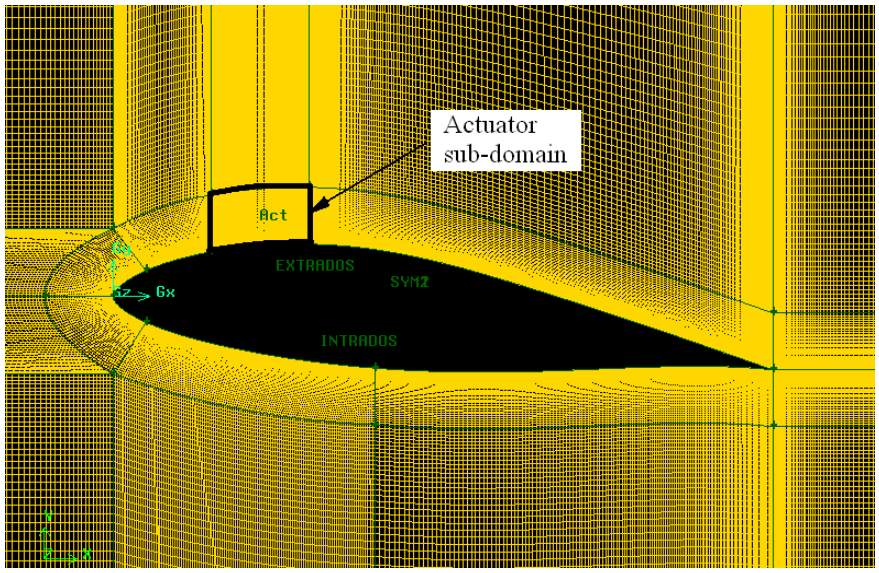

Figure 3.3 Sub-domain for plasma actuation

Since boundary layer separation is an unsteady phenomenon, all the simulations are performed in the transient mode and the results are averaged out over several oscillations when the simulations reach convergence. For each simulation, a steady-state run is first carried out without actuation. The resulting flow field serves as the initial condition for the subsequent transient simulation without actuation. This, in turn, provides the initial condition for the subsequent transient computation with implementation of the plasma actuator model.

The selected actuator model for the present study is that proposed by Lemire *et al.* [15]. This model is chosen because it is not as computationally intensive as the microscopic models and is capable of producing a realistic body force distribution similar to microscopic models. The model is implemented in a Matlab code that produces a time-averaged spatial body force on a very fine Cartesian mesh.

The body force distribution is then transferred to a coarser CFD mesh for implementation into ANSYS-CFX. The body force on the plasma actuator mesh is mapped to the CFD mesh using the algorithm written by Lemire *et al*. [15]. Figure 3.4 shows the distribution of the transferred body force after mapping to the mesh in the actuator sub-domain. The coordinates are expressed as a fraction of the chord's length with the origin at the leading edge and the horizontal axis being parallel to the chord. This body force distribution is then implemented in CFD simulations by using the User Fortran option in ANSYS-CFX. The actuation strength acts as an important parameter with the potential to influence the ambient aerodynamic flow since the effectiveness of a plasma actuator was found to be proportional to its strength [15]. In the

simulations, the desired strength setting is achieved by using a scaling factor for the vector force field.

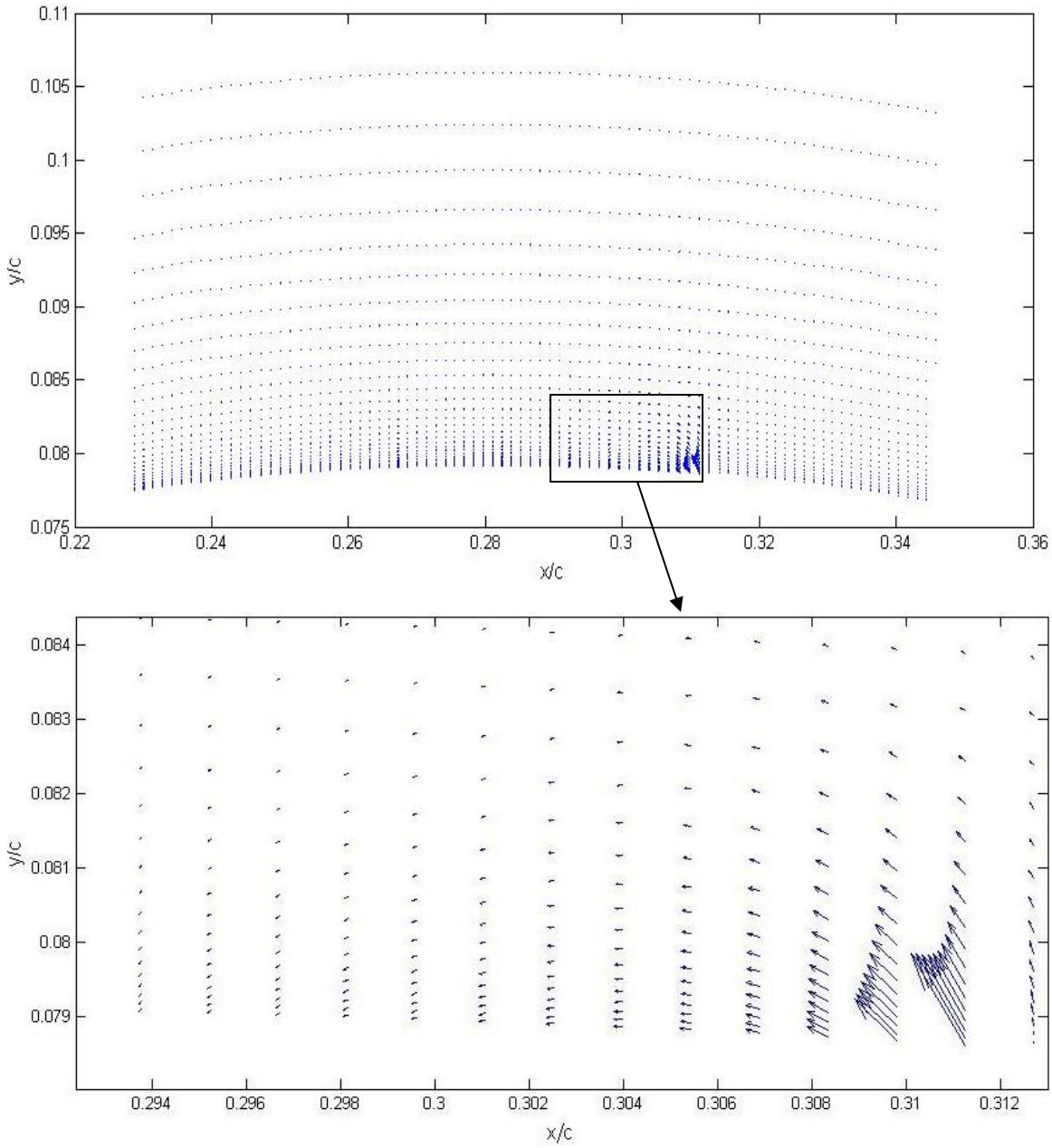

Figure 3.4 Plasma force distribution (a) over sub-domain, (b) zoomed near the edge of the exposed electrode

Since the maximum actuation strength that is so far practically achievable is nearly 200 mN/m, the computations do not implement body forces greater than this. In fact, the maximum simulated actuation strength is 150 mN/m so as to be nearer the greatest body force that can be generated with the available plasma actuation set-up without causing damage to the Plexiglas

dielectric. The velocities investigated in this study do not exceed 30 m/s although wind speeds of 75 m/s to 100 m/s are commonly encountered at the outboard of a blade of a MW-class wind turbine. The reason is that the currently available actuation strength is not sufficient to make any discernable changes to such high free stream flows.

The numerical simulations are carried out to:

1) Assess the effect of plasma actuation on the lift coefficient with the variation of the actuator strength from 0 to 150 mN/m (as in a CFD study) at a fixed angle of attack, chordwise location and velocity.
2) Determine the change, from plasma actuation, in the lift and drag coefficients as a function of the Reynolds number based on inlet velocity for a given angle of attack (= 9.8 deg). This series of tests is carried out for two settings of actuation strength, 30 mN/m and ~150 mN/m.
3) Optimize the actuator's chordwise position. These tests are carried out for three different angles of attack, 6.4 deg, 9.8 deg and 12.4 deg. At each of these angles, different positions of the actuator are tested for their effectiveness at two incoming velocities, 12.5 m/s and 30 m/s.

3.2 Experimental Study

3.2.1. Experimental Set-Up

This sub-section gives an overview of the experimental set-up used for measurements of lift and drag and also describes its individual components.

Assembly

The entire assembly, comprising of the blade mounted on the shaft and shielded by the aerodynamic sleeve, is shown in Figure 3.5.

The set-up inside the wind tunnel appears as in Figure 3.6. It shows the scale of the blade and the supporting components in comparison to the dimensions of the wind tunnel. Both the weighing balances are placed inside a box and the whole assembly is isolated from the surroundings.

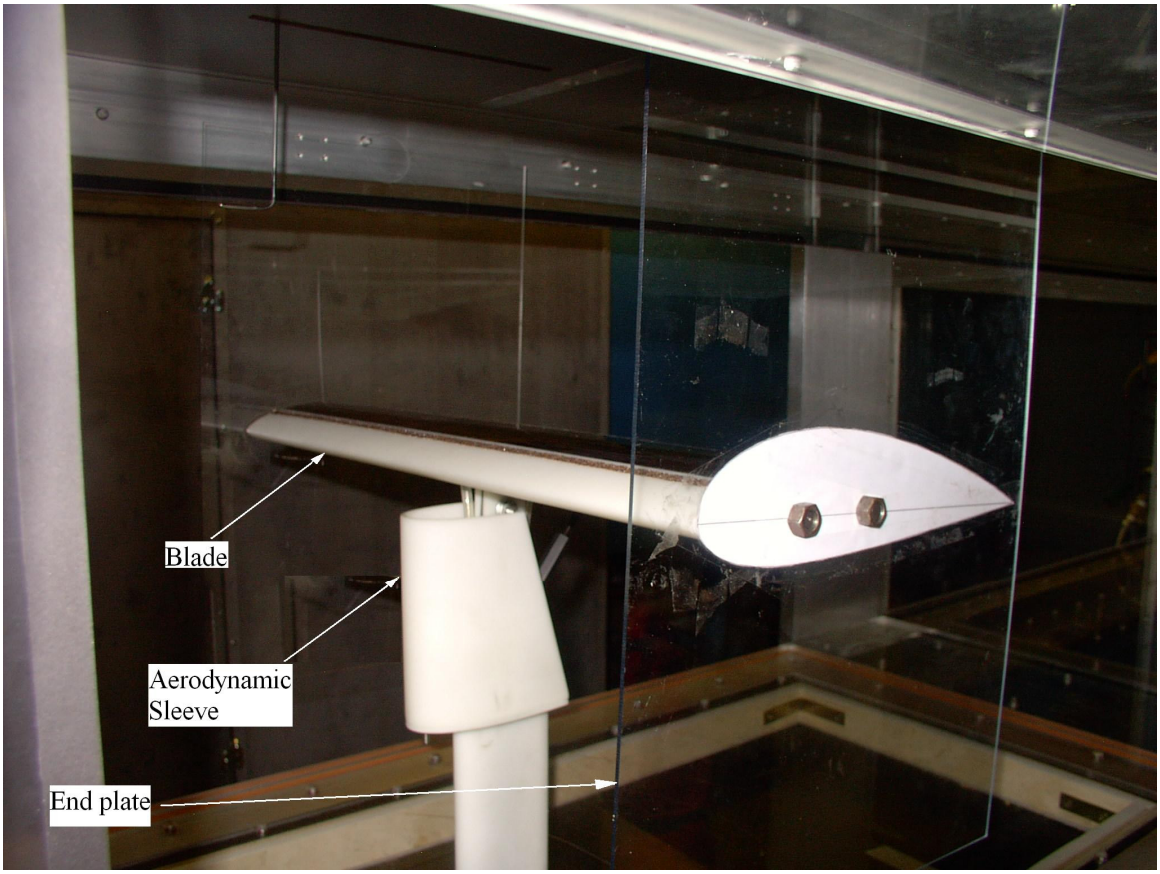

Figure 3.5 Assembly of all parts in the wind tunnel

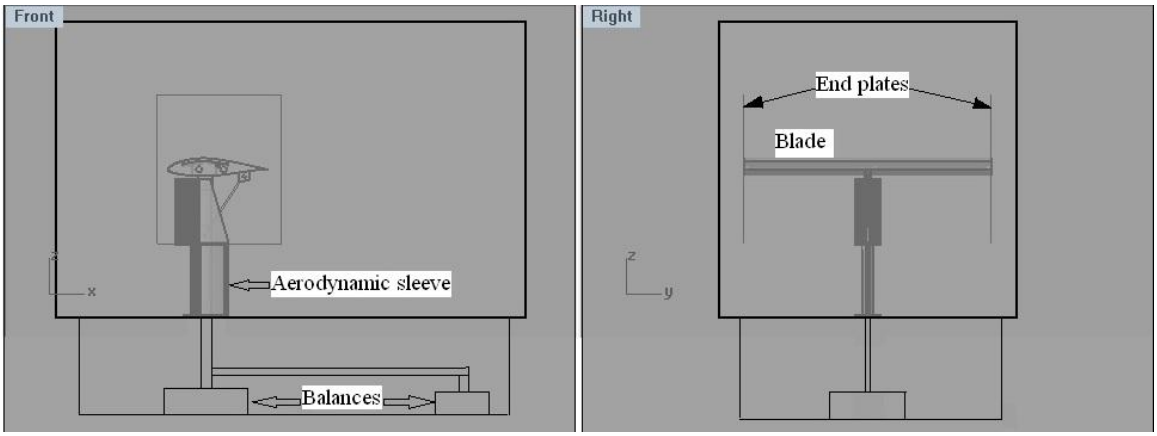

Figure 3.6 Set-up inside the wind tunnel

Aerodynamic sleeve

In order to minimize the drag acting on the mast and the plasma actuator wires, they are surrounded by a sleeve having an aerodynamic shape and made of the same resin as the main blade body. It is screwed into the base of the test section floor. In this way, most of the extraneous drag is transferred to the test section floor and does not feature as a part of the blade

drag. The profile used for this sheath is NACA0024. This profile is chosen for its symmetricity so as not to disrupt the symmetric nature of the approaching airflow and for its thickness so as to accommodate the mast, the wires and the end-fitting turnbuckle which is a part of the linkage to vary the angle of attack. The upper half of the sleeve has a cross-section of a truncated airfoil in order to enable and make room for the connection of the turnbuckle to the mast.

Plasma generation system

The system for plasma generation was developed based on the specifications of the system proposed by Thomas *et al*. [59]. This system is composed of a signal generator, power amplifiers, a resistor module and transformers. The sawtooth high voltage AC waveform is generated by the signal generator. Two Crown XTi-4000 Power Amplifiers, each consisting of two channels, are used to supply high power. The channel outputs from each amplifier are then connected to two different transformers via the resistor module which consists of four ballast resistors (2 Ω, 300 W). The two CMI-5525 transformers, made by Corona Magnetics, have a turns' ratio of 360:1 and a maximum output of 25 kV_{rms} each. The two transformers are connected in parallel to obtain a total voltage amplification ratio of 720:1. During plasma generation, the amplification ratio is set at the same value for both the amplifiers so that the peak-to-peak voltage can be obtained by simply doubling the amplitude since the outputs from the two transformers are out of phase. The actuator should be operated for a very brief duration when the force nears its saturation value. Otherwise, the filamentary discharges may result in the breakdown of the dielectric. The main components of this system are placed in a standard equipment rack as shown in Figure 3.7.

Figure 3.7 Plasma generation system

Wind Tunnel

All the experiments are performed in the Gottingen–type subsonic, closed-loop wind tunnel (ELD Inc., model 407-B) of the École Polytechnique de Montréal. The maximum airflow speed that can be simulated in this wind tunnel is 91 m/s. The cross-section of the wind tunnel test section is 2 ft × 2 ft and its length is 8 ft. The free-stream turbulence level specification is of the order of 0.25%. The inlet air speed is regulated by adjusting the frequency of the variable speed AC induction motor which powers the axial fan of the wind tunnel. During the test, the temperature is held constant by means of a cold water cooling system mounted in the wind tunnel upstream of the test-section. The floor of the test-section has an orifice which permits the passage of a vertical shaft and actuator wires. It also has holes to screw in place the aerodynamic sleeve.

Test Blade

The blade is an extrusion of the DU96-W-180 airfoil profile. It has a chord of 8” and a span of 20”. It is an assembly of two parts – (i) the blade body which is fabricated by stereolithography (a rapid prototyping technique) using the ABS-like nano-composite

photopolymer DSM Somos Protogen 18420, and (ii) the ¼”-thick curved Plexiglass dielectric which forms the suction surface of the blade and extends from 15% to 60% of chord length. The geometrical details of the blade body, including hidden features, can be seen in its CAD model as shown in Figure 3.8. The chordwise extent of the dielectric was limited by practical considerations arising from the downscaled blade since the blade thickness diminishes as we approach the trailing edge and it is difficult to accommodate a ¼”-thick dielectric in that region without compromising the structural integrity of the blade. This would not be a major problem in a full-scale wind turbine blade where more blade thickness would be available.

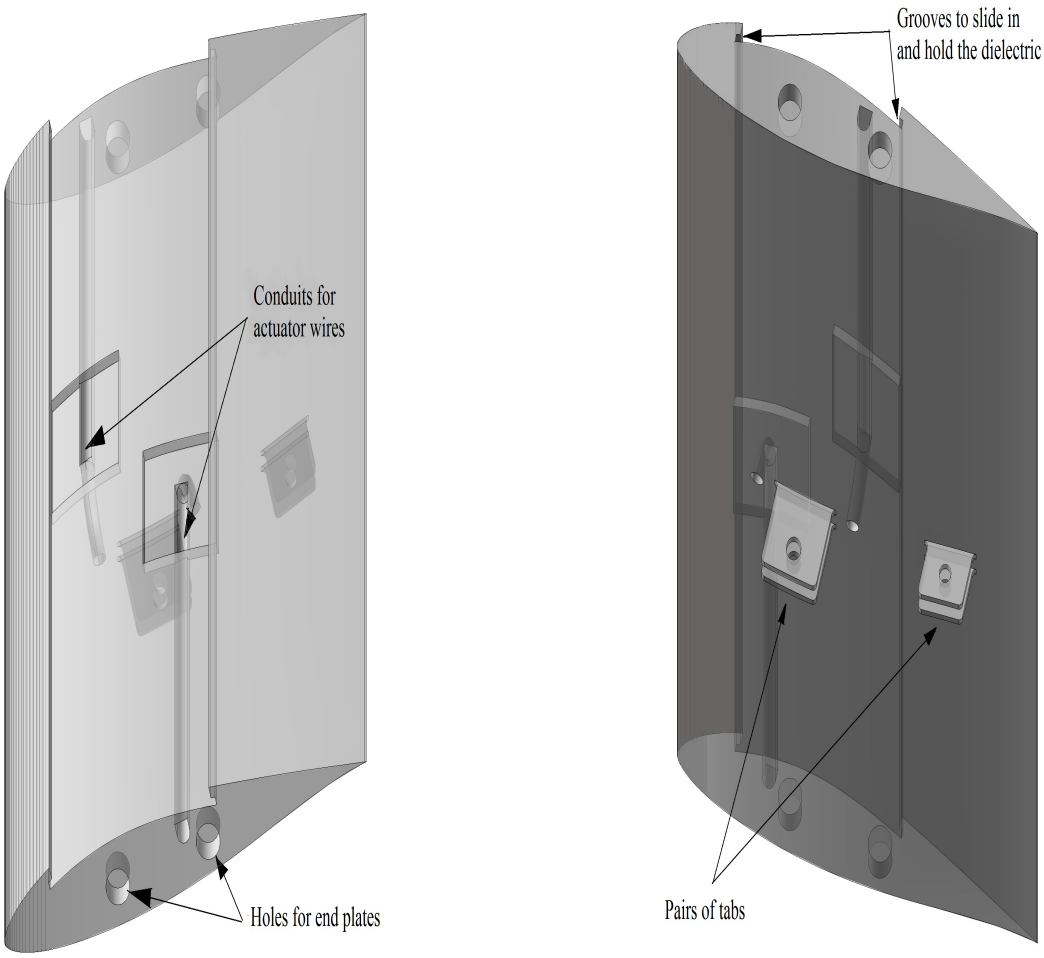

Figure 3.8 (a) Blade body's suction side, *(b)* Blade body's pressure side

The dielectric is inserted in the main blade body by sliding it along the span so that it fits into grooves that have been built into the main body. Figure 3.9 illustrates the side view of the blade fitted with the Plexiglas plate.

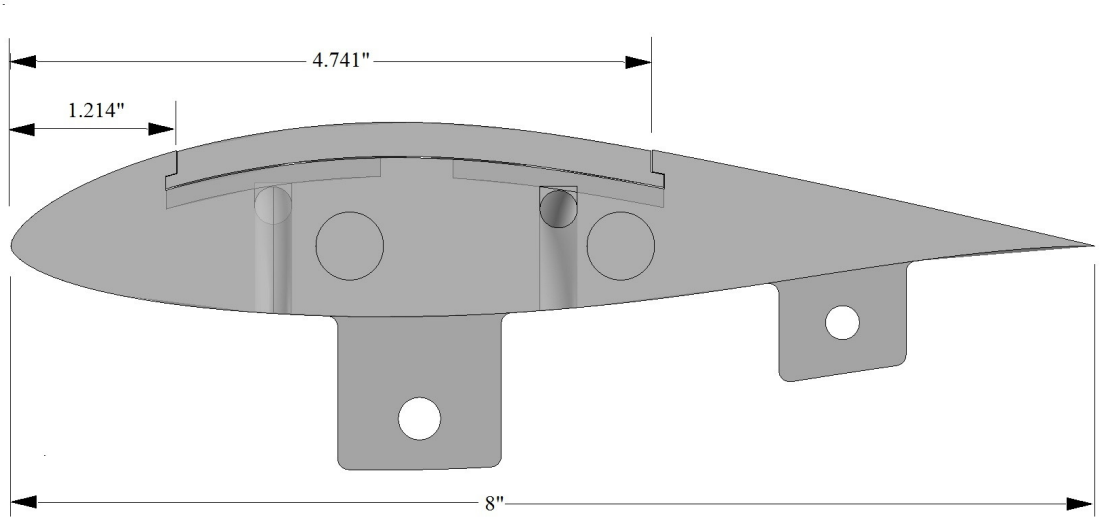

Figure 3.9 Side view of the blade

Glass plates are attached at the two tips of the blade to minimize the three-dimensional effects of the wing tip vortices. Two high-voltage and flexible wires run spanwise halfway through the blade from opposite blade tips, where they are soldered to the actuator electrodes, and exit the blade through openings at the mid-span on its pressure surface. The pressure side of the blade also has two pairs of tabs at two different chordwise positions, as shown in Figure 3.8 (b). The pair of upstream tabs has holes for a bolt through which it is propped on the mast. All the holes in the blade are filled with metal inserts of the appropriate size so that no wear and tear is caused by friction from the rotation of the corresponding screws.

The wind tunnel velocities in the tests will be limited to 30 m/s. The operation is therefore restricted to a chord Reynolds number of almost $4x10^5$ which is quite close to the transition Reynolds number. This implies that the flow over the airfoil would be laminar for most of its passage over the blade. In reality, the flow passing over a full-scale wind turbine airfoil becomes turbulent very soon after it has passed the leading edge. To force the transition of the laminar boundary layer to obtain a flow similar to the one observed over a real blade, a strip of sand paper is used. For a blade operating at a typical chord $\mathrm{Re} = 3\times10^6$, the transition could occur at around $\mathrm{Re}_x = 3\times10^5$ (approximating the airfoil as a flat plate), i.e. at around 10% of the chord length. For this reason, the sandpaper is installed on the suction side at 10% of the chord from the leading edge while the plasma actuator is placed downstream. If the actuator is not placed in the turbulent boundary layer region, its influence might be to trip the boundary layer resulting in momentum addition to the flow and its subsequent reattachment. The main effect would then be an augmentation of the C_l, which is not desired.

The blade, fitted with the dielectric can be seen in Figure 3.10.

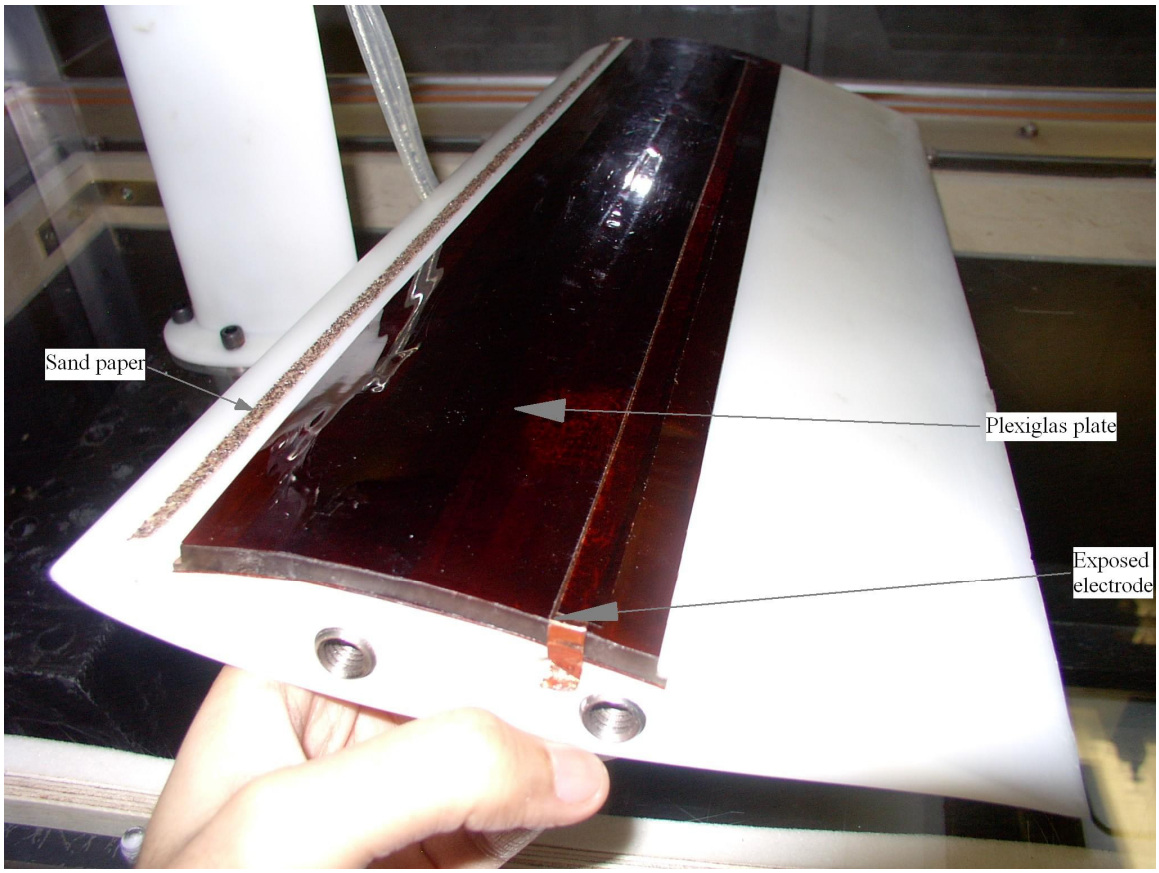

Figure 3.10 Blade fitted with dielectric

Angle of Attack Variation System

The centerline through the holes in the pair of upstream tabs serves as the pivoting axis of the blade to vary the angle of attack. The variation is achieved by a link of adjustable length, one end of which is attached to the mast and the other end is attached to the downstream pair of pressure side tabs on the blade by means of screws. This link is comprised of a turnbuckle having a jaw-type end fitting, a coupling nut and a rod end as shown in Figure 3.11.

The angle of attack can be increased by reducing the length of this link. The angle of attack is ascertained by measuring the tilt of the chord from the horizontal with the help of a Mastercraft digital inclinometer which has a resolution of 0.1 deg.

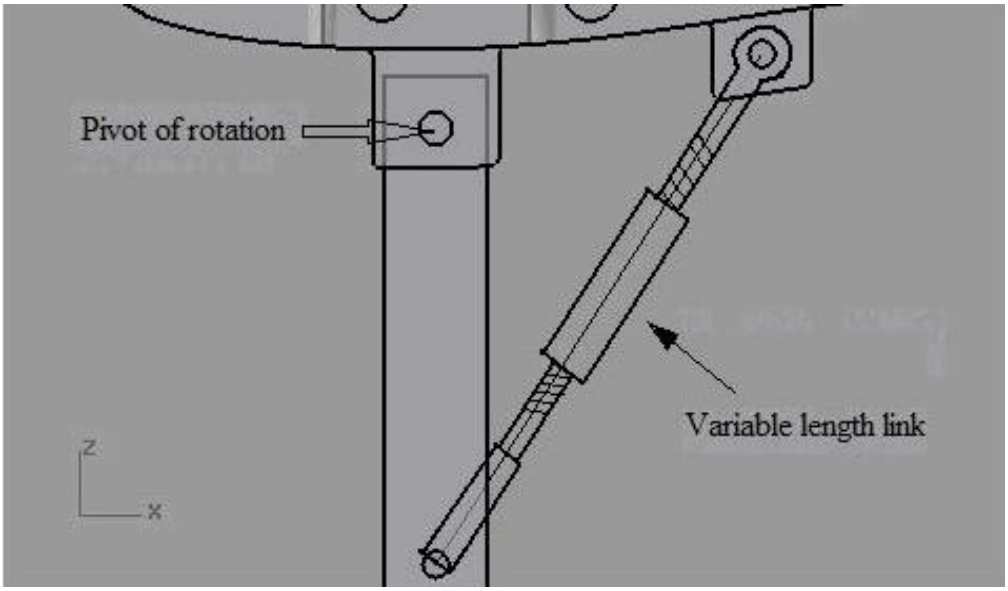

Figure 3.11 Variation of angle of attack

Vertical Shaft and Weighing Scale

The shaft, on which the airfoil blade is propped up, is a part of an L-shaped aerodynamic balance, shown in Figure 3.12, which is used to obtain the lift and drag forces experienced by the blade.

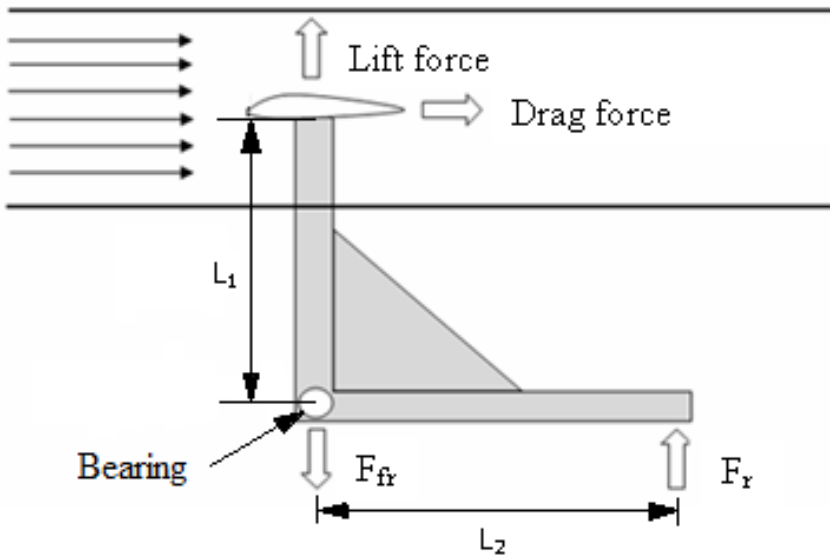

Figure 3.12 Balance for measurement of aerodynamic forces

The two measured forces, F_{fr} and F_r, are obtained from a CTS 3000 scale (capacity: 30 kg, resolution: 1 gram) and a STARFRIT scale (capacity: 5 kg, resolution: 1 gram) respectively. Force and moment balances result in the following relations for lift (L) and drag (D):

$$L = F_{fr} - F_r \qquad \text{and} \qquad D = (L_2/L_1)\, F_r .$$

The drag thus calculated is corrected by subtracting from it the drag due to the objects in the test-section apart from the airfoil blade such as the shaft and the angle of attack variation link. This drag is measured for all the velocities that have been reported in this thesis. It is obtained by removing the blade and running the wind tunnel with the remaining components in the test-section. Another correction is made to account for the moment due to the non-alignment of the center of lift with the vertical shaft. The chordwise position of the center of lift is calculated numerically using XFOIL and used with the experimental force measurements to determine the drag.

3.2.2. Plasma Actuator

A cross-section of the dielectric, which will fit into the main blade body and the electrodes (not drawn to scale) on both its sides, is shown in Figure 3.13. The electrodes are made of copper foil tape that is 0.0035" thick. A layer of Kapton tape is added between the Plexiglas and each electrode in order to protect the Plexiglas glass surface from damage due to plasma formation on the surface. In addition, the hidden electrode is completely encapsulated by a strip of rubber to prevent the formation of parasitic plasma, which is undesirable plasma formed around the edges of the electrode and which would result in the waste of input power. One of the edges of the exposed electrode is also covered by Kapton for the same reason.

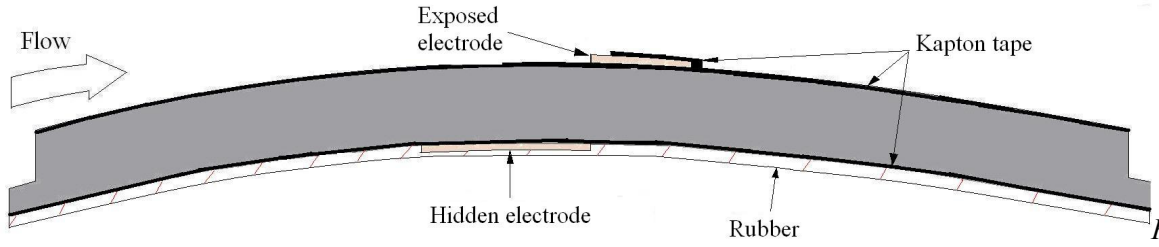

Figure 3.13 Plexiglas dielectric cross-section

The plasma actuator is calibrated for its strength as a function of the input voltage. This is done at a fixed low frequency signal since the plasma saturation force is inversely related to frequency [59]. The plasma actuator is arranged on the curved dielectric block as shown in the above figure and operated while it is propped vertically (i.e. the chordwise tangent at the actuator position is vertical) in a groove in a Styrofoam slab that is placed on a high precision electronic balance (Ohaus Explorer) with a capacity of 2100 g and a resolution of 0.01 g. This balance measures the downward acting reactive thrust produced by the plasma induced flow. The measurement set-up is shown in Figure 3.14. The calibration tests are done for multiple axial

positions of the actuator on the dielectric to gauge the influence, if any, of the position on the actuator performance.

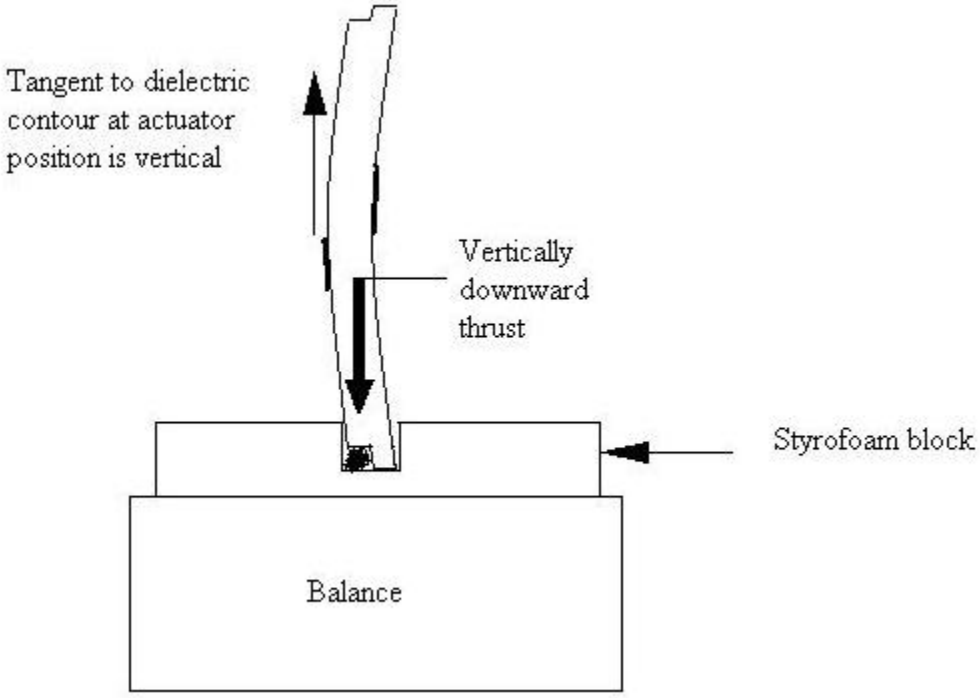

Figure 3.14 Schematic of dielectric calibration set-up

It should be remembered that the net measured thrust is not a direct indication of the actuation strength. Its magnitude is actually a conservative (reduced) estimate of the actuator strength since a part of the plasma induced flow generates viscous friction on the dielectric wall in the direction opposite to the imparted body force (actuator strength) which results in a diminished measurement of the reactive thrust. Figure 3.15 from reference [76] shows a control volume which can be used to analytically determine the imparted body force F_B from a given spatial velocity distribution, with the wall shear force F_τ deduced from the velocity gradient at the wall. The application of this analysis to results from CFD simulations of plasma actuator on a flat plate in quiescent conditions predicts that the shear force accounts for around 30% of the imparted body force. The thrust can therefore be approximated at around 70% of the actuation strength.

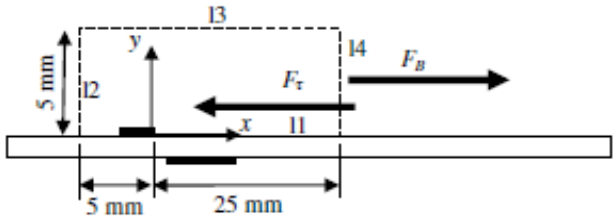

Figure 3.15 Control volume for body force computation [76]

3.2.3. Lift and Drag Measurements

This series of tests aims to validate the results obtained from numerical simulations of plasma actuation on the blade. It should be noted that the test conditions are different from those that are numerically simulated. Firstly, it is not possible to completely eliminate three-dimensional effects by adding glass plates to the tips. Moreover, it is not claimed that the presence of the aerodynamic sleeve entirely eliminates the error in the drag measurement. In light of these limitations, a laboratory replication of the numerical values of the forces is not strictly required.

However, the wind tunnel test results are expected to be qualitatively similar to their computational counterparts. They should reflect the same trends and tendencies as predicted by the CFD tool.

The wind tunnel tests follow the cases that have been numerically simulated. These cases vary based on different parameters, such as the inlet velocity, the angle of incidence, the strength of plasma actuation and the chordwise location of the actuator. The following is an enumeration of the tests that are carried out.

(1) The measurement of lift and drag characteristics on the clean 'unactuated' airfoil blade in order to ensure that these data are similar to the predictions of XFOIL.

(2) Wind tunnel runs at all numerically simulated velocities, without the blade, for the measurement of the contribution to the drag from the blade's supporting shaft and the angle of attack variation link since these two are partly unshielded by the aerodynamic sleeve near their highest points.

(3) The effect of plasma actuation strength.

(4) The effect of Reynolds number by varying the inlet velocity. This series of tests is carried out for two settings of actuation strength, ~20 mN/m and ~100 mN/m. These two values of actuation thrust are almost 70%, as discussed in 3.2.2, of the actuation strengths of 30 mN/m and 150 mN/m used in CFD simulations.

(5) Effect of the actuator's chordwise position.

3.3 Application at Realistic Conditions

From a practical standpoint, the research on plasma actuation for wind turbine power control is justified only when it is assessed for realistic operating conditions. To this end, the effect of plasma actuation is numerically computed for a two-dimensional wind turbine profile at a realistic Reynolds number to assess the lift decrease.

Secondly, the rated power operation of the WindPACT 1.5 MW turbine is studied. An algorithm, based on the blade element momentum theory, is programmed in Matlab to predict wind turbine performance. This code uses 2-D blade performance data for the computation of the turbine's power curve. It incorporates the 3-D effects with the help of available models on stall delay and blade tip effects. It is validated without 3-D models using WT_Perf, a code developed by the National Renewable Energy Laboratory without the stall delay model, and then it is employed with the model of Laino and Hansen [77] to give a more realistic estimation of the performance. This model accounts for the three-dimensional effects and modifies the two-dimensional lift and drag coefficients into three-dimensional coefficients by proposing certain increments in their values. It is then used to determine, by trial and error, the average lift reduction that would be needed for rated power operation of this wind turbine without blade pitching at high wind speeds. In this exercise, it is assumed that the 'lift vs. angle of attack' curve of the airfoil decreases by a constant factor as a result of plasma actuation which is not entirely true but it gives an approximation of the required magnitudes of lift reduction.

Subsequently the numerically calculated lift drop is compared to the lift drop requirement computed as described in the last paragraph and some modifications of the 2-dimensional actuator are proposed and investigated.

CHAPTER 4
RESULTS AND DISCUSSION

This chapter presents the results from the simulations and experiments that were outlined in Chapter 3. It also examines the applicability of plasma actuation in the context of a wind turbine. It is structured as follows:

1) Computational study
2) Plasma actuator characterization
3) Experimental and computational results

4.1 Computational Study

Uncertainty in Numerical Results

In the analysis of the numerical uncertainty carried out using the procedure in [75], the parameters investigated are C_l and C_d. The results that are eventually presented in this thesis are those from the finest grids which are practically unaffected by further refinement. In the course of all the analyses, it was found that the GCI for lift calculations never exceeded ±2% and that for drag calculations never exceeded ±3%. Since these uncertainty values would result in error bars of nearly the same size as the symbols in the graphs, they are not plotted.

Monitoring CFD Data and Post-Processing

Over the transient simulation involving plasma actuation, the reduction in the lift relative to the 'unactuated' initial condition is evident over successive time-steps. Figure 4.1 shows an example of one such time evolution curve. After a point, the time-accurate curve of lift tends towards convergence at which point it oscillates periodically with progressively smaller amplitude. It should be noted that variation comprises of oscillations of several frequencies. Of these, the periodic oscillation with the lowest frequency (or the highest time period) is chosen and the results are averaged over an integer number of these oscillations to represent the converged solution of the simulation.

Towards convergence, the amplitude of the lowest frequency oscillation decreases very slowly with time but the average becomes constant. Since the average of these oscillations is the object of interest, it is considered sufficient to terminate the computation before the amplitude becomes strictly constant with time.

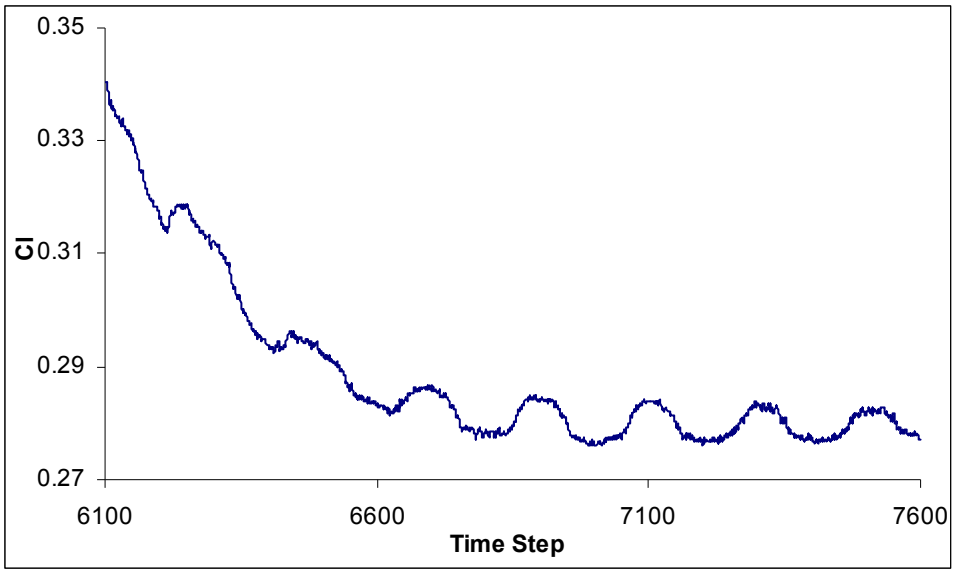

Figure 4.1 Time evolution of lift

4.2 Actuator Characterization

The strength of the curved dielectric was experimentally measured for four different chordwise positions of the actuator, viz., 25%, 35%, 45% and 55% (The dielectric itself extends from 15% to 60% of the blade chord). Although the electrodes (which are made of 0.035" thick copper foil tape), the dielectric material and thickness are same for these four settings and the actuator would be expected to behave identically for all of them, it is observed that the intermediate positions (35% and 45%) behave differently from the ones near the edges (25% and 55%). The intermediate positions of the actuator permit operation at higher actuation thrust compared to the actuator positions near the edges which were found to be more susceptible to arcing given the closeness of the two electrodes to the edge of the dielectric.

The thrust per unit span for these four positions is plotted in Figure 4.2 as a function of applied peak-to-peak a.c. voltage. Since the actuator thrust is inversely related to the signal frequency [59] and the signal generator of the plasma generation system has a frequency range of 2 kHz to 9 kHz, a low a.c. frequency of 2.5 kHz is used for actuator operation. All the measurements are reported with a relative uncertainty of ±4% at 95% confidence interval. The waveform used was negative sawtooth because this waveform type has been found to generate the maximum thrust for a given amount of consumed power [78].

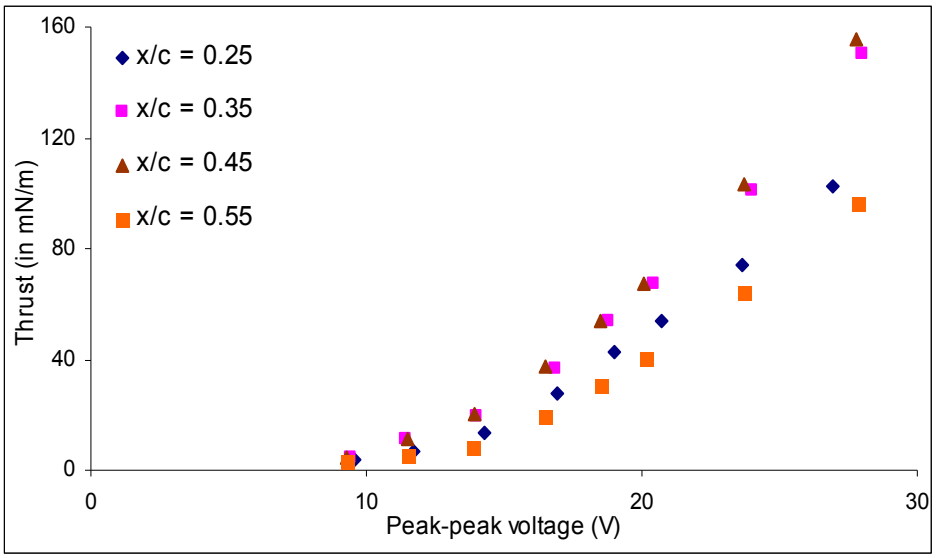

Figure 4.2 Plot of actuation strength as a function of voltage

In order to establish a correlation between the thrust and the voltage, the above graph is also plotted on a log-log scale and the data points for each actuator position are connected by a linear regression curve. It is found that the slope of these curves lies in the range of 3.2 to 3.3 which implies that the thrust varies with voltage raised to power 3.2 to 3.3 for low and moderate voltages. These values of the slope are reasonably close to the power law variation of $T \propto V^{3.5}$ as found in [59]. All regression lines are good fits and have R^2 close to 0.99. During the operation of the actuator, its strength is fixed by setting the voltage to its corresponding value from the plot in Figure 4.3.

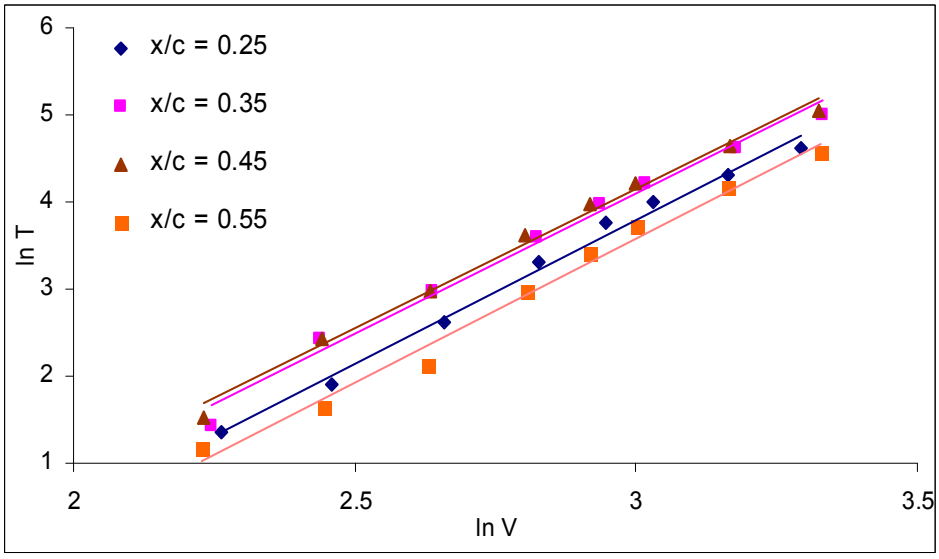

Figure 4.3 Logarithmic plot for dielectric strength calibration in terms of voltage

4.3 Results

The results from the numerical simulations and the corresponding experiments in the wind tunnel are presented in this section.

It is observed that the experimentally measured C_l and C_d are different from those computed using XFOIL (which simulates the flow in the absence of walls) and CFD. Figure 4.4 shows the variation of lift and drag coefficients from these three methods for flow velocities of 12.5 m/s and 30 m/s. The XFOIL results are in close agreement with the CFD data for both velocities. This indicates that the presence of no slip walls above and below the airfoil in ANSYS-CFX does not have a major impact on the lift and drag.

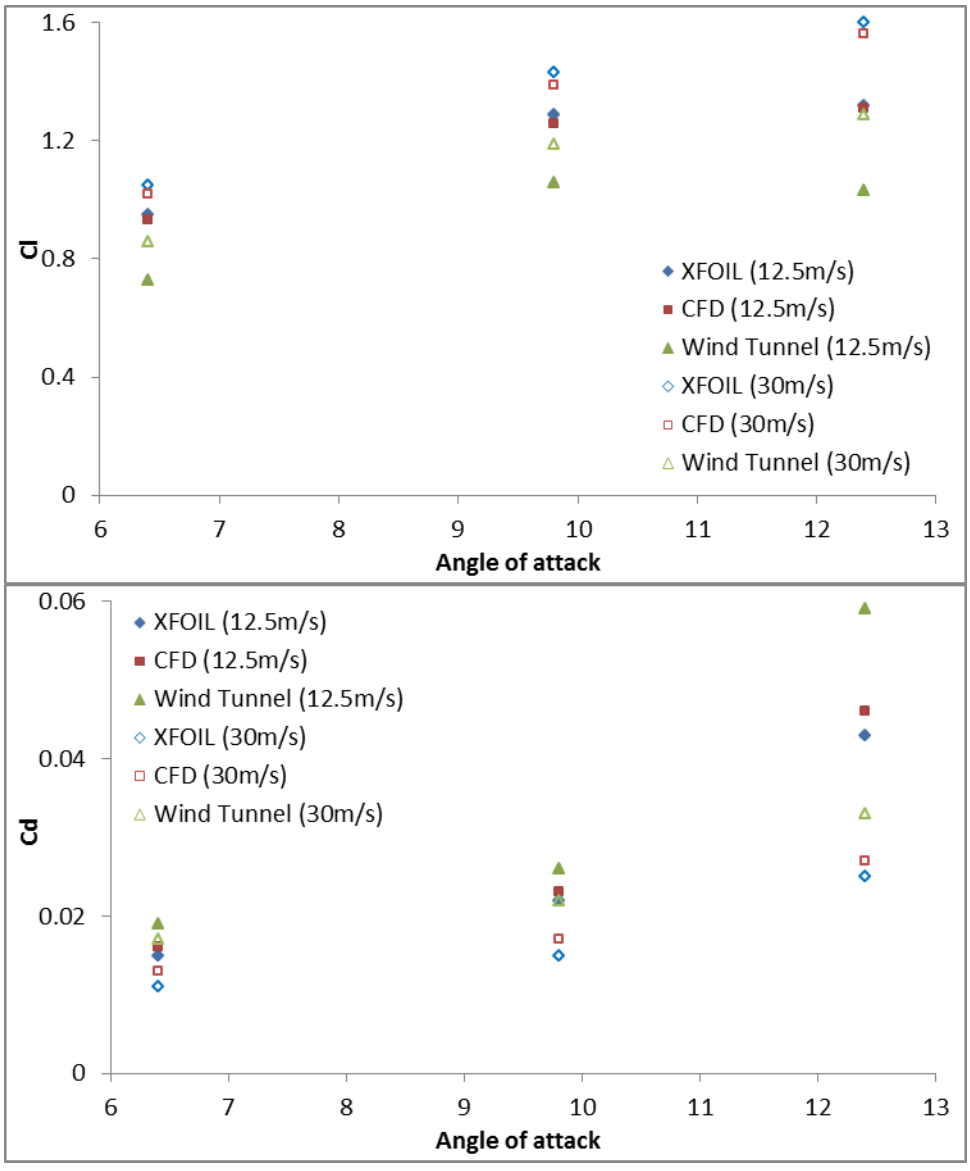

Figure 4.4 C_l & C_d from XFOIL, CFD and wind tunnel at speeds of 12.5 m/s & 30 m/s

The experimentally measured values are however considerably more different from the numerically calculated values. This difference may be mainly attributed to the three-dimensional effects associated with the wing tips which are expected to be reduced but not eliminated by the end-plates as well as to the relative difference in boundary layer transition between numerical simulation and wind tunnel experiments. In addition, for tests with plasma actuation, there is uncertainty in the equivalence of the simulated actuator strength and the actual actuator strength (estimated from thrust measurements). In view of the above factors, the experiments are meant to confirm the numerical trends qualitatively rather than quantitatively.

It should also be noted that all experimental lift and drag coefficient measurements conducted were followed by error analyses based on the uncertainty in the measurement of their components and the uncertainty in the angle of attack measurement. The error due to oscillations in the lift measurements at high angles of attack is accounted for by reading the balance to the nearest 10 gram instead of its least count of 1 gram. The uncertainty of this measured force is accordingly altered in the calculation of the error bars of the force coefficients. In all cases, the computed error bars were found to be smaller than the plot symbols and thus have not been graphically represented. In practice, however, the baseline (no actuation) measurements are found to differ slightly from one test to another even if all experimental conditions remain unchanged. This is evident in Figure 4.6 where the deviation between the highest and the lowest values is indicated and can be interpreted as the effective error band.

4.3.1. Effect of Actuation Strength

In the implementation of the momentum source in ANSYS-CFX to represent the effect of the plasma actuator, different scaling factors were applied to the force vector field to give different values of the actuation strength. The magnitude of the resultant body force was varied up to 150 mN/m in the simulations. The simulated effect of this variation on the lift, for an angle of attack of 9.8 deg and for an inlet velocity of 12.5 m/s, is presented in Figure 4.5.

In Figure 4.5, zero actuation strength represents the baseline or the 'no actuation' case. It is seen that the lift coefficient decreases with actuator strength. It decreases almost linearly at first as the actuation strength increases. This is followed by a more severe drop in the lift coefficient over a relatively small increase in the actuation strength (between 60 mN/m and 70 mN/m). Subsequently, the lift keeps decreasing at a progressively smaller rate and the variation is nearly asymptotic for high values of actuator strength.

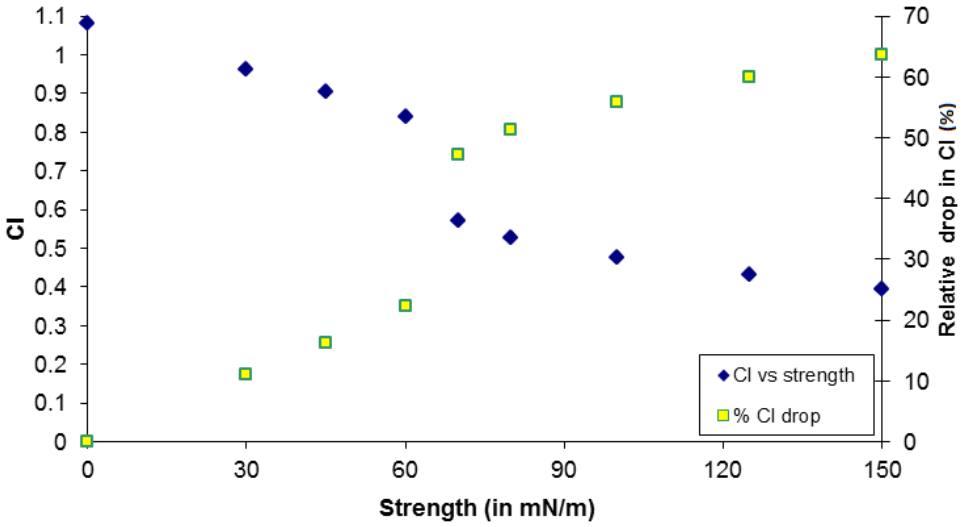

Figure 4.5 Actuation strength effect on C_l at 12.5 m/s for 9.8 deg AoA (CFD)

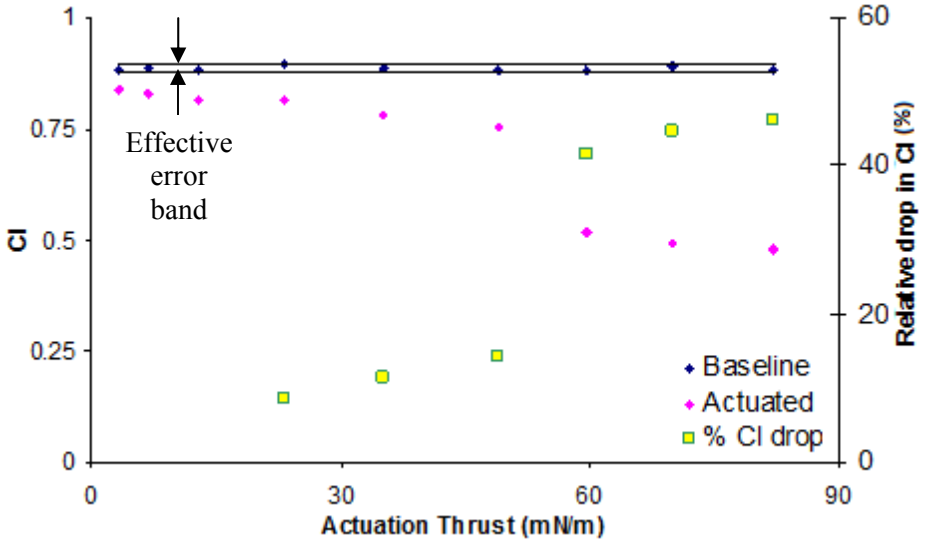

Figure 4.6 Actuation strength effect on C_l at 12.5 m/s for 9.8 deg AoA (wind tunnel)

The above tendency is also evident in Figure 4.6 which shows the results from the same exercise carried out in a wind tunnel. The sudden drop in the lift occurs between thrusts of 50mN/m and 60 mN/m. This is reasonably close to the CFD estimation given that the thrust is always less than the actuation strength.

Figure 4.7 plots the velocity field in the vicinity of the airfoil. It shows the upstream displacement of the separation point and the expansion of the separation bubble with increasing actuator strength. The white curves indicate zero-axial-velocity contours and indicate the extent of the zone of recirculation. The vertical white line at the suction surface in the plots represents

the actuator position, i.e. the position of the upstream edge of the exposed electrode and the white arrow points to the point of separation.

There is a considerable difference between the cases of 60 mN/m and 70 mN/m actuation strength. It can be seen that the region of backflow is significantly larger and the boundary layer is much weaker in the latter case. A closer look at the above flow fields shows that separation occurs downstream of the actuator position for cases (a) to (d) and upstream of it for cases (e) to (i). Moreover, there is a sudden and significant jump in the point of separation between (d) and (e). This observation indicates that the influence of the plasma actuator on the flow is amplified by a factor if the actuation strength crosses a certain threshold which corresponds to the value at which the point of separation moves upstream of the actuation position. The actuator is evidently more effective in displacing the free-stream flow further away from the airfoil wall for a flow that has already separated by the time it reaches the actuator. This greater effectiveness may be because the actuator adds momentum *in* the direction of the backflow for a boundary layer that has already separated upstream as opposed to resisting an attached flow. This indicates that the actuator is more capable of influencing the force coefficients by aiding the local flow in its vicinity rather than by countering it.

The decrease in the lift with increased actuator strength is understandable because greater strength of actuation implies greater momentum to counter the boundary layer flow. It results in the weakening of the boundary layer, displaces the point of separation towards the leading edge and widens the low pressure zone over the suction surface. This results in greater loss in lift experienced by the airfoil.

The optimum force setting of plasma actuation is, therefore, slightly in excess of the threshold discussed above. This allows us the advantage of the sudden drop in lift. It would not be desirable to operate at strength much greater than this threshold since the additional gain in terms of lift reduction tends to be inconsequential at higher values. Besides, it would result in unnecessary power consumption.

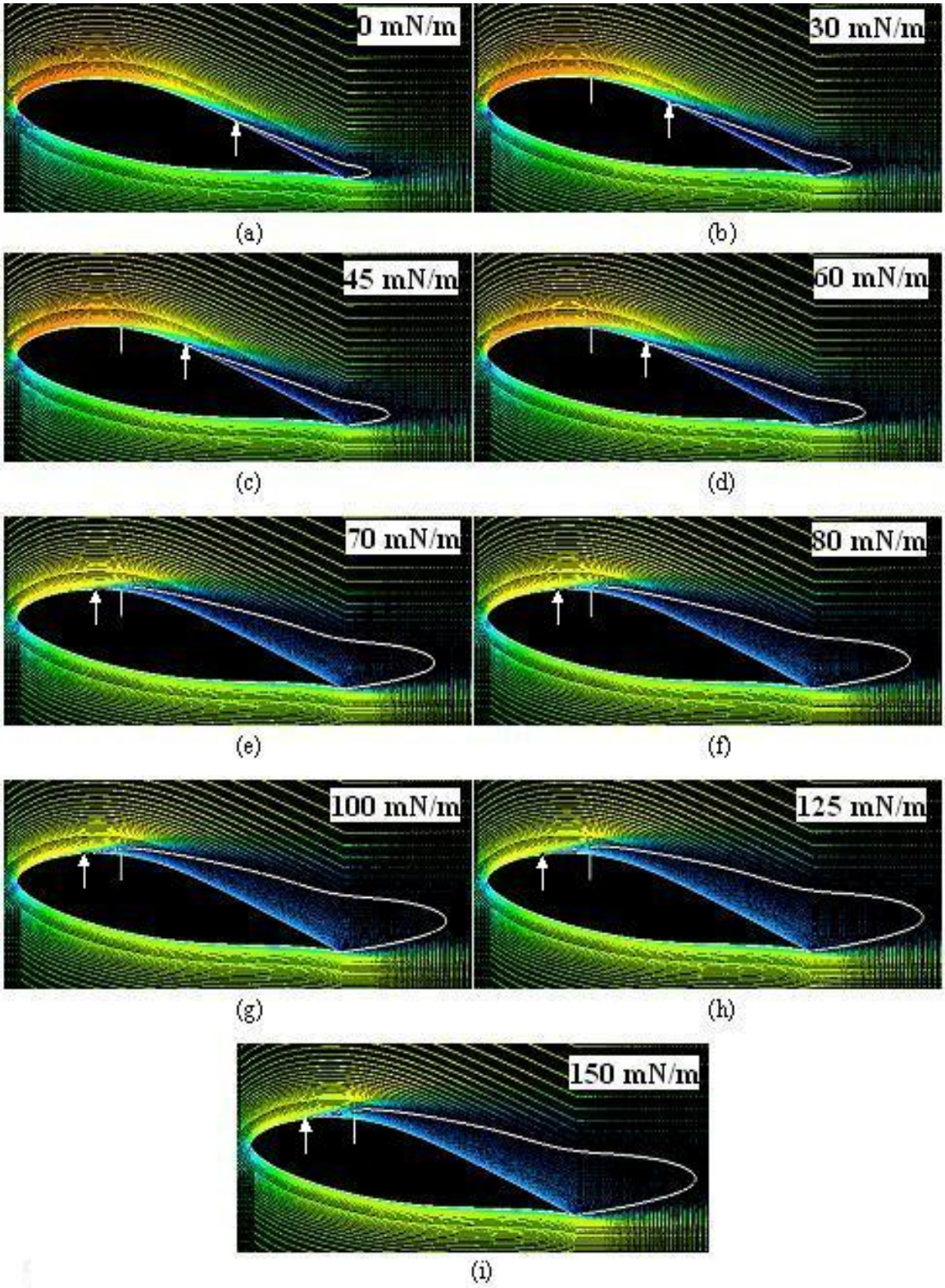

Figure 4.7 Velocity field and the *u=0* contour from CFD simulations for varying actuation strength at 12.5 m/s for 9.8 deg AoA. The color scale is the same for all the plots.

4.3.2. Effect of Reynolds Number

The effect of the plasma actuation with respect to the change in the Reynolds number corresponding to the inlet velocity is presented in this section. The angle of attack for these simulations and experiments was set at 9.8 deg and the response to change in *Re* is studied for two different actuation strengths, 30 mN/m and 150 mN/m. In this section and the subsequent ones, these two numerically simulated strength settings are regarded to be respectively equivalent to experimental actuation thrusts of 20 mN/m and 100 mN/m for reasons discussed in Chapter 3 (The shear stress accounts for nearly 30% of the actuation force in ambient air simulations on a flat plate and hence the chosen thrust settings are almost 70% of the corresponding values of strength). Figure 4.8 shows the effect on the lift and drag for 30mN/m strength.

It is seen that plasma actuation has a greater effect against lesser inlet velocities. This is expected since the actuator is acting against a boundary layer with lower momentum at a low Reynolds number. The trend reflected by the charts in Figure 4.8 is a little similar to those in the previous sub-section in the sense that the actuation effect gradually increases as the free-stream Reynolds number is decreased and subsequently a sharp increase in this effect is seen over a relatively small decrease in the *Re*. Once again, it was observed that this is associated with the displacement of the separation point to the upstream of the actuator position as seen in Figure 4.9 (The vertical white line represents the actuator position and the white arrow indicates the point of separation). At very low values of *Re*, the effect of 30 mN/m actuation is moderate and may not be necessary because the baseline lift itself is quite low.

The CFD trends of lift and drag without and with plasma actuation are fairly well matched by the experiments in spite of the difference in the absolute values. A sudden increase in the actuation effect is witnessed experimentally over a small decrease in *Re*. This sudden change occurs over nearly the same range of Reynolds numbers for both the numerical and experimental results.

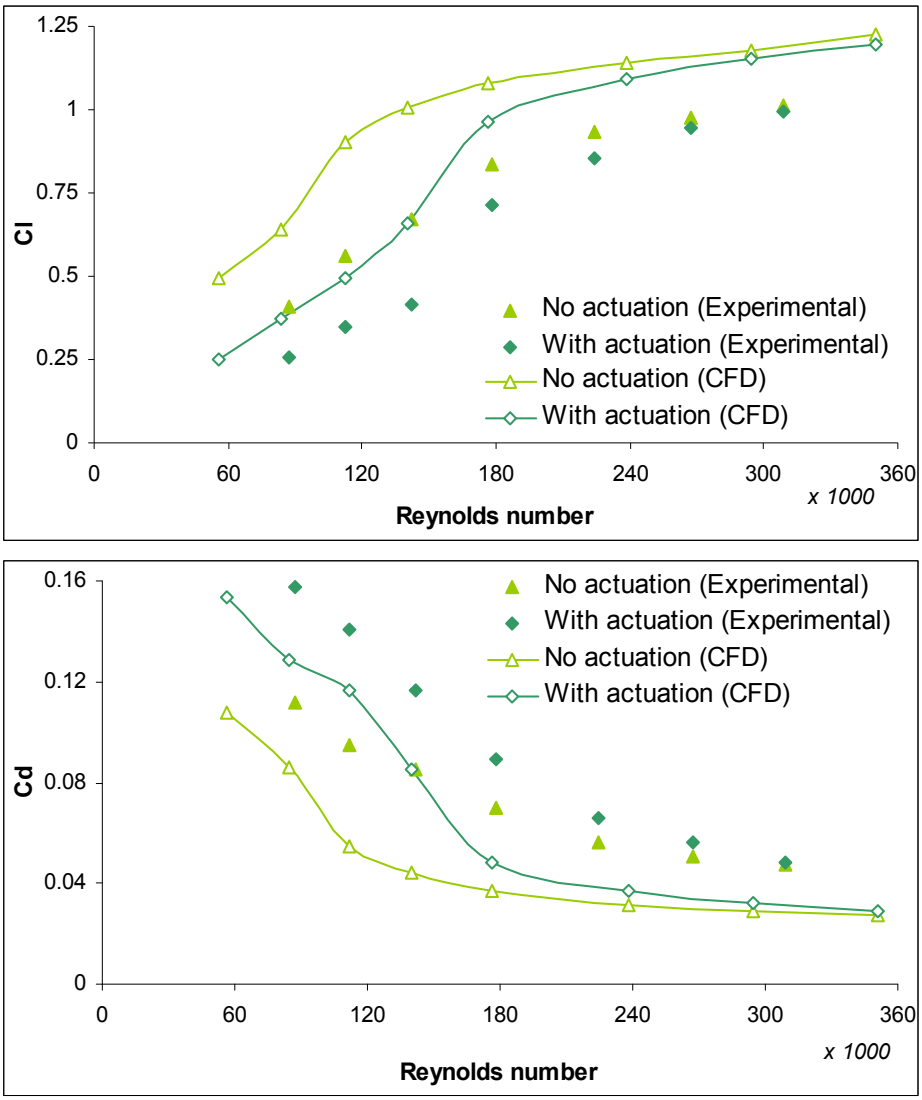

Figure 4.8 Actuation effect on C_l and C_d with *Re* variation at strength of 30 mN/m

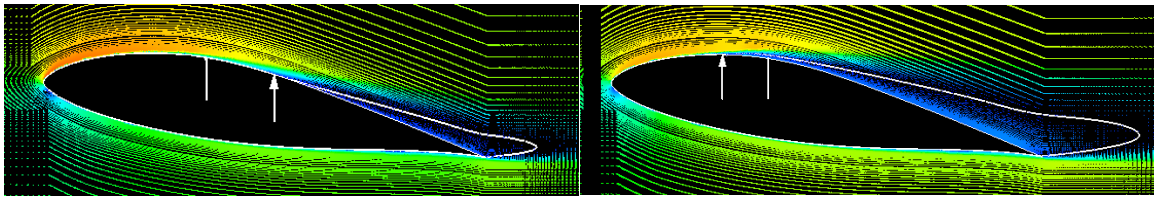

(a) (b)

Figure 4.9 Velocity fields at 9.8 deg AoA (a) at *Re* = 177000 (just before sharp drop in C_l) & (b) at *Re* = 140000 (just after sharp drop in C_l)

Figure 4.10 presents the response of the force coefficients to Reynolds number variation at higher actuation strength of 150 mN/m.

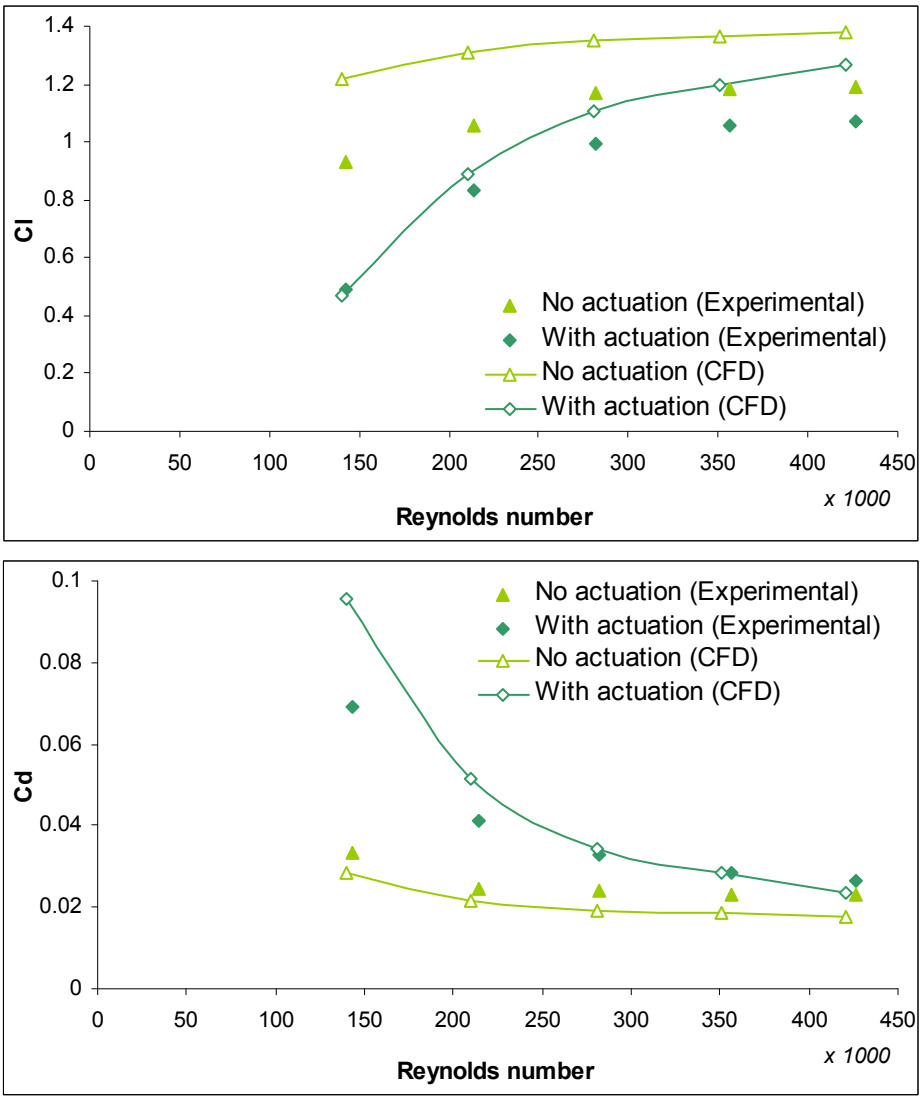

Figure 4.10 Actuation effect on C_l and C_d with *Re* variation at strength of 150 mN/m

The above graphs show the same trend as Figure 4.8. It should be noted that the data points for lift and drag for the case of $Re \approx 70000$ (free-stream of 5 m/s) are not shown. The reason for their exclusion is that extreme temporal oscillations in the forces are observed, as shown in Figure 4.11, in the CFD analysis of this case along with the shedding of von Karman vortices in the wake of the airfoil. The airfoil in this case is fully stalled. Although a given strength of actuation would be more effective at lower velocities, it is not advisable to operate at extremely high actuation strength for an extremely low velocity as the structural vibrations due to these oscillations could lead to high fatigue loading and eventually premature failure of the blade.

The experiments are once again in reasonably good agreement with the CFD simulation results. The low *Re* case, as mentioned above, is not tested so as not to risk any damage to the test blade due to strong fluctuations in the force.

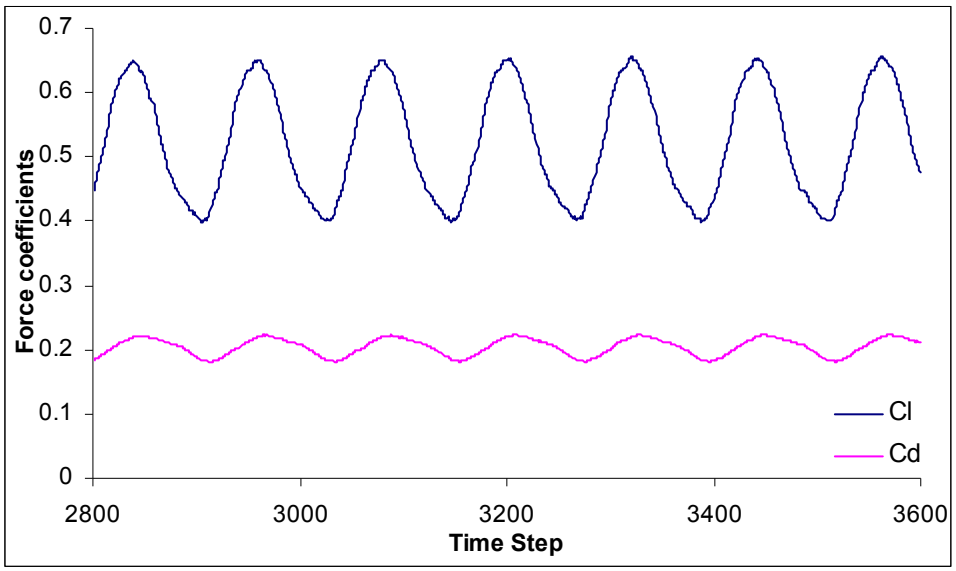

Figure 4.11 C_l and C_d oscillations for high-strength actuation at very low velocity

4.3.3. Effect of Actuator Position

In this section, the chordwise actuator position is varied keeping the actuator strength and the free-stream velocity constant. The results are presented for three different angles of attack, namely 6.4 deg, 9.8 deg and 12.4 deg, and two different settings of force and inlet velocity, namely 30 mN/m at 12.5 m/s and 150 mN/m at 30 m/s. The choice of the first setting is akin to that used in [26] and helps to revalidate the percentage lift reduction that was obtained for the three angles of attack. The second setting is closer to the real operating condition. Although 30 m/s is still less than the typical velocities at the blade tip, it provides a better idea of how a high velocity flow would react to high-strength actuators.

In all the graphs in this section, the actuation is numerically simulated on the suction surface in sub-domains of 15% of the chord length (~30mm, which is a typical actuator width). Five different actuator positions, 25%, 40%, 55%, 70% and 85%, are examined for these computations. The CFD generated data points in the following graphs are shown at the actuator location. Also, the baseline or the 'no actuation' force coefficients show a very slight variation between the different positions because the simulation for each position uses a slightly different mesh with higher mesh density in and near the actuator sub-domain. The wind tunnel measurements are reported at actuator locations of 25%, 35%, 45% and 55% of the chord length. It should be noted that numerical simulations permit the investigation of a wider range of chord

locations as opposed to experiments where there are constraints on the placement of the dielectric.

Actuator Location Effect on C_l and C_d at 12.5 m/s and 30 mN/m

Figures 4.12, 4.13 and 4.14 show how the lift and drag coefficients vary with the position of the actuation sub-domain for angles of attack of 6.4 deg, 9.8 deg and 12.4 deg respectively for low-strength actuation at a low incoming velocity of 12.5 m/s.

At low angle of attack (6.4 deg), the CFD results in Figure 4.12 indicate that there does not seem to be a clear preference from amongst the different cases in terms of the effect on drag at the angle of 6.4 deg (ΔC_d is comparable for all the positions). On the other hand, the decrease in the lift coefficient is found to be greatest when actuation is closest to the trailing edge (10.2%, as compared to 6.2% for the most upstream actuation location). The most optimum position for operation, therefore, appears to be near the trailing edge for an unstalled blade. This tendency is again noticeable from the wind tunnel lift measurements where the lift reduction benefit is maximum for the most downstream location (x/c = 0.55).

When the angle of attack is increased to 9.8 deg, the computational results in Figure 4.13 show that a remarkably clear preference exists for plasma actuation at an intermediate chordwise position for this angle of attack. The lift reduction for this position is more than 20%, as opposed to nearly 9% for the most upstream and most downstream sub-domains. The increase in drag is also substantial. This indicates that proper placement of the actuator can be a very important factor in its effectiveness when it has started to stall. The existence of a preferred intermediate position is corroborated by the experimental data.

The numerical results of Figure 4.14, which shows the force coefficients for plasma actuation on a stalled blade at 12.4 deg, indicate a clear maximum in the lift decrease similar to Figure 4.13. It is interesting to note that the maximum lift drop achieved in this case is 28.6% accompanied by a considerable rise in the drag as well. It should also be noted that the most optimum location at this angle of attack is further upstream of that in the case of 9.8 degrees. This observation is supported by the experimental force coefficient measurements.

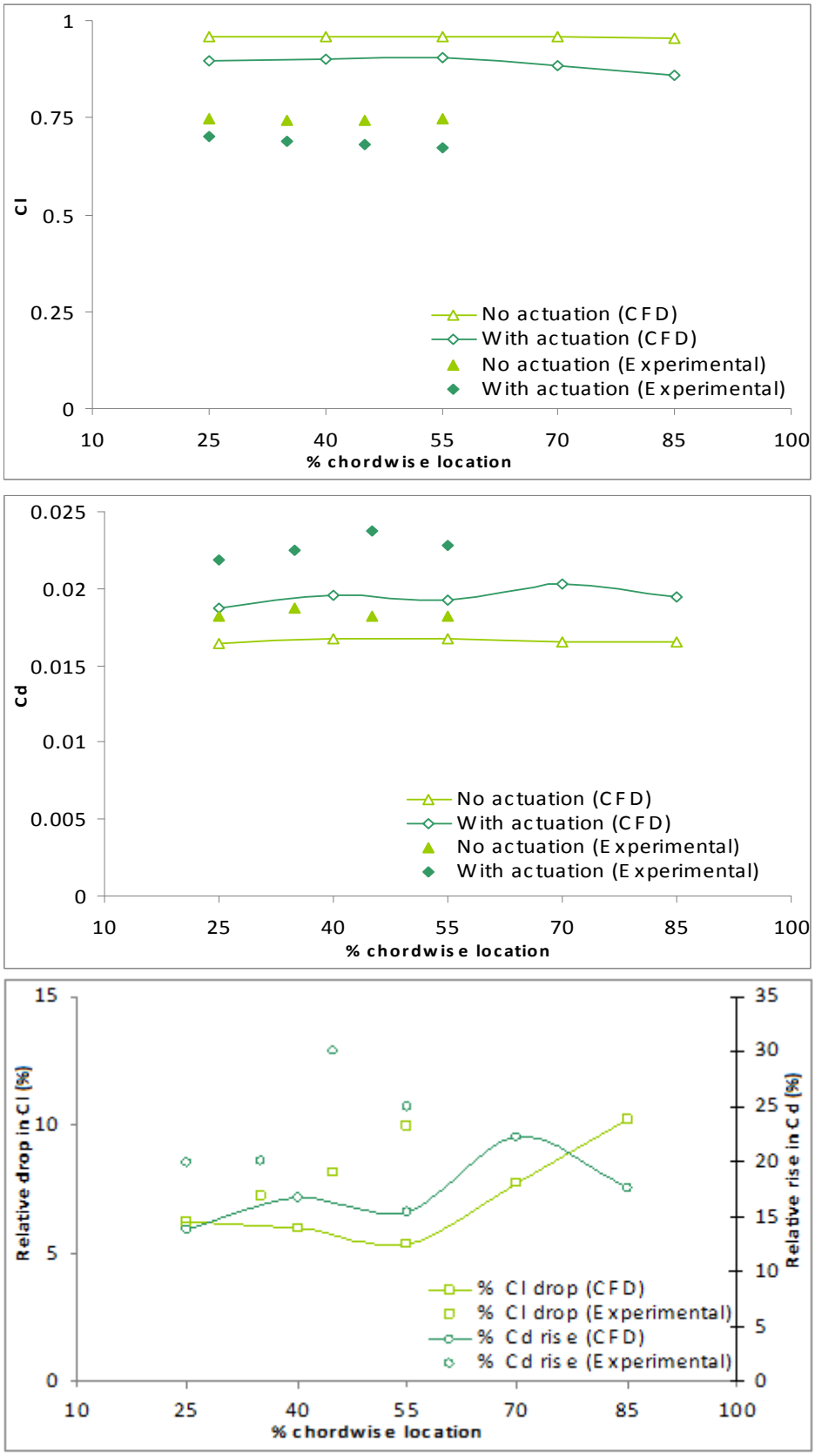

Figure 4.12 Location effect on C_l and C_d at 6.4 deg and 12.5 m/s at 30 mN/m strength

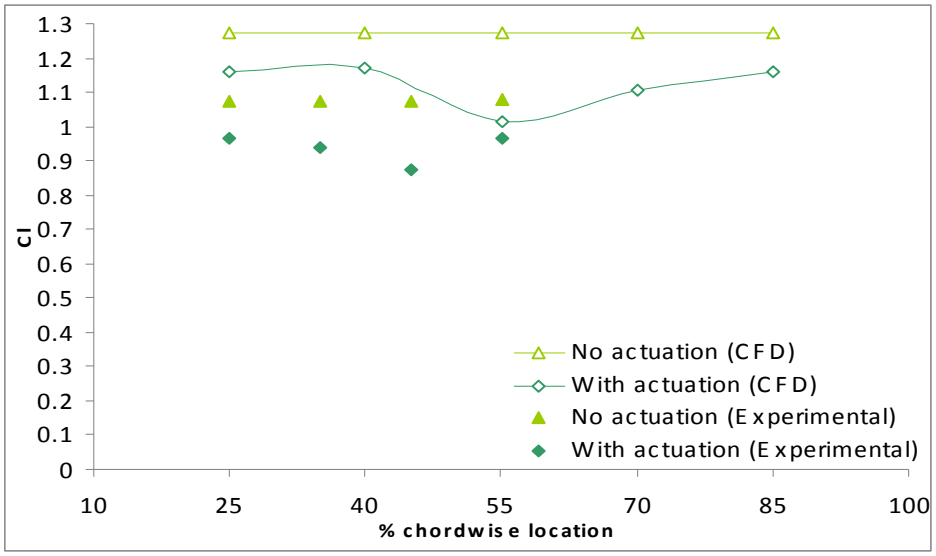

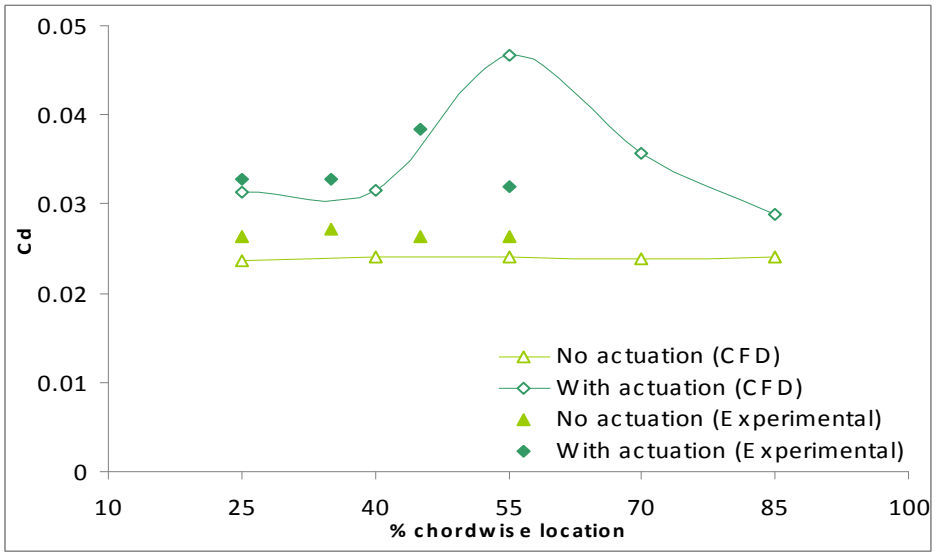

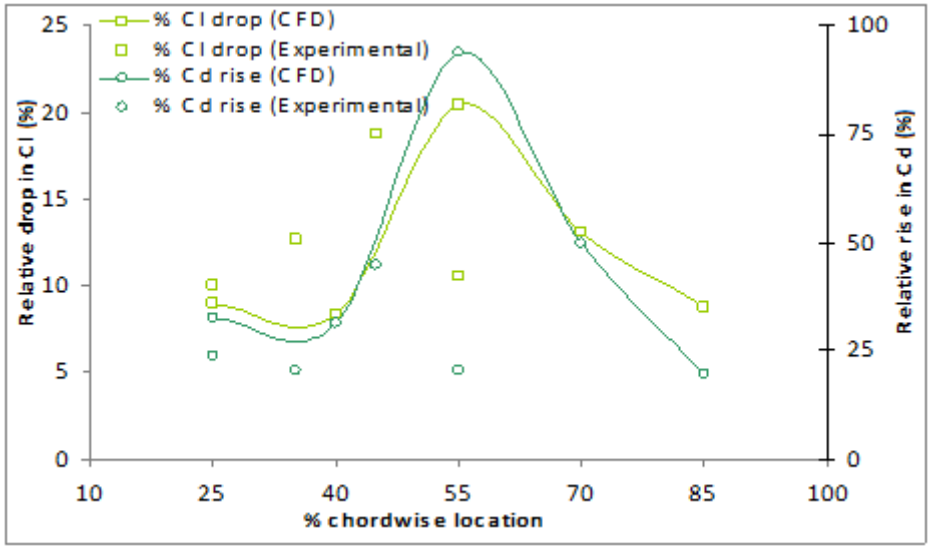

Figure 4.13 Location effect on C_l and C_d at 9.8 deg and 12.5 m/s at 30 mN/m strength

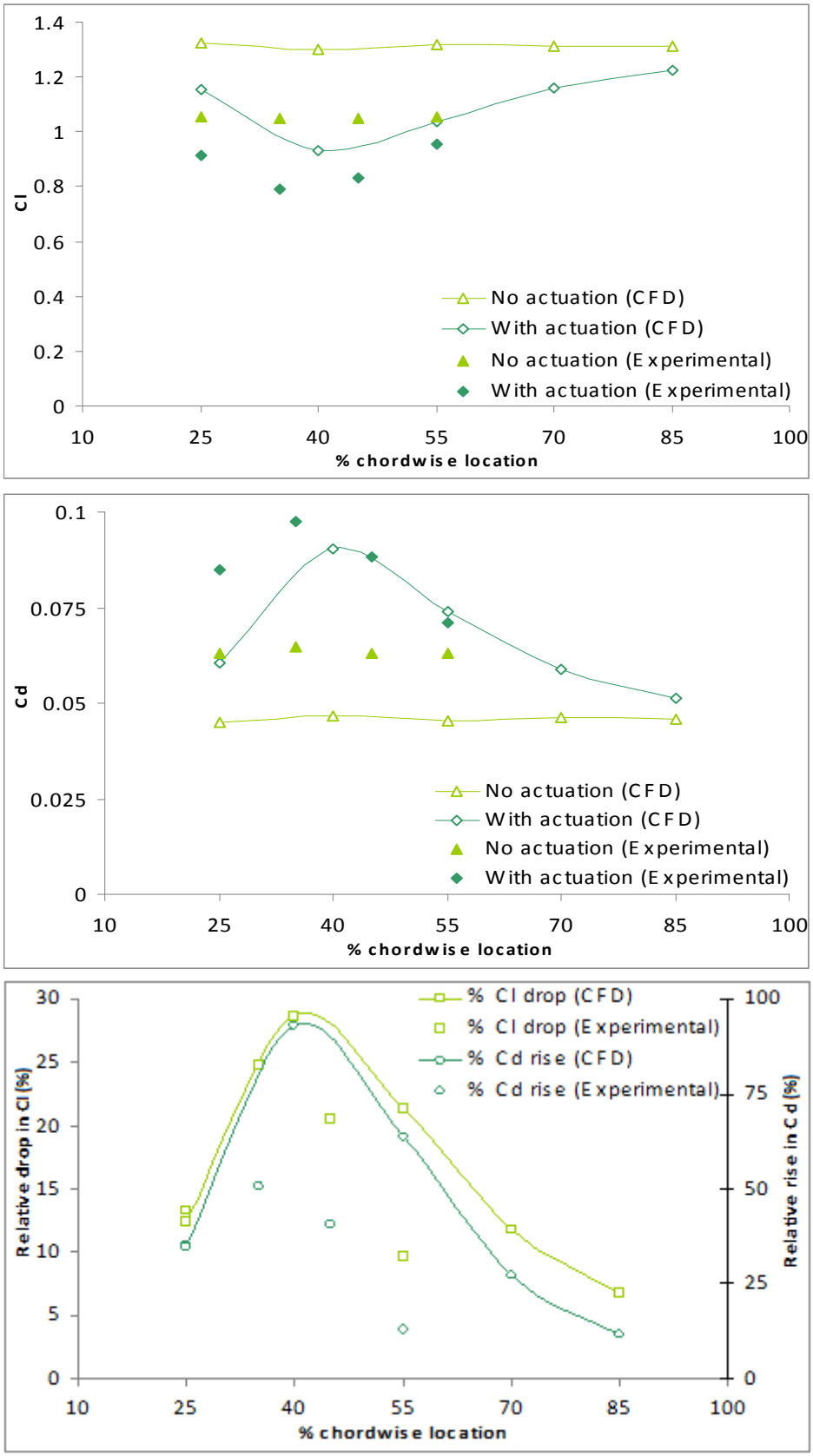

Figure 4.14 Location effect on C_l and C_d at 12.4 deg & 12.5 m/s at 30 mN/m strength

From the results in Figures 4.12, 4.13 and 4.14, it can be inferred that the position of the actuator has a significant impact on its effectiveness, especially when the blade is beginning to stall or has stalled and that there is a preferred location for actuation at all angles of attack. At low angles, this position is close to the trailing edge and shifts upstream with an increase in the angle of attack.

Plasma actuation, when applied on an airfoil opposite to the free-stream flow, results in an increase in the boundary layer thickness or causes the boundary layer to separate. The simulation of the unactuated flow at 6.4 deg indicates that the boundary layer always remains attached. When actuation is simulated for the most upstream case (x/c = 0.25), no flow separation is observed as seen in Figure 4.15 (a). As the actuation is applied further downstream, it proves to be more effective in reducing lift because the actuator has to counter a flow that has decelerated further and can be more easily diverted away from the airfoil. The diversion of the boundary layer becomes more evident, as seen in Figure 4.15 (b), at the most downstream location (x/c = 0.85) as the flow separates a short distance upstream of the trailing edge.

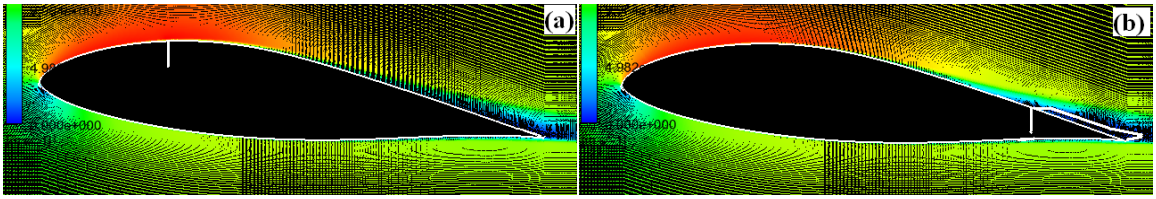

Figure 4.15 Velocity field at 6.4 deg AoA and 12.5 m/s for actuator at (a) x/c = 0.25 (no separation), (b) x/c = 0.85 (small separation region). Vertical white lines are for actuator position.

In the case of the flows at 9.8 deg and 12.4 deg, the simulation shows that the unactuated flow separates on the suction side. Up to a certain point, downstream actuators are found to be more effective than the upstream ones in the enhancement of boundary layer separation due to the same reasons as mentioned for the flow at 6.4 deg. As the actuator is placed further downstream, the point of separation moves upstream as noted when actuator moves from x/c = 0.25 in Figure 4.16 (a) to x/c = 0.55 in Figure 4.16 (b). But this holds true till a limit. When separation becomes so prominent that it occurs upstream of actuator position, it does not expand any more with downstream displacement of the actuator. This is the critical position at which the influence of actuation is greatest. For positions downstream of this critical position, the interaction of the actuator with the boundary layer flow results in a point of separation which is only slightly upstream of the actuator. This can be seen in Figure 4.16 (c) where the actuator position is x/c = 0.85. Hence any further downstream displacement of the actuator causes the point of separation to recede downstream and results in lower lift. Vertical white lines show the actuator position and white arrows show the separation point.

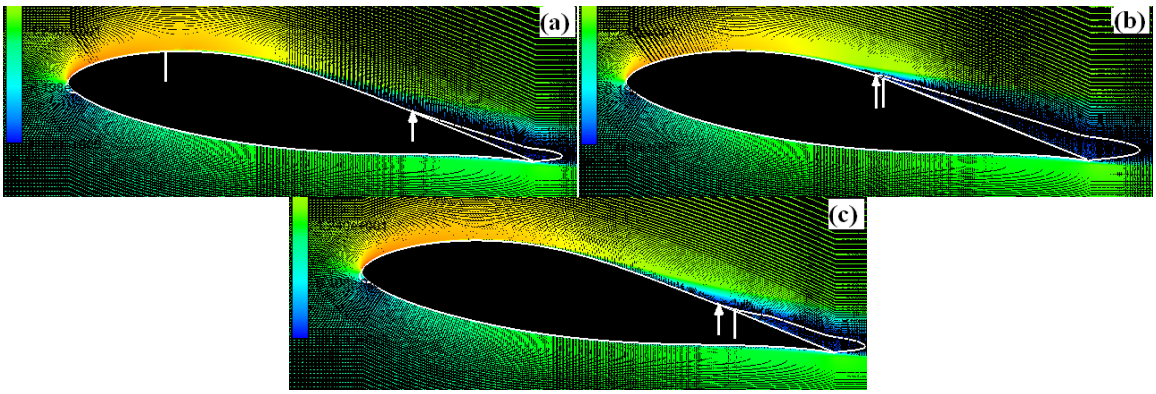

Figure 4.16 Extent of separation for (a) upstream (x/c = 0.25), (b) intermediate (x/c = 0.55) and (c) downstream (x/c = 0.85) actuator positions

In a realistic scenario, the tendency of having different optimum locations at different angles of attack can be exploited by having a series of actuators, all connected electrically in parallel with switches, in succession on the blade's suction surface. When power control is required for low wind speeds (~13-15 m/s, associated with low to moderate angles of attack), the downstream actuators could be turned on and for higher wind speeds (associated with higher angles of attack) the more upstream actuators could be switched on.

Actuator Location Effect on C_l and C_d at 30 m/s and 150 mN/m

Figures 4.17, 4.18 and 4.19 show the variation of the lift and drag coefficients with the position of the actuation sub-domain for angles of attack of 6.4 deg, 9.8 deg and 12.4 deg respectively for an actuation strength of 150 mN/m at a relatively high incoming velocity of 30 m/s.

Once again, it is observed in Figure 4.17 that the greatest lift reduction occurs for the most downstream sub-domain. This reduction is numerically computed as 8.7%. The increase in drag is more or less similar for all the positions. The trend of increasing lift drop with increasing axial actuator position is also observed experimentally.

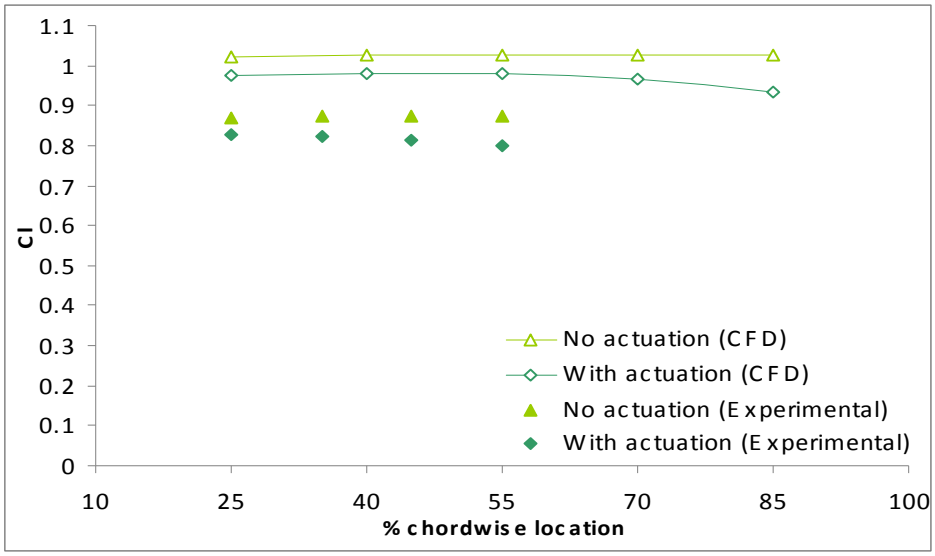

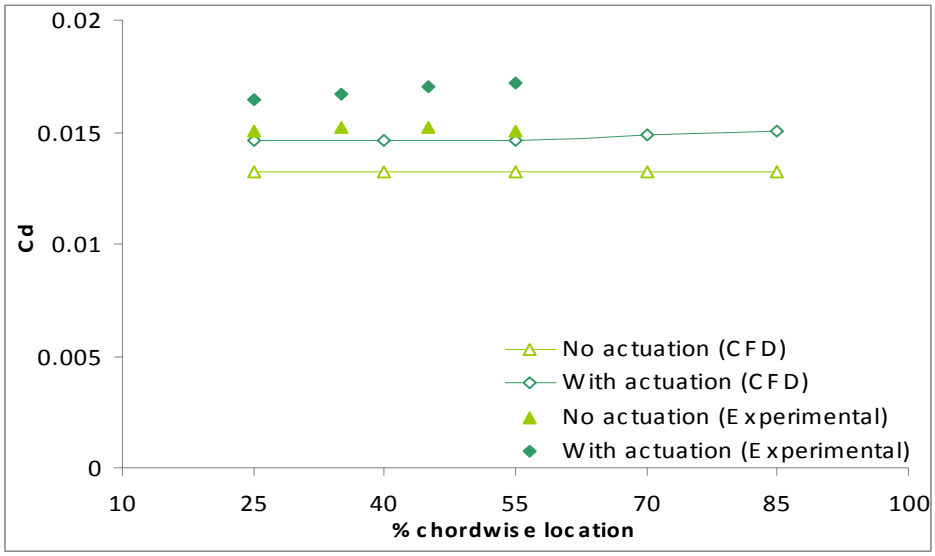

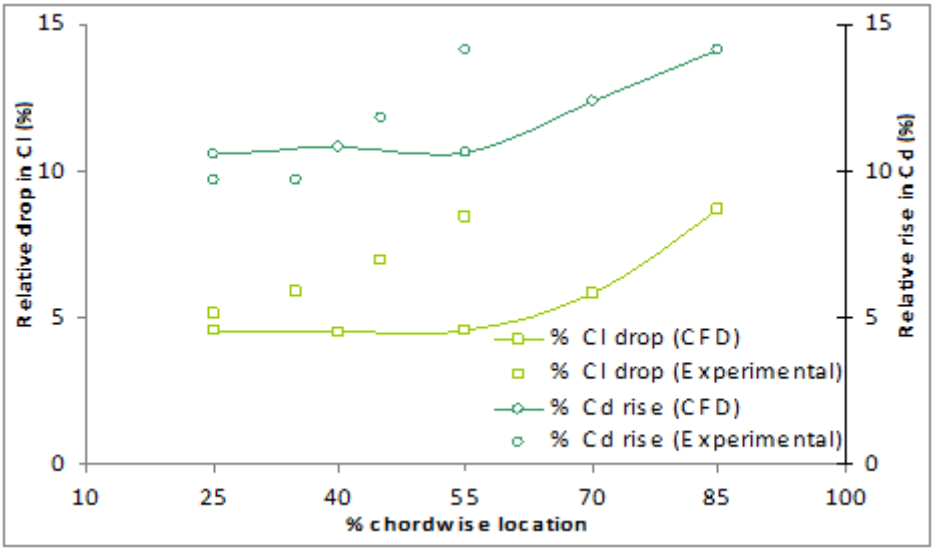

Figure 4.17 Location effect on C_l and C_d at 6.4 deg and 30 m/s at 150 mN/m strength

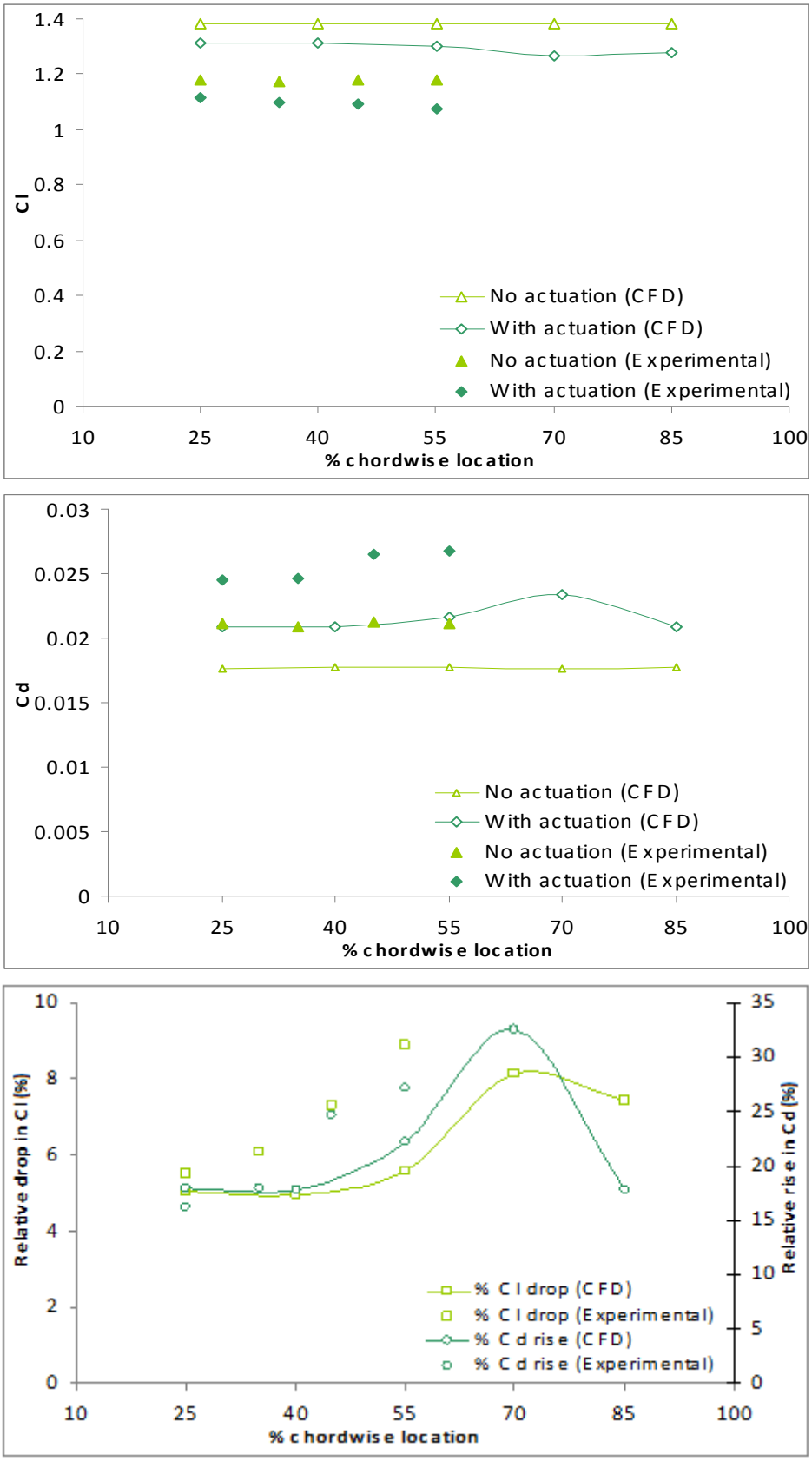

Figure 4.18 Location effect on C_l and C_d at 9.8 deg and 30 m/s at 150 mN/m strength

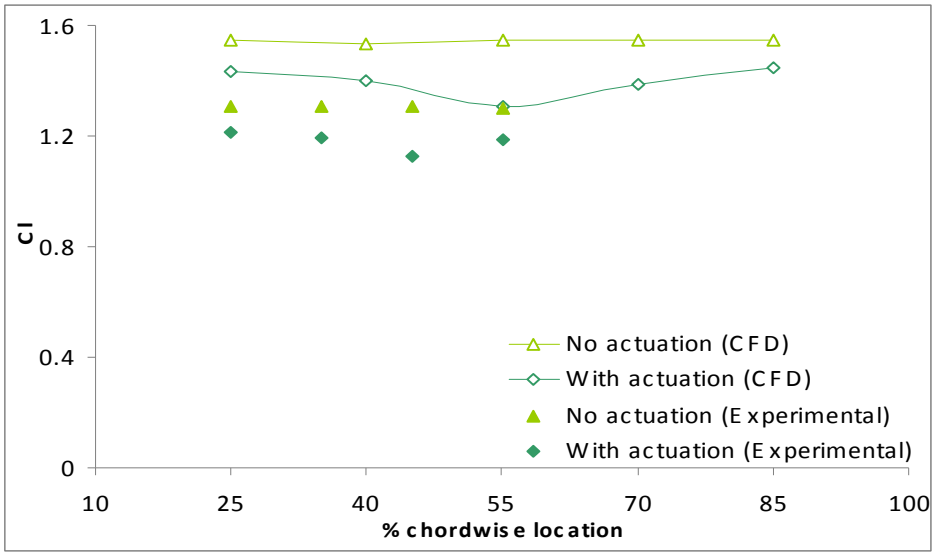

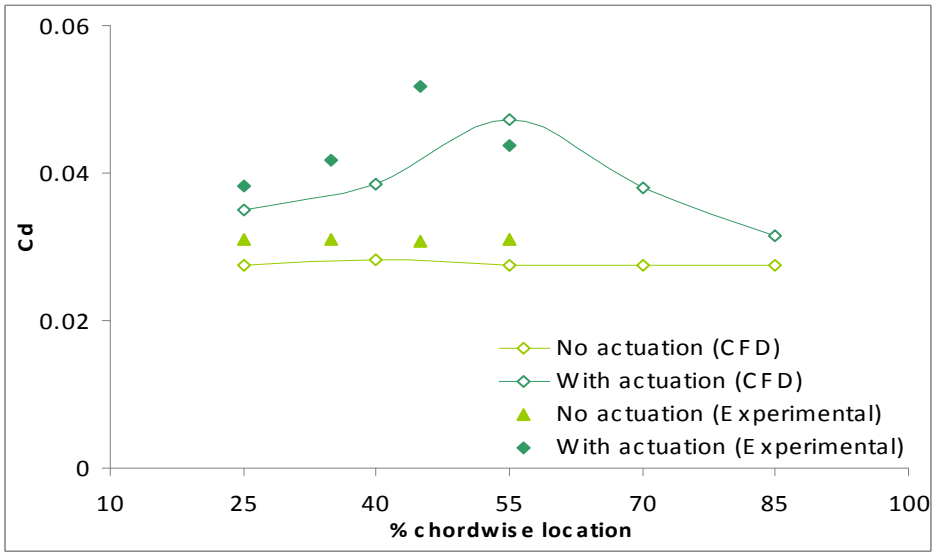

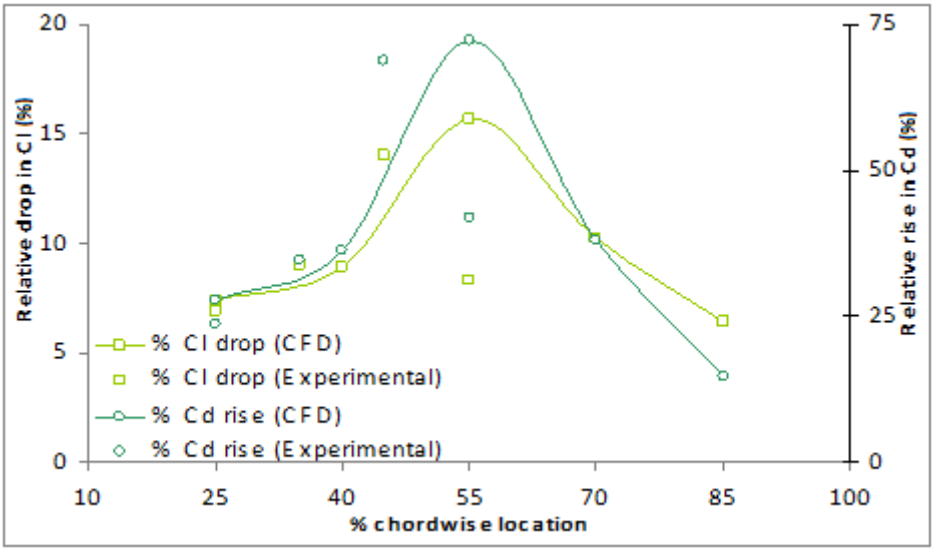

Figure 4.19 Location effect on C_l and C_d at 12.4 deg and 30 m/s at 150 mN/m strength

For a higher angle of attack of 9.8 deg, the computational results in Figure 4.18 show that the optimum position is now the second one from the trailing edge. The lift reduction is 8.1% in this case. The optimum in the drag increase is more clearly noticeable in this case. However, the experimental data suggests that lift drop keeps increasing as one goes downstream (till 55% chord). It is very likely that an optimum exists further downstream although this could not be verified due space limitations posed by the dielectric.

At a 12.5 deg angle of attack, the largest lift reduction is witnessed for the third actuator position. The magnitude of this reduction is greater than 15%. The rise in drag is also significant. As mentioned above, the existence of an optimum in this case is also validated by the experimental measurements and the fact that it is located on the dielectric plate substantiates the presumption stated in the last paragraph.

The last three figures show less reduction in lift as compared to the three before them. This is understandable because the 30 m/s flows carry greater momentum in their boundary layers than the 12.5 m/s flows do. Although the actuation strength is greater for 30 m/s, it is not nearly enough to produce lift decrease of the same magnitude. Besides, these two sets of figures are similar in the sense that the most suitable actuation location shifts upstream with an increase in the angle of attack. However, it is observed that the upstream displacement of this position is less remarkable in the case of a higher inlet velocity.

4.4 Plasma Actuation at Full-Scale Conditions

Given that ANSYS-CFX simulation results were broadly in agreement with wind tunnel measurements for low *Re*, an attempt was made to evaluate the influence of plasma actuation on the lift and drag of the airfoil at realistic conditions using CFX.

In a numerical simulation carried out at a realistic Reynolds number of $\mathrm{Re} = 7.5 \times 10^6$, based on a typical relative wind velocity of 87.5 m/s, using a full-scale tip profile of the DU 96-W-180 blade section with a 1 m long chord at an angle of attack of 6.4 deg, the impact of a single 150 mN/m actuator placed at 30% of chord length on the lift and drag was found to be practically negligible. As a result, its effect on the wind turbine power curve would also be insignificant.

The rotor power output curve for the WINDPACT 1.5 MW turbine is computed by coding in Matlab an algorithm based on blade element momentum theory, as described in Section 3.3. This program, without a stall delay model, is in very good agreement with WT_Perf (an NREL code without stall delay) but underestimates the power output because stall sets in early (See Appendix A for the validation of the code). Having been validated, the Matlab code is

used to predict the wind turbine performance accounting for the stall delay effects with the model of Laino and Hansen [77] as seen in Figure 4.20. This power curve represents the operation of the wind turbine at constant tip-speed ratio up to wind velocities of 11.5 m/s and constant rotor speed for higher wind velocities. Since the influence of the plasma actuator is found to be inconsequential, a plasma actuated turbine will follow the same power curve. The figure also shows the target curve of rated power operation.

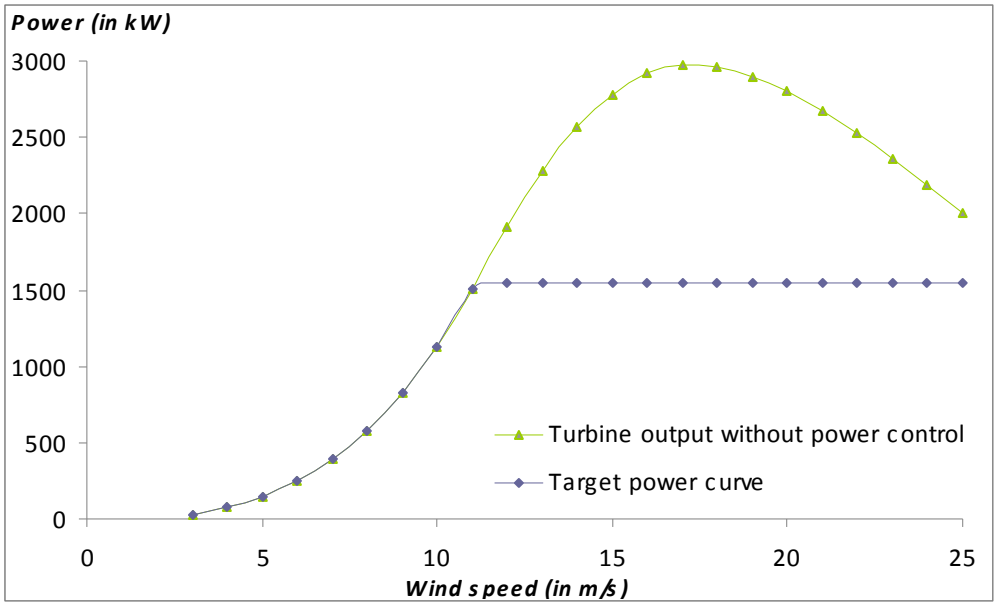

Figure 4.20 Performance curve of WINDPACT 1.5 MW wind turbine

For rated power operation at 1.5 MW, the turbine would have to shed the excess power by reducing the lift and increasing the drag on its blades. In this approximative analysis, the magnitude of lift reduction necessary for rated power operation is estimated by trial and error and the effect of drag increase is neglected for the moment. This assumption is more valid at the blade tip where the contribution of the lift to the rotational force is more important. Since the outboard of the blade is more significant in terms of torque and generated power, it is reasonable to ignore the drag. In the estimation of the required fractional lift reduction, it is assumed that all the blade sections along the span are subject to the same lift reduction. Figure 4.21 gives an estimate of the order of lift reduction requirement for operation at rated power (refer to Figure 4.20).

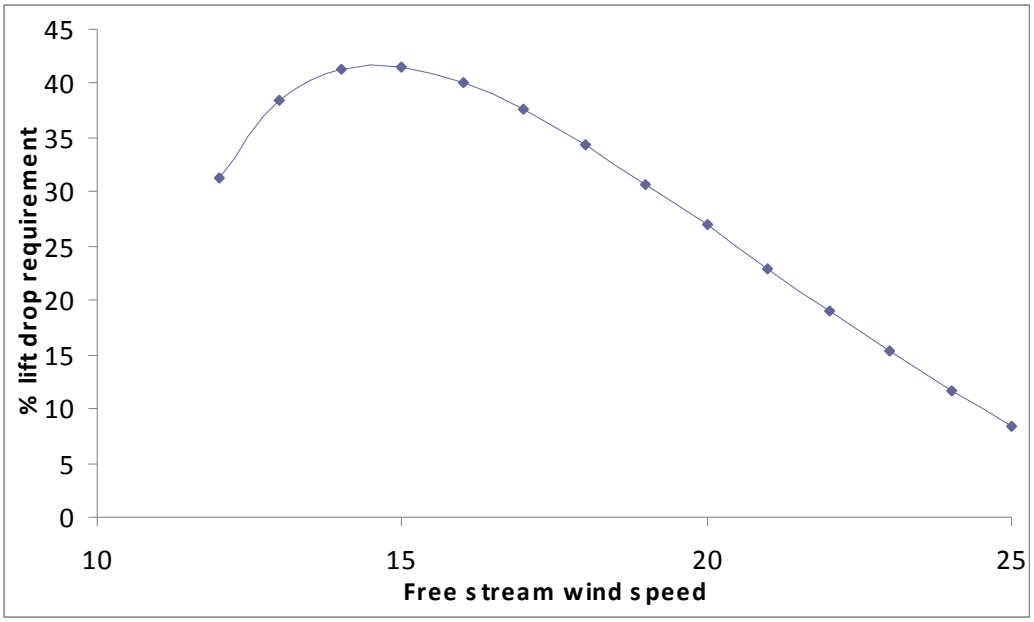

Figure 4.21 Lift reduction requirement vs. free-stream speed

Alternative configurations studied

1) Plasma actuation was simulated in the operating conditions described earlier in this section by applying the time-averaged body force in seven sub-domains at chordwise positions of 30%, 40%, 50%, 60%, 70%, 80% and 90% on the suction surface. The separation between each of these sub-domains is 1.5 times the sub-domain width since plasma actuators in series have to be well spaced out to avoid mutual interference. High actuation strength of 150 mN/m was applied in each of these sub-domains.

It was found that the decrease in lift reduction as a consequence of seven plasma actuators in series was less than 1%. The drag increase was also negligible. These variations, resulting from the best option that is currently available (i.e. multiple actuators in series operating at their maximum strength), in the aerodynamic forces are extremely inconsequential to have any discernible impact on the generated power. They are far less than the requirements shown in Figure 4.21.

In view of the above limitations of multiple plasma actuators on a full-scale blade at a realistic Reynolds number, the impact of multiple actuators is analyzed on the small-scale blade at a relatively smaller *Re* and the results are presented in Appendix B. It is observed that having several actuators in series is more advantageous than having a single actuator that is optimally located on the suction side.

2) In light of the inability of the current generation of plasma actuators to effectively influence real wind turbine performance, a CFD evaluation is performed using different settings

of actuator strength that might become available in future. The actuator model is concentrated at a single location in this case.

The actuation strength is doubled at each step to assess the corresponding lift reduction. It is observed that an actuator strength that is higher than the current standard by at least two orders of magnitude would be necessary for a lift drop that is comparable to the maximum requirement shown in Figure 4.21. This implies that plasma actuation will need to be coupled with another method such as rotor speed control to become a viable option for wind turbine power control in the near future.

CHAPTER 5
CONCLUSIONS

The ability of plasma actuation to influence the lift of a wind turbine profile is assessed as a part of this research. Attempts are made to optimize the operation of a plasma actuator in the context of a wind turbine. The computational analysis carried out in ANSYS-CFX is validated by wind tunnel experiments. The numerical and the experimental trends are found to be consistent with each other. The validation of ANSYS-CFX leads to the conclusion that it can serve as a reliable means for future numerical studies aimed at investigating the influence of plasma actuation in the case of external flows over airfoils.

With regard to the parametric study on the influence of actuation strength, it is observed that greater strength of actuation results in greater lift decrease. Beyond a certain strength threshold, the drop in lift is far more substantial. This sudden jump in ΔC_l is attributed to the actuator's ability to exert a greater influence on a separated boundary layer when it is adding momentum in the same direction as the local flow. After having crossed this threshold, it is not very useful to go on increasing the strength as the lift reduction benefit tends towards constancy.

The results of the parametric study on velocity follow the same logic as above. There exists a critical speed below which there is a sharp jump in ΔC_l. Similar as above, the actuator is found to be more potent when it is operating at a low enough speed where the boundary layer has separated upstream of it.

Apropos the parametric study on the actuator position, there always exists a preferred location on the airfoil suction side. The optimum is near the trailing edge of the blade at low to moderate angles of attack. As the angle of attack is increased, the optimum position shifts upstream. This behavior is observed at two combinations of velocity and actuation strength. The maximum lift reduction obtained in this study was 29%. This was observed for the optimum position of the actuator at an angle of attack of 12.4 deg. The optimum at a higher velocity happens to be downstream than that at a lower velocity for the same angle of attack. The optimum chordwise position can be defined as the most upstream position of the actuator for which the point of separation is upstream of it. This can serve as a design rule for the placement of plasma actuator on the suction side of the blade. In addition, the variation of the optimum with respect to the angle of attack can be exploited by having successively placed actuators along the chord and electrically connected in parallel. The desired actuator could be switched on depending on the angle of attack that corresponds to the speed of the wind.

An initial estimate of the lift reduction requirement for rated power operation of a wind turbine shows that up to 40% of ΔC_l reduction may be necessary when the turbine power output peaks before stalling. A numerical simulation in CFX which uses a full-scale wind turbine profile at a realistic velocity leads to the conclusion that the state of the art in plasma actuation is not sufficient to have a noticeable impact on the power generated. An assessment of hypothetical actuator strengths that are not currently achievable shows that actuation strengths higher by at least two orders of magnitude would be required to control the power of a MW-class wind turbine.

There has recently been an order of magnitude improvement in the capacity of plasma actuators in the last few years. More such improvements will be necessary before an attempt is made to control wind turbine power with the help of plasma actuation. If and when plasma actuators of adequate strength become available, a more realistic assessment of their applicability on wind turbines can be made in three dimensions in rotating frames of references.

REFERENCES

[1] World Wind Energy Association, "World Wind Energy Report 2009," Report, March 2010.

[2] J.F. Manwell, J. G. McGowan and A.L. Rogers, "Aerodynamics of Wind turbines," in *Wind Energy Explained*, Chichester, England: John Wiley & Sons, 2002, pp. 83-139.

[3] C.L. Enloe, T.E. McLaughlin, R.D. Van Dyken, K.D. Kachner, E.J. Jumper and T. Corke, "Mechanisms and Responses of a Single Dielectric Barrier Plasma Actuator: Plasma Morphology", *AIAA Journal*, vol. 42, no. 3, pp. 589-594, 2004.

[4] J. R. Roth, D. M. Sherman and S. P. Wilkinson, "Electrohydrodynamic Flow Control with a Glow-Discharge Surface Plasma," *AIAA Journal,* vol. 38, no. 7, pp. 1166-1172, 2000.

[5] T. Corke and M. Post, "Overview of Plasma Flow Control: Concepts, Optimization, and Applications," in *43rd AIAA Aerospace Sciences Meeting and Exhibit, Reno, Nevada*, 2005, Paper AIAA-2005-563.

[6] B. Goeksel, I. Rechenberg, D. Greenblatt and C.O. Paschereit, "Steady and Unsteady Plasma Wall Jets for Separation and Circulation Control," in *3rd AIAA Flow Control Conference, San Francisco, California*, 2006, Paper AIAA-2006-3686.

[7] T. C. Corke, C. He and M. Patel, "Plasma Flaps and Slats: An Application of Weakly-Ionized Plasma Actuators," *Journal of Aircraft*, vol. 46, no. 3, pp. 864-873, 2009.

[8] D.M. Orlov, T. Apker, C. He, H. Othman and T.C. Corke, "Modeling and Experiment of Leading-Edge Separation Control Using SDBD Plasma Actuators," in *45th AIAA Aerospace Sciences Meeting and Exhibit, Reno, Nevada*, 2007, Paper AIAA-2007-0877.

[9] M.P. Patel, Z.H. Sowle, T.C. Corke and C. He, "Autonomous Sensing and Control of Wing Stall Using a Smart Plasma Slat," *Journal of Aircraft*, vol. 44, no. 2, pp. 516-527, 2007.

[10] M.L. Post, "Plasma Actuators for Separation Control on Stationary and Oscillating Airfoils," Doctoral thesis, University of Notre Dame, Notre Dame, Indiana, 2004.

[11] L.S. Hultgren and D.E. Ashpis, "Demonstration of Separation Delay with Glow-Discharge Plasma Actuators," in *41st AIAA Aerospace Sciences Meeting and Exhibit, Reno, Nevada*, 2003, Paper AIAA-2003-1025.

[12] S.P. Wilkinson, "Investigation of an Oscillating Surface Plasma for Turbulent Drag Reduction," in *41st AIAA Aerospace Sciences Meeting and Exhibit, Reno, Nevada*, 2003, Paper AIAA-2003-1023.

[13] F. Thomas, A. Kozlov, T. Corke, "Plasma Actuators for Cylinder Flow Control and Noise Reduction," *AIAA Journal*, vol. 46, no. 8, pp. 1921-1931, 2008.

[14] Y. Li, X. Zhang and X. Huang, "The Use of Plasma Actuators for Bluff Body Broadband Noise Control," *Experiments in Fluids*, vol. 49, no. 2, pp. 367-377, 2010.

[15] S. Lemire and H.D. Vo, "Reduction of Fan and Compressor Wake Defect using Plasma Actuation for Tonal Noise Reduction," in *ASME Turbo Expo: Power for Land, Sea and Air (GT 2008), Berlin, Germany*, ASME Paper GT 2008-50821.

[16] N. Benard, J. Jolibois, M. Forte, G. Touchard and E. Moreau, "Control of an Axisymmetric Subsonic Air Jet by Plasma Actuator," *Experiments in Fluids*, vol. 43, no. 4, pp. 603-616, 2007.

[17] J. Huang, T.C. Corke and F. Thomas, "Plasma Actuators for Separation Control of Low Pressure Turbine Blades," in *41st AIAA Aerospace Sciences Meeting and Exhibit, Reno, Nevada*, 2003, Paper AIAA-2003-1027.

[18] J. List, A.R. Byerley, T.E. McLaughlin and R.D. Van Dyken, "Using a Plasma Actuator to Control Laminar Separation on a Linear Cascade Turbine Blade," in *41st Aerospace Sciences Meeting and Exhibit, Reno, Nevada*, 2003, Paper AIAA-2003-1026.

[19] S. Lemire, H.D. Vo and M.W. Benner, "Performance Improvement of Axial Compressors and Fans with Plasma Actuation," *International Journal of Rotating Machinery*, vol. 2009, Article ID 247613, 2009, 13 pages.

[20] S. Grundmann, E.L. Sayles and J.K. Eaton, "Sensitivity of an Asymmetric 3D Diffuser to Plasma-Actuator Induced Inlet Condition Perturbations," *Experiments in Fluids*, vol. 50, no. 1, pp. 217-231, 2010.

[21] S. Morris, T. Corke, D. VanNess, D., J. Stephens and T. Douville, 2005, "Tip Clearance Control Using Plasma Actuator," in *44th AIAA Aerospace Sciences Meeting and Exhibit, Reno, Nevada*, 2006, Paper AIAA-2005-782.

[22] D. K. Van Ness, T.C. Corke and S.C. Morris, "Turbine Tip Clearance Flow Control using Plasma Actuators," in *44th AIAA Aerospace Sciences Meeting and Exhibit, Reno, Nevada*, 2006, Paper AIAA-2006-0021.

[23] H.D. Vo, "Suppression of Short Length-scale Rotating Stall Inception with Glow Discharge," in *ASME Turbo Expo: Power for Land, Sea and Air (GT 2007), Montréal*, ASME Paper GT2007-27673.

[24] G. Li, Y. Xu, B. Lin, J. Zhu, C. Nie, H. Ma and Z. Wang, "Control of Endwall Secondary Flow in a Compressor Cascade with Dielectric Barrier Discharge Plasma Actuation," *Science in China Series E: Technological Sciences*, vol. 52, no. 12, pp. 3715-3721, 2009.

[25] E. Moreau, "Airflow Control by Non-Thermal Plasma Actuators," *Journal of Physics D: Applied Physics*, vol. 40, no. 3, pp. 605-636, 2007.

[26] P. Versailles, S. Ghosh, H.D. Vo and C. Masson, "Preliminary Assessment of Wind Turbine Blade Lift Control via Plasma Actuation", *Wind Engineering*, vol. 35, no. 3, pp. 339-356, 2011.

[27] M. Gad-el-Hak, "Control of Low-Speed Airfoil Aerodynamics," *AIAA Journal*, vol. 28, no. 9, pp. 1537-1552, 1990.

[28] R.P.J.O.M. Van Roojj and W.A. Timmer, "Roughness Sensitivity Considerations for Thick Rotor Blade Airfoils," in *41st AIAA Aerospace Sciences Meeting and Exhibit, Reno, Nevada*, 2003, Paper AIAA-2003-350.

[29] G.P. Corten, "Flow Separation on Wind Turbine Blades," Doctoral thesis, Utrecht University, Utrecht, Holland, 2001.

[30] Z. Du and M.S. Selig, "The Effect of Rotation on the Boundary Layer of a Wind Turbine Blade," *Renewable Energy*, vol. 20, no. 2, pp.167-181, 2000.

[31] S. Schreck and M. Robinson, "Rotational Augmentation of Horizontal Axis Wind Turbine Blade Aerodynamic Response," *Wind Energy*, vol. 5, no. 2-3, pp. 133-150, 2002.

[32] GE Wind Energy, LLC, "Advanced Wind Turbine Program Next Generation Turbine Development Project," Subcontract Report NREL/SR-5000-38752, May 2006.

[33] A.T. Lee and R.G.J. Flay, "Compliant Blades for Wind Turbines," *Transactions of the Institution of Professional Engineers New Zealand*, vol. 26, no. 1, pp.7-12, 1999.

[34] R.I. Lewis, I. Potts and A.A. Arain, "Aerodynamic Properties of NASA LS (1)-0417 MOD with Leading Edge Microspoilers for Lift/Drag Control," *Wind Engineering*, vol. 15, no. 1, pp.40-67, 1991.

[35] S.J. Johnson, C.P. Van Dam and D.E. Berg, "Active Load Control Techniques for Wind Turbines," SANDIA Report SAND2008-4809, 2008.

[36] I. Chopra, "Review of State of Art of Smart Structures and Integrated Systems," *AIAA Journal*, vol. 40, no. 11, pp. 2145-2187, 2002.

[37] T. Burton, D. Sharpe, N. Jenkins and E. Bossanyi, "The Controller," in *Wind Energy Handbook*, Chichester, England: John Wiley & Sons, pp. 471-509, 2001.

[38] "Power Control of Wind Turbines," Online: http://guidedtour.windpower.org/en/tour/wtrb/powerreg.htm [Accessed: December 8, 2010]

[39] D.R. Miller and R.L. Puthoff, "Aileron Controls for Wind Turbine Applications," work performed for U.S. Department of Energy, Conservation and Renewable Energy, Wind Energy Technology Division; prepared for *Intersociety Energy Conversion Engineering Conference, San Francisco, California*, 1984.

[40] M.A. Lackner and G.A.M. van Kuik, "A Comparison of Smart Rotor Control Approaches Using Trailing Edge Flaps and Individual Pitch Control," *Wind Energy*, vol. 13, no. 2-3, pp.117-134, 2010.

[41] T. Buhl, C. Bak, M. Gaunaa and P.B. Andersen, "Load alleviation through adaptive trailing edge control surfaces: ADAPWING overview," in *European Wind Energy Conference and Exhibition, Milan, Italy,* 2007, pp. 20-23.

[42] T.K. Barlas and G.A.M. van Kuik, "Review of State of the Art in Smart Rotor Control Research for Wind Turbines," *Progress in Aerospace Sciences*, vol. 46, no. 1, pp.1-27, 2010.

[43] L.A. Krakers, "Ductile Piezo-Electric Actuator Materials," Technical Report, Netherlands Institute for Metals Research, NIMR P06.1, 2006.

[44] D.T. Yen, C.P. van Dam, R.L. Smith and S.D. Collins, "Active Load Control for Wind Turbine Blades Using MEM Translational Tabs," in *39th AIAA Aerospace Sciences Meeting and Exhibit, Reno, Nevada*, 2001, Paper AIAA-2001-0031.

[45] R. Chow and C.P. van Dam, "Computational Investigations of Deploying Load Control Microtabs on a Wind Turbine Airfoil," in *45th AIAA Aerospace Sciences Meeting and Exhibit, Reno, Nevada*, 2007, Paper AIAA-2007-1018.

[46] K.J. Standish and C.P. van Dam, "Computational Analysis of a Microtab-Based Aerodynamic Load Control System for Rotor Blades," *Journal of the American Helicopter Society*, vol. 50, no. 3, pp. 249-258, 2005.

[47] G. Pechlivanoglou, C.N. Nayeri and C.O. Paschereit, "Performance Optimization of Wind Turbine Rotors with Active Flow Control," in *ASME Turbo Expo 2011 (GT 2011), Vancouver, B.C.*, ASME Paper GT2011-45493.

[48] F.K. Straub, "A Feasibility Study of Using Smart Materials for Rotor Control," *Smart Materials and Structures*, vol. 5, pp. 1–10, 1996.

[49] R. Barrett and S. Farokhi, "Subsonic Aerodynamics and Performance of a Smart Vortex Generator System," *Journal of Aircraft*, vol. 33, no. 2, pp. 393-398, 1996.

[50] G.V. Selby, J.C. Lin, and F.G. Howard, "Control of Low-Speed Turbulent Separated Flow Using Vortex Generator Jets," *Experiments in Fluids*, vol. 12, no. 6, pp. 394-400, 1992.

[51] J.C. Lin, "Control of Turbulent Boundary-Layer Separation using Micro-Vortex Generators," in *30th AIAA Fluid Dynamics Conference*, *Norfolk, Virginia*, 1999, Paper AIAA-1999-3404.

[52] B.L. Smith and A. Glezer, "The Formation and Evolution of Synthetic Jets," *Physics of Fluids*, vol. 10, no. 9, pp. 2281-2297, 1998.

[53] J. Tensi, S. Bourgois, J.P. Bonnet, J.M. Breux and W.L. Siauw, "Airfoil Performance Enhancement Using Fluidic Actuators," *Laboratoire d'Études Aérodynamiques UMR 6609*, 2007.

[54] U. Kogelschatz, "Dielectric-barrier Discharges: Their History, Discharge Physics, and Industrial Applications," *Plasma Chemistry and Plasma Processing*, vol. 23, no. 1, pp. 1-46, 2003.

[55] J.W. Gregory, C.L. Enloe, G.I. Font and T.E. McLaughlin, "Force Production Mechanisms of a Dielectric-Barrier Discharge Plasma Actuator," in *45th AIAA Aerospace Sciences Meeting and Exhibit, Reno, Nevada*, 2007, Paper AIAA-2007-185.

[56] N. Balcon, N. Benard, Y. Lagmich, J.-P. Boeuf, G. Touchard and E. Moreau, "Positive and Negative Sawtooth Signals Applied to a DBD Plasma Actuator - Influence on the Electric Wind," *Journal of Electrostatics*, vol. 67, no. 2-3, pp. 140-145, 2009.

[57] M. Forte, J. Jolibois, J. Pons, E. Moreau, G. Touchard and M. Cazalens, "Optimization of a Dielectric Barrier Discharge Actuator by Stationary and Non-Stationary Measurements of the Induced Flow Velocity: Application to Airflow Control," *Experiments in Fluids,* vol. 43, no. 6, pp. 917-928, 2007.

[58] T.C. Corke, M.L. Post and D.M. Orlov, "Single Dielectric Barrier Discharge Plasma Enhanced Aerodynamics: Physics, Modeling and Applications," *Experiments in Fluids,* vol. 46, no. 1, pp. 1-26, 2008.

[59] F.O. Thomas, T.C. Corke, M. Iqbal, A. Kozlov and D. Schatzman, "Optimization of Dielectric Barrier Discharge Plasma Actuators for Active Aerodynamic Flow Control," *AIAA Journal*, vol. 47, no. 9, pp. 2169-2178, 2009.

[60] M.R. Visbal, D.V. Gaitonde and S. Roy, "Control of Transitional and Turbulent Flows Using Plasma-Based Actuators," in *36th AIAA Fluid Dynamics Conference and Exhibit*, *San Francisco, California*, 2006, Paper AIAA-2006-3230.

[61] C.A. Williamson, "Compressor Blade Flow Control in an Axial Compressor with Plasma Actuators," Master's thesis, Oklahoma State University, Stillwater, Oklahoma, 2008.

[62] N. Benard, N. Balcon and E. Moreau, "Jet Flow Control by Dielectric Barrier Discharge - Excitation by Axisymmetric and Flapping Modes," in *47th AIAA Aerospace Sciences Meeting Including the New Horizons Forum and Aerospace Exposition, Orlando, Florida*, 2009, Paper AIAA-2009-776.

[63] F. Massines, A. Rabehi, P. Decomps, R. Ben Gadri, P. Segur and C. Mayoux, "Experimental and Theoretical Study of a Glow Discharge at Atmospheric Pressure Controlled by Dielectric Barrier," *Journal of Applied Physics*, vol. 83, no. 6, pp. 2950-2957, 1998.

[64] M. Paulus, L. Stals, U. Rude and B. Rauschenbach, "Two-Dimensional Simulation of Plasma-Based Ion Implantation," *Journal of Applied Physics*, vol. 85, no. 2, pp. 761-766, 1999.

[65] K.D. Hall, "Potential Flow Model for Plasma Actuation as a Lift Enhancement Device," Master's thesis, University of Notre Dame, Notre Dame, Indiana, 2004.

[66] W. Shyy, B. Jayaraman and A. Andersson, "Modeling of Glow Discharge-Induced Fluid dynamics," *Journal of Applied Physics*, vol. 92, no. 11, pp. 6434-6446, 2002.

[67] Y. Suzen and P. Huang, "Simulation of Flow Separation Control using Plasma Actuators," in *44th AIAA Aerospace Sciences Meeting and Exhibit, Reno, Nevada*, 2007, Paper AIAA-2006-877.

[68] Y. Suzen, P. Huang, J. Jacob and D. Ashpis, "Numerical Simulations of Plasma Based Flow Control Applications," in *35th Fluid Dynamics Conference and Exhibit*, *Toronto, Ontario*, 2005, Paper AIAA-2005-4633.

[69] D.M. Orlov, "Modelling and Simulation of Single Dielectric Barrier Discharge Plasma Actuators," Ph.D. Thesis, University of Notre Dame, Notre Dame, Indiana, 2006.

[70] G. Font, "Boundary Layer Control with Atmospheric Plasma Discharges," *AIAA Journal*, vol. 44, no. 7, pp. 1572-1578, 2004, AIAA Paper 2004-3574.

[71] G. Font and W.L. Morgan, "Plasma Discharges in Atmospheric Pressure Oxygen for Boundary Layer Separation Control," in *35th Fluid Dynamics Conference and Exhibit*, *Toronto, Ontario*, 2005, AIAA Paper 2005-4632, 2005.

[72] A. Likhanskii, M. Shneider, S. Macheret and R. Miles, "Modeling of Interaction between Weakly Ionized Near-Surface Plasmas and Gas Flow," in *44th AIAA Aerospace Sciences Meeting and Exhibit, Reno, Nevada*, 2006, Paper AIAA-2006-1204.

[73] D.V. Gaitonde, M.R. Visbal and S. Roy, "A Coupled Approach for Plasma-Based Flow Control Simulations of Wing Sections," in *44th AIAA Aerospace Sciences Meeting and Exhibit, Reno, Nevada*, 2006, Paper AIAA-2006-1205.

[74] W.A. Timmer and R.P.J.O.M. van Rooij, "Summary of the Delft University Wind Turbine Dedicated Airfoils," *Journal of Solar Energy Engineering*, vol. 125, no. 4, 2003.

[75] I.B. Celik, U. Ghia, P.J. Roache, C.J. Freitas, H. Coleman and P.E. Raad, "Procedure for Estimation and reporting of Uncertainty due to Discretization in CFD Applications," *Journal of Fluids Engineering*, vol. 130, no. 7, 2008.

[76] P. Versailles, V. Gingras-Gosselin and H.D. Vo, "Importance of Pressure and Temperature on the Performance of Plasma Actuators," *AIAA Journal*, vol. 48, no. 4, 2010, pp. 859-863.

[77] D. J. Laino and A.C. Hansen, "Current Efforts Toward Improved Aerodynamic Modeling Using the Aerodyn Subroutines," in *A Collection of the 2004 ASME Wind Energy Symposium Papers*, *Reno, Nevada*, pp. 329–338.

[78] X. Xu, 2011, private communication.

Appendix A

Prediction of Wind Turbine Performance Based on Blade Element Momentum Theory

The following program calculates the power and power coefficient of a wind turbine with the turbine blade design data as the input.

```
rho = 1.225;  % Air density
D = 70; R = D/2;    % Diameter (=2*R, R=35)
Area =(pi/4)*D^2;

% Turbine end-of-blade data%
a_ini = [0 0 0 0 0 0 0 0 0 0 0 0 0 0 0 0 0 0 0 0 0 0 0];
a_pr_ini = [0 0 0 0 0 0 0 0 0 0 0 0 0 0 0 0 0 0 0 0 0 0 0];

% Turbine data%
V0 = 3:25;
lambda = 6;   % Design tip speed ratio
B = 3;    % No. of blades
c  =  35*[0.02747  0.03066  0.03385  0.03704  0.04024  0.04360  0.04707
0.05062  0.05415  0.05771  0.06126  0.06479  0.06832  0.07188  0.07543
0.07782 0.07452 0.06826 0.06140]; % Spanwise chord variation
r = 35*[0.975 0.925 0.875 0.825 0.775 0.725 0.675 0.625 0.575 0.525
0.475 0.425 0.375 0.325 0.275 0.225 0.175 0.125 0.075];    % Radial
positions of elements
dr = (R/20)*ones(1,19);
alpha  =  [.............................];     % List  of  angles  of
attack
%  Cl  &  Cd  data  for  the  3  airfoils  are  listed  in  the  next  6  lines  for
   the angles of attack listed above
cl16 = [.....................................................];
cd16 = [.....................................................];
cl21 = [.....................................................];
cd21 = [.....................................................];
cl27 = [.....................................................];
cd27 = [.....................................................];

% Note: omega constant till V0 = 11.5 m/s and constant beyond.
Omega = [(lambda/R)*(1:11) (lambda*11.5/R)*ones(1,14)];
ThetaP0 = 0*ones(1,23);
ThetaT = [0.061 0.174 0.286 0.399 0.511 0.793 1.186 1.660 2.140 2.614
3.405 4.583 6.098 7.619 9.141 10.496 11.014 11.100 11.100]; % Blade
twist distribution
a = 1; b = 1; d = 1; k = 0.12;   % Constants for the stall delay model
of Laino and Hansen.

for i = 1:23
    A = a_ini(i); A_pr = a_pr_ini(i);
    for j = 1:19 % 19 elements along the radius.
        ThetaP = (ThetaP0(i)+ThetaT(j))*pi/180;
        sigma_pr = B*c(j)/(2*pi*r(j));
        A_old = A-1; A_pr_old = A_pr-1;     % Note:  Chosen  to  satisfy
        the condition of the while loop for the first time.
```

```
    % Iterating (Convergence limit: For a = 0.001, For a_pr =
    0.00001)
    while(abs(A-A_old)>0.001 || abs(A_pr-A_pr_old)>0.00001)
        phi = atan((1-A)*V0(i)/((1+A_pr)*omega(i+2)*r(j)));
        f = B*(R-r(j))/(2*r(j)*sin(phi));
        F = (2/pi)*acos(exp(-f));
        F_til = F*max(1,(1-0.25*A*(5-3*A))/(1-A));
        Alph = phi-ThetaP;
        alph_deg = alph*180/pi;
        % Interpolating to find Cl and Cd from tables.
        if (j>=1 && j<=3)
            cl2d = interp1(alpha,cl16,alph_deg);
            cd2d = interp1(alpha,cd16,alph_deg);
            alpha0 = interp1(cl16(15:38),alpha(15:38),0);
        end
        if (j>=4 && j<=11)
            cl2d = interp1(alpha,cl21,alph_deg);
            cd2d = interp1(alpha,cd21,alph_deg);
            alpha0 = interp1(cl21(15:38),alpha(15:38),0);
        end
        if (j>=12 && j<=19)
            cl2d = interp1(alpha,cl27,alph_deg);
            cd2d = interp1(alpha,cd27,alph_deg);
            alpha0 = interp1(cl27(15:38),alpha(15:38),0);
        end
        % Stall delay model of Laino and Hansen.
        f_alpha = max(min(1,(50-alph_deg)/20),0);
        clp = 2*pi*(alph-alpha0*pi/180);
        L = omega(i+2)*R/(V0(i)^2+(omega(i+2)*R)^2)^0.5;
        fl=(0.5/pi)*((1.6*(c(j)/r(j))/0.1267)*(a-
        c(j)/r(j))^(d*R/(L*r(j))))/(b+(c(j)/r(j))^(d*R/(L*r(j))))-
        1);
        dcl = fl*(clp-cl2d);
        dcd=((sin(alph)-k*cos(alph))/(k*sin(alph)+cos(alph)))*dcl;
        cl3d = cl2d+f_alpha*dcl;
        cd3d = cd2d+f_alpha*dcd;
        cn = cl3d*cos(phi)+cd3d*sin(phi);
        ct = cl3d*sin(phi)-cd3d*cos(phi);
        A_old = A;
        A_pr_old = A_pr;
        A = 0.8/(4*F_til*(sin(phi))^2/(sigma_pr*cn)+1)+0.2*A;
        A_pr=0.8/(4*F*sin(phi)*cos(phi)/(sigma_pr*ct)-1)+0.2*A_pr;
    end
    Urel_sq = (V0(i)*(1-A))^2+(omega(i+2)*r(j)*(1+A_pr))^2;
    dL = 0.5*rho*Urel_sq*cl3d*c(j)*dr(j);
    dD = 0.5*rho*Urel_sq*cd3d*c(j)*dr(j);
    dFn = dL*cos(phi)+dD*sin(phi);
    dFt = dL*sin(phi)-dD*cos(phi);
    dQ(j) = dFt*r(j);
end
Q = sum(dQ);
P(i) = Q*omega(i+2);
```

```
    Cp(i) = P(i)/(0.5*rho*area*V0(i)^3);
end
V0 = [[1 2] V0];
P = 3*[[0 0] P];
Cp = 3*[[0 0] Cp]; % Multiplying by no. of blades to get total power
figure(1)
plot(V0,P/1000);
title(sprintf('P vs V0'));
xlabel('V0'), ylabel('P');
print -dpng PvsVo(DesignedBlade)
figure(2)
plot(V0,Cp);
title(sprintf('Cp vs V0'));
xlabel('V0'), ylabel('Cp');
print -dpng CpvsV0(DesignedBlade)
lambda=(omega*D./(2*V0));
figure(3)
plot(lambda,Cp);
title(sprintf('Cp vs lambda'));
xlabel('lambda'), ylabel('Cp');
print -dpng CpvsLambda(DesignedBlade)
```

Validation of the Matlab code with WT_Perf and the turbine power curve with the stall delay model

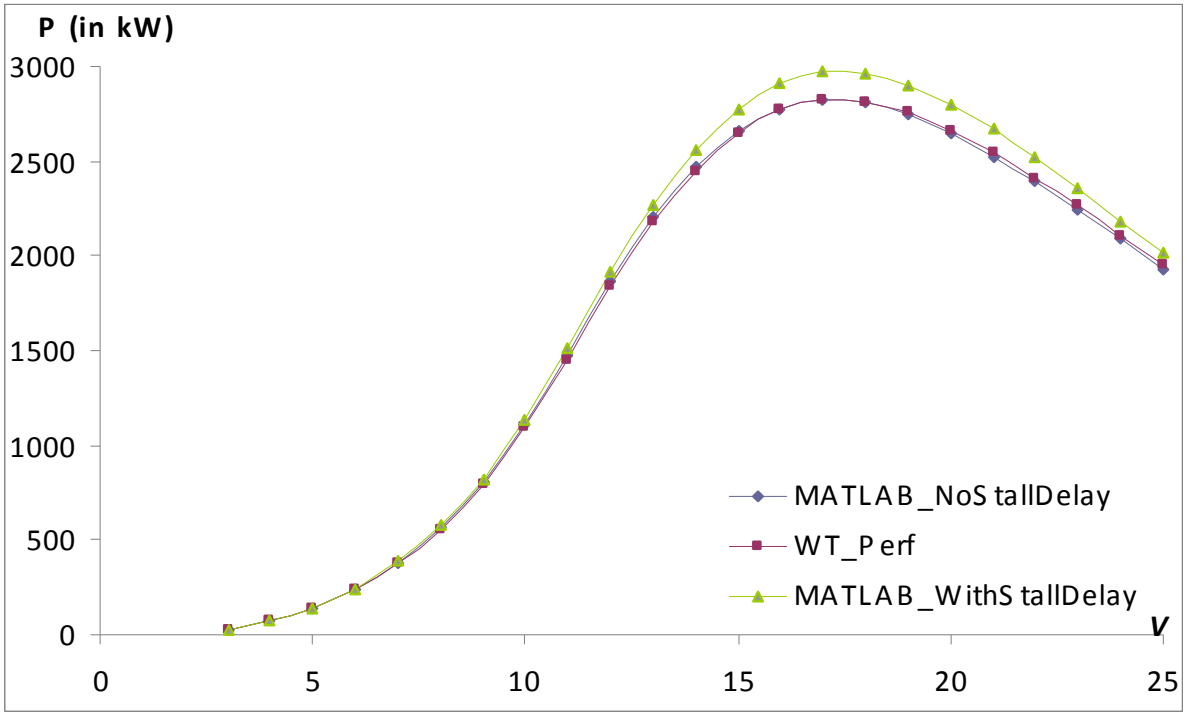

Figure A.1 Validation of the Matlab code for turbine performance with WT_Perf

Appendix B

Effect of Multiple Actuators in Series

Figure B.1 presents the impact of multiple actuators in series as opposed to a single actuator that is placed optimally on the suction side for three different angles of attack. This analysis is done for the small-scale blade profile. The presence of three plasma actuators, situated at 25%, 55% and 85% of the chord length and separated by a distance of one actuator width, is simulated and the effect on lift and drag is shown along with the effect of a single actuator. The actuation strength is 150 mN/m and the incoming relative velocity is 30 m/s.

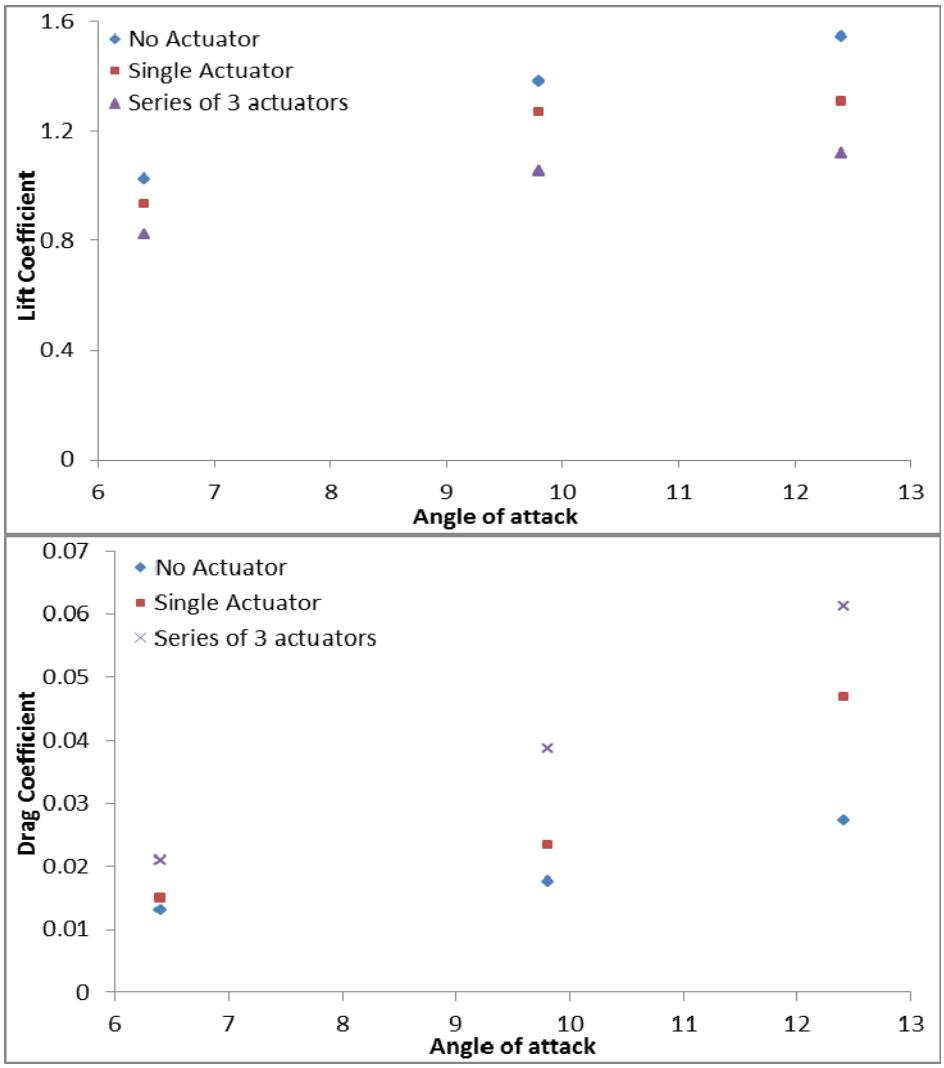

Figure B.1 Effect of multiple actuators versus single optimally positioned actuator

It is evident that the influence of three actuators in series is greater than that of a single actuator. However, it should be noted that the presence of n actuators in series does not imply that ΔC_l and ΔC_d will be amplified n times compared to a single actuator.